CONTROL OF SHOCK WAVE OSCILLATION IN TRANSONIC INTERNAL FLOW AROUND AN AIRFOIL USING CAVITY

by

Md. Abdul Hamid (0413102082)

Submitted in partial fulfillment of the requirements for the degree of Master of Science in Mechanical Engineering

Under the supervision of
Dr. A. B. M. Toufique Hasan

Associate Professor

Department of Mechanical Engineering
Bangladesh University of Engineering and Technology (BUET)

BANGLADESH UNIVERSITY OF ENGINEERING AND TECHNOLOGY,
DHAKA – 1000, BANGLADESH

Certificate of Approval

The thesis titled, **"Control of Shock Wave Oscillation in Transonic Internal Flow Around an Airfoil Using Cavity"**, submitted by **Md. Abdul Hamid**, Roll No: 0413102082, Session: April 2013, has been accepted as satisfactory in partial fulfillment of the degree of Master of Science in Mechanical Engineering on 26th January 2016.

_____

Dr. A. B. M. Toufique Hasan
Associate Professor
Department of Mechanical Engineering
BUET, Dhaka

Chairman
(Supervisor)

_____

Head
Department of Mechanical Engineering
BUET, Dhaka

Member
Ex-Offficio

_____

Dr. Md. Quamrul Islam
Professor
Department of Mechanical Engineering
BUET, Dhaka

Member
(Internal)

_____

Dr. Mohammad Ali
Professor
Department of Mechanical Engineering
BUET, Dhaka

Member
(Internal)

_____

Dr. A.K.M. Sadrul Islam
Professor
Department of Mechanical and Chemical Engineering
Islamic Institute of Technology (IUT)
Board Bazar, Gazipur

Member
(External)

Candidate’s declaration

This is hereby declared that this thesis or any part of this thesis has not been submitted elsewhere for award of any degree or diploma.

_____

Md. Abdul Hamid

Acknowledgements

First of all, I want to express my warm gratitude to the Almighty, Creator for everything I have achieved so far. I would like to pay my heartiest gratitude to my honorable thesis supervisor, Dr. A. B. M. Toufique Hasan, Associate Professor, Department of Mechanical Engineering, BUET, for his continuous support, valuable guidance and suggestion throughout this study. Without his initiative ideas, talents, guidelines and encouragements this challenging work would not have been possible to complete successfully.

I also would like to thank all others who are directly or indirectly related to this thesis by sharing their ideas, suggestions and finally supporting me.

The present work has been carried out with computational resource support from Higher Education Quality Enhancement Project (HEQEP), AIF (2nd Round)-Sub- Project CP 3111, UGC, MoE, Government of Bangladesh (Contract no. 34/2014).

Abstract

Self sustained shock wave oscillation on airfoils at transonic flow conditions are associated with the phenomenon of buffeting, high speed impulsive noise, non synchronous vibration, high cycle fatigue failure and so on. Though experiments demonstrate the presence of periodic shock oscillation in flow over airfoil in some transonic speeds, the physical mechanism of periodic shock motion is not fully understood yet. The present numerical study investigates the intricate flow phenomenon associated with self sustained shock oscillation and the passive control of shock oscillation using cavity over a symmetrical circular arc airfoil at zero incidence. The effect of incorporating both open and perforated cavity on the airfoil surfaces are demonstrated systematically considering pressure rise across the shock as an indicator of shock strength. Three different cases of open cavity control and nine different cases of perforated cavity control is studied along with the clean (base airfoil) airfoil. Results for base airfoil and airfoil with cavities (open and perforated) are compared to understand the effects of cavity installation. Shock strength, total pressure loss and surface pressure fluctuation are investigated by interpreting various shock characteristics like shock location, shock Mach number, boundary layer thickness and shock boundary layer interaction zone for all the cases. Results show that both open and perforated cavity can reduce the shock strength, surface pressure fluctuation near the airfoil and total pressure loss. The change in both flow characteristics and shock wave characteristics is studied and their dependency on the configuration of cavity and percentage of perforation are observed and proper suggestions are made.

The results suggest that open cavity can be a better choice to control shock oscillation for external high speed flow over a single airfoil or internal flows through a series of airfoils separated by sufficient distance. But open cavities have a major difficulty for internal high speed flow application through a series of airfoils placed close to one another. On the other hand perforated cavities can also reduce surface pressure fluctuation for both internal and external high speed flows though their performance is not as good as open cavities. A comparative assessment is performed to ensure the economic feasibility of both open and perforated cavity control by calculating the integrated total pressure loss (*ITPL*).

List of symbols

c	chord length of the airfoil (unit: mm)
$\boldsymbol{E}$	inviscid flux vector in x-direction
$\boldsymbol{F}$	inviscid flux vector in y-direction
H	height of the channel (unit: mm)
$\boldsymbol{H}$	turbulance source term
$ITPL$	integrated total pressure loss
M	mach number
n	no of sampling points
p	static pressure (unit: kpa)
PR	pressure ratio
q	dynamic pressure (unit: kpa)
$\boldsymbol{R}$	viscous flux vector in x-direction
RMS	root mean square
$\boldsymbol{S}$	viscous flux vector in y-direction
$\boldsymbol{U}$	conservative flux vector
T	time period (unit: s)
t	time (unit: s)
x	stream wise coordinate (unit: mm)
$[x]$	Shock boundary layer interaction zone
y	normal coordinate (unit: mm)
δ	boundary layer thickness (unit: mm)

subscripts

b	back condition
i	instantaneous state
t	total quantity
0	upstream condition
1	ahead of shock
01	total condition at inlet
s	shock wave

TABLE OF CONTENT

CHAPTER 1

INTRODUCTION

In transonic flow over an airfoil both subsonic and supersonic conditions are present in the flow field. Typically transonic flow includes flows with free stream Mach numbers from 0.6 to 1.2. When an airfoil is subjected to such a flow, shockwave could generate on the airfoil surfaces. This shockwave acts as a barrier in between the subsonic and supersonic region. The shock waves lead to a rapid rise in drag due to the emergence of wave drag and increase in viscous drag. The flow separation occurs due to the sudden pressure rise across the shockwave. This separation is known as shock induced separation which increases the thickness of the boundary layer.

1.1 FLOWFIELD DEVELOPMENT

When transonic flow occurs past an airfoil a local supersonic flow region is formed known as supersonic bubble. Often this supersonic bubble is terminated by creating a shock wave. This shock wave adds an additional drag. This additional drag which is called wave drag increases the required power input to operate fluid Machinery. At some particular conditions this shock wave starts to oscillate over the airfoil surface. While oscillating the shock absorbs energy from the flowing fluid to maintain its oscillation. So this shock oscillation introduces another additional power loss. Not only the shock oscillation increases the required input power but also it causes pressure fluctuation over the airfoil surface which is the source of noise, vibration, fatigue and so on.

For fluid Machinery where high speed internal flow over airfoil occurs (such as turbine, compressor etc) the self sustained shock oscillation limits the performance of the machinery. Thus researchers are always concerned about the control of this self sustained shock oscillation. Both "Active" and "Passive" technique has been suggested for this purpose. Active techniques require additional power to control the shock oscillation, which makes the use of active techniques questionable from economic point of view. So the alternate solution is the passive techniques which do not require any additional power source. The present study is intended to control the shock oscillation over a bi-convex circular arc airfoil by passive technique. Before going to the control of shock oscillation it is essentially mandatory to understand the mechanism of the shock oscillation.

1.2 MECHANISM OF SELF SUSTAINED SHOCK OSCILLATION

Two different mechanisms have been proposed by scientists. The first one is based on the change in effective airfoil shape and corresponding change in airfoil camber. And the second one is based on the propagation of downstream moving pressure wave and the upstream moving waves created due to the disturbances at the trailing edge (TE). The present study is carried out based on the second mechanism of shock oscillation. Tijdeman [2] introduced the concept of the disturbance wave and concluded that these waves are created to satisfy the "Kutta condition" at the trailing edge. He referred this upstream moving wave as "Kutta wave". Lately Lee [17] observed that there is a significant deviation between the time required to propagate the Kutta wave from TE to the shock and the time period of the shock oscillation. Then he concluded Tijdeman's model as incomplete and proposed a closed loop mechanism for the shock oscillation.

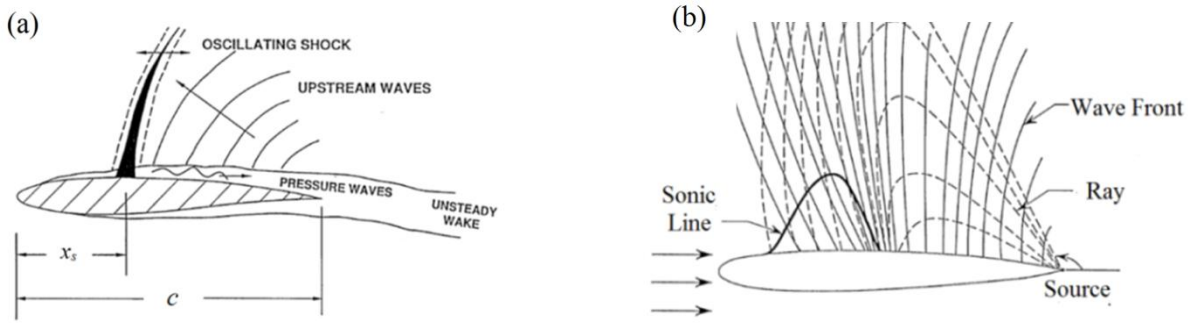

Fig.1.2.1: Close loop mechanism of self sustained shock oscillation. (a) propagation of pressure wave and upstream wave; (b) dispersion of upstream wave into the flow field. [From Ref. 17]

The shock oscillation causes the unsteady pressure fluctuation and that leads toward generation of pressure wave at the shock foot. This pressure wave moves toward the TE through the separated flow region and interact with the disturbances created at the TE as shown in figure 1.2.1 (a). This interaction creates the upstream waves which propagate through the outside of the separated region which is shown in figure 1.2.1 (b). This upstream wave carries the required energy to the shock wave to maintain its oscillation and then the loop is completed. This type of shock oscillation is called self sustained shock oscillation as the shock oscillates without any external energy input.

The Mechanism proposed by Lee is called as feedback mechanism. The mechanism assumes the flow past the airfoil is fully separated. Studies involving calculation of time period show that time required for the pressure wave and the upstream waves to complete one cycle is in good agreement with the oscillation time period.

1.3 TYPES OF SHOCK OSCILATION

There are three types of shock oscillation and they are known as Tijdeman type A, Tijdeman type B and Tijdeman type C shock oscillation.

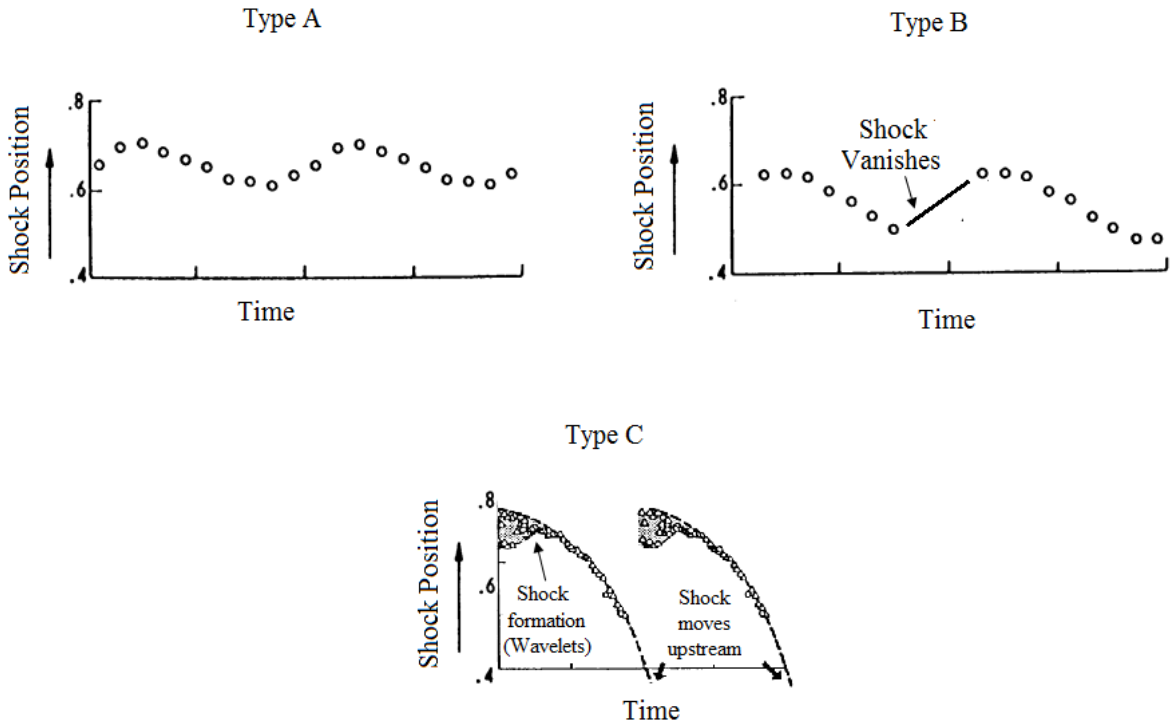

Fig. 1.3.1: Shock location with time for all three types of shock oscillation [17]

Type A oscillation is characterized as continuous oscillation of shock wave while type B and C are characterized as discontinuous. A shock movement associated with the continuous oscillation of both upper and lower surface (for symmetrical airfoil) with about 180^0 in phase is called type A shock oscillation. Meanwhile when the shock oscillate in a manner that the upper shock moves forward and eventually vanishes at about half of the total oscillation period and the lower surface shock starts to move at about half of the cycle and then vanishes at about the end of the cycle is known as type B shock oscillation. For type B shock oscillation the shock on both surfaces travel about half of its path as a shock wave and then return to its initial position as a compression wave (will be discussed in section 5.2.1 and 5.2.2). But for the type C shock oscillation, the shock moves forward as a shock wave and then turn into a compression wave and that compression wave continues to move forward. Eventually the compression wave passes the leading edge and then the cycle starts again.

1.4 CONTROL OF SELF SUSTAINED SHOCK OSCILLATION

Shock oscillation is primarily dependent on many parameters like the free stream Mach number, boundary layer separation, airfoil geometry etc. So researchers are trying to design a proper geometry by analyzing its shock control capabilities. Both active and passive techniques are been studied all over the world. Most control techniques applied are based on either of the flowing two concepts:

- **Reduction of boundary layer separation downstream of the shock**:
  In this process the propagation of pressure wave is interrupted. As a result shock strength is reduced as well as the wave drag.

- **Thickening of boundary layer upstream of the shock:**
  In this process a single strong shock is transformed into several weaker shock and the skin friction drag is reduced.

1.5 SOME PASSIVE CONTROL TECHNIQUES FOR SELF SUSTAINED SHOCK OSCILLATION

Several types of passive control techniques have been studied by researchers. Some of the passive techniques are listed and briefly discussed below:

- Buffet breather: Buffet breather is a narrow passage that connects the two downstream on upper and lower surfaces. Breather allows flow of air in both directions and is installed just after the mean shock position as shown in figure 1.5.1 (a). When the shock on the upper surface is stronger than the lower surface shock breather allows air to flow from up side to the down side of the airfoil and vice versa. As breather tries to equalize the pressure on both the surfaces it reduces the pressure fluctuation on the airfoil.
- Trailing edge thickening: Disturbances are created due to the sharpness of the airfoil at the trailing edge. Thickening of trailing edge affect the creation and interaction of the disturbances with the pressure wave.
- Inter connecting passage and cross connecting passage: These techniques work in a similar mechanism of buffet breather. The ways of different connections of narrow passages are shown in figure 1.5.1 (c) and (d). They also allow bi-directional air flow and tries to equalize the pressure difference.

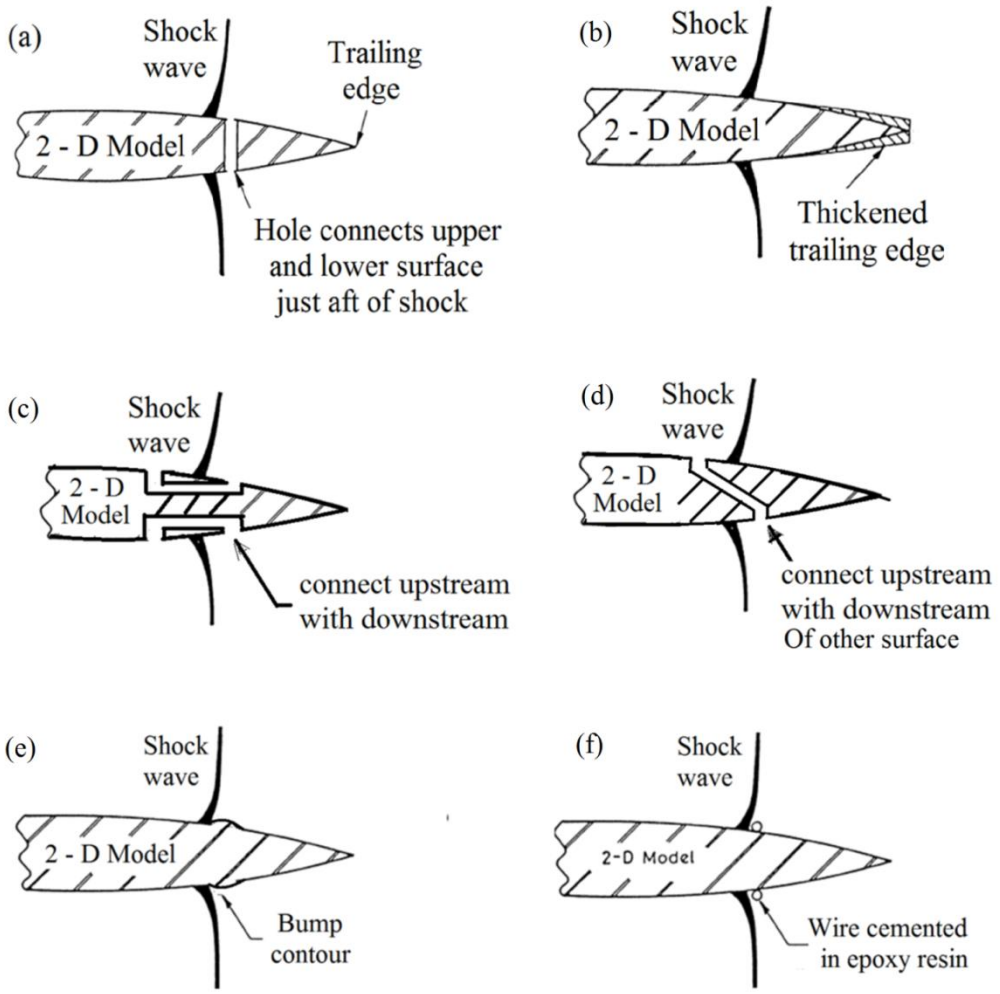

Fig. 1.5.1: Use of (a) buffet breather and (b) trailing edge thickening (c) inter connecting passage; (d) cross connecting passage; (e) bump contour and (f) wire as passive shock oscillation control technique.

- Bump contouring and wires: The idea of using a bump or wire is to change the airfoil shape to accommodate the flow separation. It also interrupts the creation of pressure wave and lowers the shock oscillation. The bump or the wire is installed at a location where the boundary layer separation occurs which is usually just downstream of the shock foot. The configuration of bump and wire installation is shown in figure 1.5.1 (e) and (f).
- Open and perforated cavity: Open cavities can create vortices that actually increase the shock foot size and thus lower the shock boundary interaction. On the other hand the porous cavity could incorporate secondary flow through cavity path. This secondary flow add a suction effect at the downstream of the shock and a blow like effect in the upstream of the shock that create several weaker shock. The present study investigates the effect of open and perforated cavity on the shock oscillation. The geometry of various configuration used is discussed in section 1.6.

1.6 AIRFOIL GEOMETRY AND DESIGNATION:

In this research, the base airfoil considered is a biconvex circular-arc airfoil with chord length (c) of 48 mm and maximum thickness of 12% of the chord length. The geometry of the base airfoil is shown in figure 1.6.1.

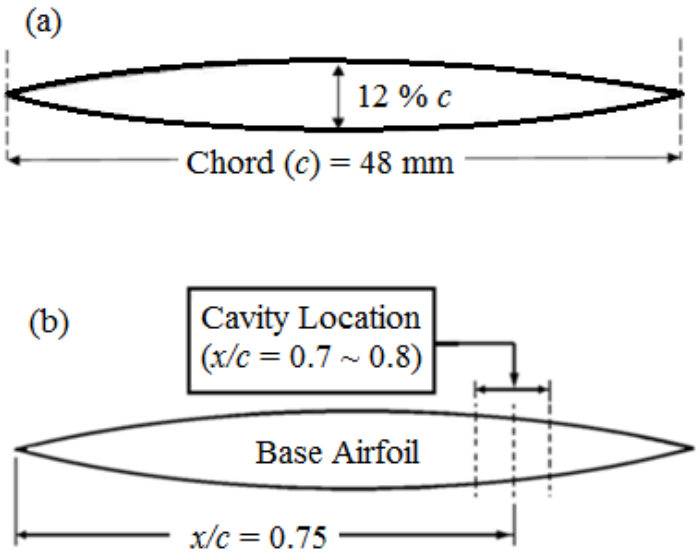

Fig. 1.6.1: (a) 12% biconvex circular arc airfoil and (b) location of cavity installation.

The base airfoil has been modified by incorporating some open and perforated cavity. The detailed geometries for all the cases are shown in figure 1.6.3 and 1.6.4. The designations of the cases are selected based on their geometric configuration.

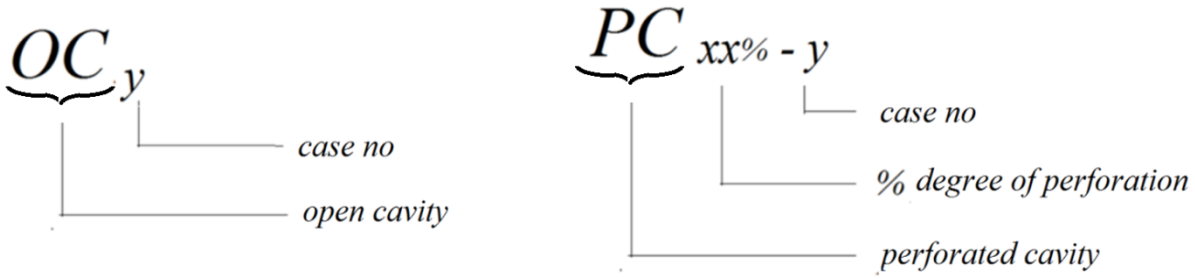

Fig. 1.6.2: Designation of control cases

The first two letters (capitalized) stand for type of cavity ('*OC*' for open cavity and '*PC*' for perforated cavity). For open cavity cases the subscript '*y*' is indication of different configurations (case number). Again for perforated cavity the subscript '*xx*' is the percentage of perforation (percentage relative to cavity length, *l*) and the subscript '*y*' is indication of different configurations (case number). The designations of different control cases are represented in figure 1.6.3 and 1.6.4.

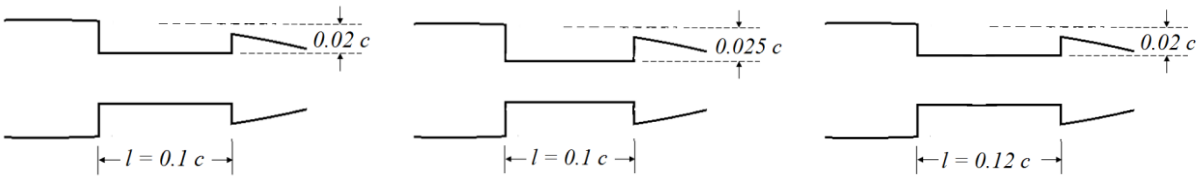

OC_1 OC_2 OC_3

Fig: 1.6.3: Configuration of open cavities

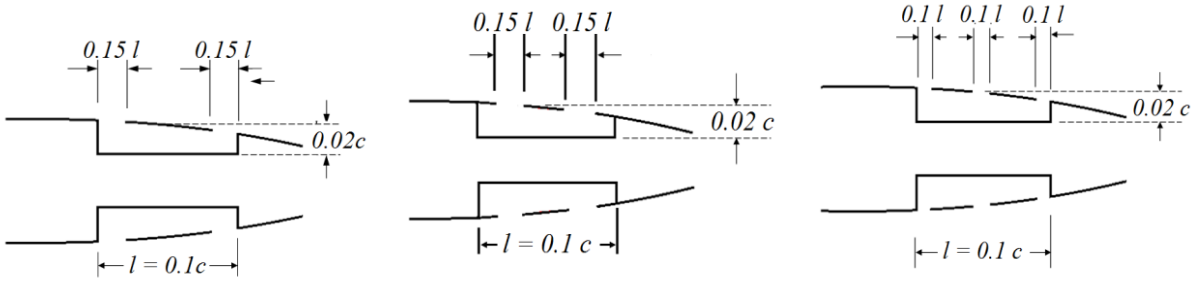

$PC_{30\%-1}$ $PC_{30\%-2}$ $PC_{30\%-3}$

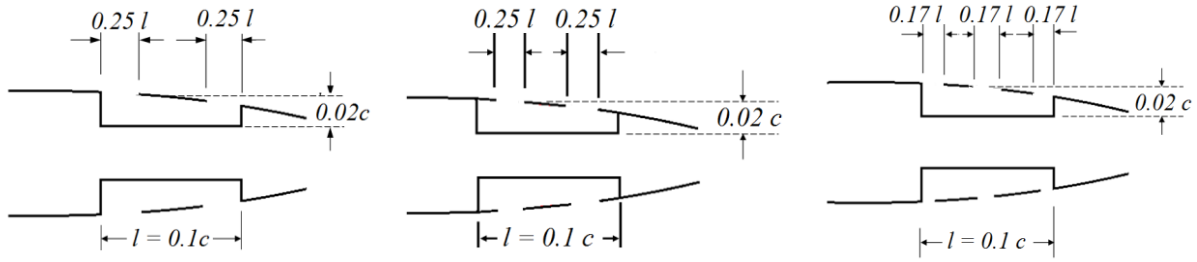

$PC_{50\%-1}$ $PC_{50\%-2}$ $PC_{50\%-3}$

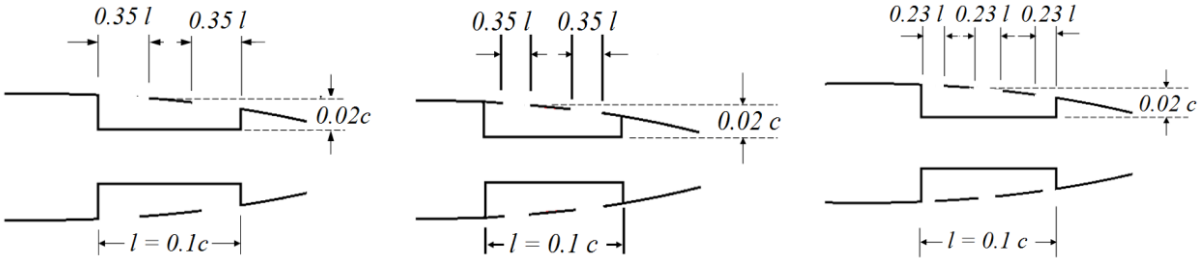

$PC_{70\%-1}$ $PC_{70\%-2}$ $PC_{70\%-3}$

Fig: 1.6.4: Configuration of perforated cavities

The cavities are installed identically on both upper and lower surface. As the fluctuation of static pressure is maximum at *x/c* = 0.75 (section 5.4) for base airfoil the cavity is installed with mean position of *x/c* = 0.75. The depth of the cavity is measured vertically at that point *x/c* = 0.75. The perforated cavities were installed in such manner that it is symmetrical about the axis passing through *x/c* = 0.75. For every perforated cavity the perforation is measured in percentage of the cavity length (*l*). All the openings of the cavity are of identical dimension and are equally spaced from the mean position of the cavity.

To avoid structural failure the entire analysis is carried out with cavities of length and the depth within 12% and 2% of the chord length of the airfoil. Three different cases for open and nine different cases for perforated cavity are studied. The enlarged views of the open and perforated cavities are shown in figure 1.6.3 and 1.6.4 along with their case designation. The perforated cavities considered are 30%, 50% and 70% perforated cavity. The percentage of perforation is calculated as follows:

$$\%\ \text{degree of Perforation} = \frac{\text{Sum of length of openings}}{Total\ length\ of\ the\ cavity} \times 100\ \%$$

Total of nine perforated cavity with 3 different configurations and each configuration with 3 different percentage of perforation has been studied in the present study

1.7 OBJECTIVES:

The objectives of this present study are:

- To develop a numerical model to capture the shock wave oscillation around an airfoil in transonic internal flow.
- To validate the transonic flow field around an airfoil with available experimental wind tunnel test data.
- To investigate the effect of incorporating open cavity (passive control) in the region of shock wave oscillation.
- To study the effects of length and depth of the cavity on shock wave oscillation.
- To investigate the effect of incorporating perforated cavity (passive control) with different percentage of porosity.
- To identify the effects of location and orientation of opening for a fixed percentage of porosity on shock wave oscillation.
- To assess the comparative benefits achieved by open cavity and perforated cavity.

CHAPTER 2

LITERATURE REVIEW

McDevitt et al [1], studied the transonic flow over an 18% thick airfoil both experimentally and numerically. The study includes investigation of parameters like surface pressures, streamline, flow separation patterns and shadowgraphs. Test results are presented for Reynolds number 1 million to 17 million, covering laminar to fully developed turbulent flows. With the variation of the airfoil peak local Mach number from about 1 to 1.4, both weak and strong shock boundary–layer interactions are observed. For a limited range of free stream Mach number, the airfoil flow fields are found to be unsteady which can be investigated by the instantaneous pressure measurements and high-speed shadowgraph movies. The study also provides comparison of experimentally determined and numerically simulated results using a new viscous-turbulent code. The comparisons show the importance of including an accurate turbulence model. When the shock-boundary-layer interaction is weak the turbulence model employed appears adequate, but when the interaction is strong, and extensive regions of separation are present, the model is inadequate and needs further development. The results suggest that the shock-boundary-layer interaction phenomena are strongly dependent on Mach number and Reynolds number.

A detailed overview of the behaviors of the transonic flow around an oscillating airfoil has been discussed by Tijdeman [2]. The study includes experimental analysis with the exploratory wind-tunnel at high-subsonic and transonic flow on a conventional airfoil with oscillating flap and a supercritical airfoil oscillating in pitch. In the analysis of the experimental results the study emphasized upon the typical aspects of transonic flow, namely the interaction between the steady and unsteady flow fields, the periodical motion of the shock waves and their contribution to the overall unsteady air-loads. Special attention is paid to the behavior of the supercritical airfoil in its "shock-free" design condition. Moreover, it is discussed to what extent linearization of the unsteady transonic flow problem is allowed if the unsteady field is considered as a small perturbation superimposed upon a given mean steady-flow field. Finally, the current status of unsteady transonic flow theory is reviewed and the present test data are used to evaluate some of the recently developed calculation methods.

Levy Jr. [3] had described an experimental and computational investigation of the steady and unsteady transonic flow fields about a thick airfoil. An operational computer code for solving the two dimensional, compressible Navier-Stokes equations for flow over airfoils was modified to include solid-wall, slip-flow boundary conditions. Steady and unsteady flow-fields about an 18% thick circular arc airfoil at Mach numbers of 0.720, 0.754 and 0.783 and a chord Reynolds number of 11×10^6 are predicted and compared with experimental results. From the comparisons it is observed

that the pressure and skin-friction distributions show improved agreement when test-section wall boundaries are included in the computations. Steady-flow results were good in quantitative agreement with experimental data for flow conditions which result in relatively small regions of separated flow. For flows with larger regions of separated flow, improvements in turbulence modeling are required. The results suggest use of computer codes with proper boundary conditions, an improved tool with proper turbulence models. It can be seen that Navier-Stokes type computer codes are capable of reproducing the time-dependent aspects of unsteady turbulent flows involving weak and strong shockwave boundary-layer interactions. These results had inspired confidence that once turbulence models are developed with which the improved computer codes can predict experimental steady-flow results, the codes can then be used to study the time-dependent aspects of unsteady flows and hence provide insight into unsteady aerodynamic phenomena such as buffeting, inlet buzz, and rotating helicopter blades.

Tijdeman and Seebass [4] had added different information to understand the transonic flow past oscillating airfoils. By that time, the recent studies have provided results essential for the design of transonic aircraft. The main limitations of these experiments were their failure, for the most part, to duplicate full scale Reynolds numbers and an inability to duplicate free flight conditions due to wind tunnel wall interference., Experimental studies, both in progress and planned for the future, would be more nearly at full-scale Reynolds number, and eventually these Reynolds numbers would be obtained with minimum wall interference in new facilities now under development.

Paralleling this progress had been a rapid development of reliable, and in the small perturbation approximation, efficient numerical algorithms for the computation of inviscid flows. Numerical results from these methods were in qualitative agreement with the experimental observations, with the main discrepancies in quantitative prediction as a consequence of the inviscid approximation. For steady flows coupled inviscid-boundary layer calculations of unseparated flows had obtained quantitative agreement with experimental measurements. He had expected this to be true for unsteady flows in the near future. The numerical simulation of unsteady separated flows was demonstrably possible, but the two orders of magnitude improvement in computer speed that was projected for a special-purpose aerodynamic computer would be essential for this simulation to have practical consequences. It was the authors' opinion that the satisfactory prediction of unsteady airloads for aeroelastic applications was within reach. This could be accomplished by "tuning" inviscid boundary conditions to model an experimentally determined steady flow and then computing its unsteady response using an inviscid small-perturbation algorithm. Thus, the time was ripe to start with the incorporation of the new methods in aero elastic practice as recently demonstrated by Ashley (1979). Of course, the use of two-dimensional methods is justified only for large aspect-ratio wings. To treat the low aspect-ratio configuration the next, and not difficult, step had to be made, namely, the development of prediction methods for three-dimensional flows.

Gronland et al.[5] discussed the accuracy one can obtain in predictions of unsteady transonic flows by a modern CFD method using a time accurate Reynolds-averaged Navier-Stokes solver. The test case used in the study is an 18% thick biconvex, two dimensional airfoil. Experiments have revealed that this geometry had showed a strong oscillatory flow in a certain regimes, often referred to as buffet. Sensitivity to numerical and physical modeling was assessed through repeated computations with various spatial and temporal discretization, numerical schemes and different types of turbulence models. The correlation between the airfoil in a free flight and in a wind tunnel environment was also investigated. It had shown that modern CFD methods can indeed predict the complex buffet phenomena with reasonable accuracy. This work highlights some of the most critical aspects of physical and numerical modeling of buffet. It was also shown that lift and drag on the airfoil differs considerably between the free flight and wind tunnel environments.

McDevitt et al [6] continued the early study and extends the original test program to include effects of angle of attack, effects of leading and trailing-edge splitter plates, additional unsteady pressure fluctuation (buffeting) measurements and flow-field shadowgraphs, and application of an oil-film technique to display separated-wake streamlines. Detailed comparisons of computed and measured pressure distribution for steady and unsteady flows, using a recent computer code representative of current methodology, are included. It was found that the numerical solutions are often fundamentally incorrect in that only "strong" (Shock-polar terminology) shocks are captured, whereas experimentally, both strong and weak shock waves appear.

Li et al. [7], experimentally investigated the effects of divergent trailing edges and Gurney flaps on a supercritical airfoil at a Mach number M = 0.7 and a Reynolds number Re= 3.15×10^5 based on the airfoil chord length. The effects of Gurney flaps with height h = 0.5%, 1.0%, and 2.0% chord length, respectively. The results revealed that, in comparison with the divergent trailing edge, the gurney flaps had significant effects on improving the aerodynamics characteristics of the tested supercritical airfoil, and even on the airfoil with divergent trailing edge. When the Gurney flaps were utilized, the lift coefficient, maximum lift coefficient and the maximum lift-to-drag ratio of both supercritical and divergent trailing edge airfoils were greatly increased. The lift-enhancing effects on Gurney flaps under high-speed circumstances mainly came from its ability of shifting backward the shock on the upper surface. Moreover, the installation of Gurney flaps will increase wave drag and base-pressure drag, but at the same time, the pressure on the lower surface of the airfoils was increased which lead to an increased rear-body loading, and the position of the shock of pressure on the upper surface was greatly shifted backward, the supersonic region is thus enlarged, which led to an increased suction. Both the increments of pressure on the lower surface and suction on the upper surface resulted in a total lift increase. As the lift did not increase with the drag linearity, the lift-to-drag ratio increase and aerodynamics characteristics improvement were obtained under some circumstances.

Alfano et al [8] had worked with external or internal transonic flows using a standard k-ε turbulence model relying on the Boussinesq assumption. The study states a linear dependence of the turbulent stresses on the mean shear stress, does not allow the successful prediction of unsteady flow phenomena such as self-sustained shock oscillations, because of an excessive production of turbulent kinetic energy. A weak non-linear correction that makes the eddy viscosity coefficient dynamical and a so-called PANS approach that modifies the dissipation rate equation allow to improve the standard model so as to predict the appearance of self -sustained shock oscillations over an airfoil and in a diffuser. The computed cases and the results obtained regarding both external and internal aerodynamics, highlight the need for a true research effort for the efficient and adapted simulation of low-frequency self-induced transonic flow oscillations. A clear limitation of this work is the assessment of the PANS approach on bi-dimensional grids only. Hybrid turbulence modeling may strongly depend on the chosen turbulence model. Clearly the evolutions of the work will be strongly dependent of the currently intense research effort in hybrid turbulence modeling. Due to the low main frequencies and high Reynolds numbers involved, which prohibit any affordable Large Eddy Simulations attempts, hybrid turbulence modeling however appears as a real future need for the transonic flows.

Raghunathan et al [9] had reviewed the understanding of periodic transonic flow briefly. The effects of boundary-layer transition, non-adiabatic wall conditions and modifications to the airfoils surface geometry at the shock interactions on periodic transonic flow are discussed. Through the methods presented, it is proposed that the frequency of the periodic motion can be predicted with reasonable accuracy, but there are limitations on the prediction of the buffet boundaries associated with periodic transonic flows. Several methods have been proposed by which the periodic motion may be virtually eliminated, most relevantly by altering the position of transition fix, contouring the airfoils surface or adding a perforated surface and a cavity in the region of shock interaction. In addition, it has been shown that heat transfer can have a significant effect on buffet. The paper has reviewed the current understanding of periodic transonic flow over circular, NACA0012 and supercritical airfoils and the use of devices to control the periodic motion.

In the numerical investigation of Chen et al [10] various fundamental mechanisms dictating the intricate flow phenomena, including moving shock wave behaviors, turbulent boundary layer characteristics, kinematics of coherent structures and dynamical processes in flow evolution, have been studied systematically. A feedback model is developed to predict the self-sustained shock wave motions repeated alternately along the upper and lower surfaces of the airfoil, which is a key issue, associated with the complex flow phenomena. Based on the moving shock wave characteristics, three typical flow regimes are classified as attached boundary layer, moving shock wave/turbulent boundary layer interaction and intermittent boundary layer separation. The turbulent statistical quantities have been analyzed in detail, and different behaviors are found in the three flow regimes.

Some quantities e.g. pressure-dilatation correlation and dilatational dissipation, have exhibited that the compressibility effect is enhanced because of the shock wave /boundary layer interaction. Further, the kinematics of coherent vertical structures and the dynamical processes in flow evolution are analyzed. The speed of downstream-propagating pressure waves in the separated boundary layer is consistent with the convection speed of the coherent vertical structures. The multi-layer structures of the separated shear layer and the moving shock wave are reasonably captured using instantaneous Lamb vector divergence and curl, and the underlying dynamical processes are clarified. In addition, the proper orthogonal decomposition analysis of the fluctuating pressure and the separated shear layers in the trailing-edge region. The results obtained in this study provide physical insight into the understanding of the mechanisms relevant to this complex flow.

Catalano and Tognaccini [11] analyzed the incompressible flow at Reynolds number 6.0×10^4 around the Selig –Donovan 7003 airfoil. The airfoil performances have been computed by the Reynolds averaged Navier-Stokes equations and large eddy simulations. The airfoil stall and preliminary post-stall have been obtained by the both methods. Some limitations of RANS turbulence models for low-Reynolds number flows have been overcome by the k-ω SST-LR model, a recent modification of the well-known SST model. Large-eddy simulations have also been performed for a more detail analysis of the results. The relevance in the stall mechanism of the laminar separation bubble arising on the airfoil is highlighted. The stall occurs when the laminar bubble present in the leading edge zone and a separated region forming on the central part of the airfoil join together. The k- ω SST-LR model returns the same stall mechanism as the large eddy simulation. Flows at low-Reynolds numbers can be simulated by the RANS methods, but the choice of the turbulence model is crucial. The k- ω SST-LR model has provided results in good agreement with the large eddy simulation and the available experimental data. Time accurate URANS simulations are performed at high angles of attack in order to achieve converged steady-state results. The main conclusion of this paper is that flows at low-Reynolds number and the peculiar phenomenon of the laminar separation bubbles can be simulated by the RANS approach. As the angle of attack increases and a converged solution is not easily recovered, time-accurate URANS simulations need to be performed. The choices of the turbulence model and of a proper transition location in the model itself resulted crucial. The k-ω SST-LR model and an empirical criterion for the transition location have provided satisfactory results at least for the test-case presented in this paper.

Hasan et al. [12] had discussed the shock induced oscillation around an airfoil in transonic internal flow fields are often observed due to complex shock wave boundary layer interaction. However, in actual flow where finite amount of water vapor is present in the air, the rapid expansion of the flow may give rise to non-equilibrium condensation. Effects of condensing moist air on unsteady shock induced oscillation were numerically studied for total back pressure to reservoir pressure ratios of 0.73-0.65. Results showed that in case with condensing moist air flows, the root mean square of the

shock induced pressure oscillation and the oscillation frequency were reduced significantly compare with those without the non-equilibrium condensation. However, there was an increase of total pressure loss for condensing moist air flows.

In the paper of Xiong et al [13], the performance of four different turbulence models in addressing shock wave-boundary layer instabilities is investigated. The problem chosen for this goal is a transonic flow over a 10% thick circular arc airfoil in a channel. The self-excited shock motion over the circular arc airfoil has been investigated before experimentally and those results are used as a benchmark for the current study. Unsteady RANS and DES methods in combination with different turbulence models are used. All the method can successfully predict the overall shock oscillatory behavior. Yet there are minor differences in frequency prediction. Another reason for choosing this problem is to better understand the physics governing the problem. It is found that the shock oscillation frequency strongly depends on mean shock wave location. All the turbulence models successfully capture the oscillatory behavior of the flow in a certain pressure range, even though the pressure does not completely match the experiments. S-A model seems to be under-predicting the oscillation frequency in comparison to the other methods. Also perfect match between shock wave location and frequency was observed. It seems that to have the numerical solution match the experiments, special attention must be paid to predict the shock wave location precisely on the airfoil. This in turn signifies the inlet profile boundary condition as a potent field for future studies. At the current stage the models are capable of predicting trends observed in experiment correctly. It is also shown that k-ω SST unlike S-A turbulence model can achieve results as accurate as DES model. Also three dimensional computation of this problem can be very important since all the two dimensional computations predict oscillation frequencies which are 50 to 100 percent higher than the experimental results. This means that there might be three dimensional mechanisms that govern the oscillation frequency.

Bendiksen [14] reviewed unsteady transonic flow theory and classical results from the non-linear asymptotic theory are combined with new results from computational fluid dynamics. The emphasis is on application to the field of aeroelasticity and on clarifying the limitations of linearized theories in problems involving mixed subsonic-supersonic flows. The inherent differences between non-linear transonic aerodynamics and linear subsonic and supersonic aerodynamics are considered from a theoretical and computational standpoint, and the practical implications of these differences in formulating suitable aerodynamics models for aeroelastic stability calculations are discussed. Transonic similarity principles are reviewed and their relevance in understanding flutter, divergence, and control reversal phenomena of transonic aircraft is illustrated through practical example. Transonic flutter is rich in non-linear dynamic phenomena that cannot simply be modeled with ideas based on linear aerodynamics. Superficially, the dynamics may appear to the non-linear behaviors of classical mechanical systems, but there are important mathematical and physical differences. First,

aero-elastic systems are essentially non-conservative involving circulatory forces and cannot be modeled simply as dissipative mechanical spring-mass-damper systems, with a damping that becomes negative as the flutter boundary are crossed. Second, in the transonic case entropy production at the moving shocks introduces a type of irreversibility that is not found in the corresponding mechanical system, and which results in entropy and vorticity waves being convected downstream , affecting the global aerodynamics solution and possibly also the stability of the fluid structure system. In transonic flutter, non-uniformities on the time scale affect stability by destroying time invariance.

Yagiz et al [15] had discussed the predictability of weakening the shock wave and hereby reducing the wave drag in transonic flight regime using flow control devices such as two-dimensional contour bump, individual jet actuator, and also the hybrid control which control devices together , and thereby to gain the desired improvements in aerodynamic performance of air-vehicle. To validate the numerical study, an efficient gradient based numerical study, a natural laminar flow airfoil, Rae5243, is chosen and then comparisons with experimental data have been made before the optimization technique is used to optimize 2D bump parameters including the length, the maximum height, the bump position via shock location, and the crest position via bump and also the jet actuation parameters such as mass flow coefficient. Suction/blowing angle, actuation location over the upper surface of the airfoil. The process generally consists of using the simulation code to obtain a flow solution for given parameters and then search the optimum parameters to reduce the total drag of the airfoil via the optimizer. Most importantly, it is shown that, the optimization yields 3.94% decrease in the total drag and 5.03% increase in lift, varying the design parameters of active and passive control devices.

Eleni et al [16] had done the analysis of the two dimensional subsonic flow over a National Advisory Committee for Aeronautics (NACA) 0012 airfoil at various angles of attack and operating at a Reynolds number of 3×10^6 is presented. The flow was obtained by solving the steady-state governing equations of continuity and momentum conservation combined with one of three turbulence models (Spalart-Allmaras, Realizable k-ε and k-ω shear stress transport (SST)) aiming to the validation of these models through the comparison of the predictions and the free field experimental measurements for the selected airfoil. The aim of the work was to show the behavior of the airfoil at these conditions and to establish a verified solution method. The computational domain was composed of 80000 cells emerged in a structured way, taking care of the refinement of the grid near the airfoil in order to enclose the boundary layer approach. Calculations were done for constant air velocity altering only the angle of attack for every turbulence model tested. This work highlighted two areas in computational fluid dynamics (CFD) that require further investigation: transition point prediction and turbulence modeling. The laminar to turbulent transition point was modeled in order to get accurate results for the drag coefficient at various Reynolds numbers. In addition, calculations showed that the

turbulence models used in commercial CFD codes does not give yet accurate results at high angles of attack.

Eventually Lee [17] suggested a physical mechanism of the periodic shock motion based on the study of Tijdeman [2]. The mechanism is explained considering the flow downstream of the shock is fully separated. The mechanism suggested in this study is described in section 1.2. The complete understanding of the mechanisms responsible for self-sustained oscillations of the shock waves under wide ranges of conditions, such as Mach number, incidence angle, Reynolds number, and airfoil geometry has not yet been achieved. A detailed investigation of flow field is carried out for both symmetrical airfoils at zero incidence and supercritical airfoil at incidence. The results show that there are narrow ranges of Mach numbers where shock oscillations can occur on the upper and lower surfaces of the airfoil.

Alshabu and Olivier [18] experimentally investigated the wave phenomena around a supercritical BAC3-11 airfoil in Mach numbers 0.65 to 0.8 at zero incidence angle. Time-resolved shadowgraphs and Schlieren pictures showed pressure waves initiated near the trailing edge and propagating upstream, where they become apparently weaker near the leading edge. These wave processes were accompanied by wake fluctuations and vortex generation in the boundary layer. The observed waves were also captured by pressure transducers mounted in the airfoil model. The dominant frequencies ranged between approximately 0.7 and 1.5 kHz. Using statistical analysis of the pressure histories, wave propagation direction and wave speed were determined. For higher flow Mach numbers, a strong wave/shock interaction was also observed in which the shock, depending on the shock strength, was attenuated and degenerated into compression waves.

Zhao et al [19] performed an experimental study on shock wave oscillations over SC (2)-0714 supercritical airfoil. The experiment was executed in the NPU NF-6 transonic wind tunnel at free stream Mach number from 0.72 to 0.82. Reynolds number based on the airfoil chord was changed from approximating 3.0 million to 5.0 million with transition strip fixed at 28% chord length. The result included spectrogram result at different x/c position under several angles of attack. Results showed that reduced frequency had increased from 0.44 to 0.63 when the angle of attack had increased. The spectrum graph had some low frequency oscillation appeared. It might be caused by background turbulence and unsmooth of the model surface. The cross-correlation coefficients of pressure fluctuations of several Kulite transducers on the upper surface were used to calculate the pressure wave's propagation upstream within the separation region between the shock wave and the airfoil trailing edge.

Very recently, the interaction between the shock wave and the turbulent boundary layer was investigated over OAT15A supercritical airfoil Srator et. al [20]. In agreement with previous results, it was found that the buffet phenomenon was driven by an unstable global mode of the linearized Navier-Stokes equations. Analysis of the adjoin global mode revealed that the flow was most receptive to harmonic forcing on the suction side of the profile, within the boundary layer upstream of the shock foot. An Eigen value sensitivity analysis showed that a steady stream wise force applied either in the boundary layer or in the recirculation region, a steady cooling of the boundary layer, or a steady source of eddy viscosity (a mechanical vortex generator for example) all led to stabilization of the buffet mode. Finally, pseudorsonance phenomena have been analyzed by performing a singular-value decomposition of the global resolvent, which revealed that, besides the low-frequency shock unsteadiness, the flow also underwent medium-frequency unsteadiness, linked to Kelvin-Helmholtz type instability. Such results were reminiscent of the medium- frequency perturbations observed in more traditional shock wave/boundary-layer interactions.

Qin et al. [21] numerically demonstrated the effectiveness of some active shock control mechanism such as suction and injection. A brief description of the flow model and the numerical method is presented including, in particular, the boundary condition modelling and the numerical treatment for surface mass transfer. The effects of surface suction, blowing, and local modification of the surface contour (bump) on aerofoil aerodynamic performance have been studied extensively regarding the control location, the mass flow strength and the bump height.

Stanewski [22] investigated various conventional and novel means of boundary layer and flow control applied to moderate-to-large aspect ratio wings, delta wings and bodies with the specific objectives of drag reduction, lift enhancement, separation suppression and the improvement of air-vehicle control effectiveness. In addition, adaptive wing concepts of varying complexity and corresponding aerodynamic performance gains were discussed, also giving some examples of possible structural realizations. Numerous devices for lift enhancement and separation suppression had been successfully investigated among them trailing-edge devices, such as Gurney flaps, divergent trailing edges, reversed-flow flaps and taps, conventional and sub-boundary-layer and air-jet vortex generators, and mass-less jets. For shock control the contour bump and discrete slot suction upstream of the shock-in that order-were found to be most effective when drag reduction is the main objective.

Effectiveness in reducing drag was found similar to the much more complex wing upper-surface adaptation.

Li et al. [23] proposed micro-blowing as another flow control technique. The interaction of cross flows over micro-porous walls composed of micro-channels with the flows through the channels was simulated by solving the Navier-Stokes equations, and k-ω/SST closure model was employed for the turbulent cross flows. Preliminary results had demonstrated that the effects of micro-blowing on the flow field were limited within the viscous sublayer of the cross flows, and the influential zone was confined in a small region surrounding the porous zone. The study confirmed that promising features on frictional drag reduction could be realized by micro-blowing technique. The capacity of drag reduction was found to be proportional to the blowing fraction. The reduction of frictional drag could even be achieved with zero blowing, implying that the micro-holes gave little effect to the surface roughness of the wall, but were capable of steepening the velocity profiles, i.e., lessening the normal velocity gradients near the wall.

Among passive control techniques, micro-ramps, bumps and cavities were demonstrated as promising control mechanisms [24, 25, 26].

Ashill et al [26] proposed to control the flow in the region of shock wave by locally altering the aerofoil or wing boundary conditions. He proposed to deploy bumps or ramps as variable-geometry devices. It was found that shock control bump offered significant benefits in controlling flows over highly swept wings suitable for combat aircraft, providing a reduction in lift dependant drag of up to 16%. The use of bumps or ramps in the region of the shock, either as fixtures or as active devices, provided significant reductions in drag typically about 12%. A buffet bump placed downstream of the shock could provide significant increases in lift coefficient for buffet onset, while not increasing drag at cruise conditions.

The optimum size, shape and location of the shock control bump have been investigated in References [27, 28]. Patzold et al. analyzed 2d–optimized shock control bumps for the unswept and swept wing. The finite span SCBs consisted of three regions, a luff side step region, a linear part, and a leeward step region. Stream wise SCB contours were either determined in a 2d optimization or individually optimized for the various finite span SCBs. While these SCB contours showed rather good performance in the unswept case, only around 25% efficiency was achieved with wing sweep. For the oblique flow case SCB contours were individually optimized at two span wise locations for finite SCBs with varying span wise

extensions. The SCB–efficiency was significantly increased by adapting the span wise contours. Unlike the unswept case no increased aerodynamic efficiency was observed for span wise small SCBs. The finite span SCB with a width of b_{SCB} = 0.5 c had around 50 to 55 % efficiency. For these span wise small SCBs the efficiency could be increased by reducing, or if so optimizing, the sizes of the luff and leeward step regions. Tian et al. studied the effect of shock control bump on supercritical airfoil RAE2822. Based on improving the airfoil's lift-drag ratio, the study showed that, (1) the best bump crest position was at the position close to 50% of bump chord, which was almost independent of free stream or pre-shock Mach numbers, but the bump height was highly coupled with the crest position, which meant that the higher the bump was, the more obviously the crest position affected the airfoil lift-drag ratio, and it became more evident with the increase of free stream or pre-shock Mach numbers; (2) in case that the lift-drag ratio of airfoil with bump was higher than basic airfoil, almost all the optimum distances between bump crest and shock wave were close to 30% of bump chord; (3) almost all the lift-drag ratios of airfoil with bump increased as bump chord length increased, of which this trend became more evident as bump height increased; (4) with the increase of the bump height, almost all the lift-drag ratios of airfoil with bump decreased at low free stream or pre-shock Mach numbers.

Mazaheri et al [29] investigated two different strategies for bump optimization. One with constant angle of attack and the other with constant lift coefficient. They found that the former design provides an optimum aerodynamic performance while the latter one provides optimum level flight. The survey was conducted for three airfoils through detailed SCB shape optimization processes employing differential evolution algorithm (DE). All optimization and analysis were mainly presented for airfoil RAE2822, but two other airfoils (i.e. NACA 64A010 and RAE 5243) were also studied to show that results are extendable to most transonic airfoils. SWBLI was analysed thoroughly for clean and bumped airfoils and it is shown how the modified wave structure originating from upstream of SCB reduces the wave drag while simultaneously improving the boundary layer velocity profiles downstream of the shock wave. It was shown that how the shock wave interacts with the boundary layer on the SCB and how the isentropic wave pattern generated by the SCB weakened the shock wave and energizes the boundary layer in the recovery region. This prohibited boundary layer growth, and delayed separation. A detailed analysis of the velocity profiles in the boundary layer was used to compare clean airfoil with constant angle of attack and constant CL optimized bumped airfoils. The analysis was extended to the structure of the wake region, to

show how the optimized shape, especially the constant CL case, produced more symmetric and uniform velocity.

The capability of shock control bump in controlling shock wave oscillation has also been reported by Hasan and Alam [30]. Self-excited shock induced oscillation (SIO) around an airfoil was observed in transonic flows at certain conditions of free stream Mach number and angle of attack. At these conditions, the interaction of unsteady shock wave with airfoil boundary layer became complex and caused several detrimental effects such as the fluctuating lift and drag coefficients, aero acoustic noise and vibration, high cycle fatigue failure (HCF), buffeting and so on. In the study, Reynolds Averaged Navier-Stokes equations had been used to predict the aerodynamics behaviour over a NASA SC(2) 0714 supercritical airfoil in transonic flow conditions. To suppress the unsteady aerodynamic behaviour, a shock control bump was introduced at the mean shock position. Computations had been performed at free stream Mach number of 0.77 while the angle of attack was varied from 2° to 7°. The results obtained from the numerical computation had been validated with the experimental results. Mach contour, lift and drag coefficient, and pressure history over the airfoil surface had been analyzed for the cases of baseline airfoil and airfoil with bump. It is found that, the bump could control the unsteady SIO in the flow field.

Another promising shock control technique is the shock control cavity which is not well explored until now. McComick [31]. described an experimental comparison of two passive approaches for controlling the shock interaction with a turbulent boundary layer: low-profile vortex generators and a passive cavity (porous wall with a shallow cavity underneath). The experiments were conducted with a normal shock wave in an axi-symmetric wind tunnel. The shock strength (M = 1.56-1.65) was of sufficient magnitude to induce a large separation bubble, thus causing substantial boundary-layer losses. The low-profile vortex generators were found to significantly suppress the shock-induced separation and improve the boundary-layer characteristics downstream of the shock. However, the suppression of the separation bubble decreased the extent of the low total pressure loss region associated with the lambda foot shock system which results in a lower mass-averaged total pressure downstream of the shock. The passive cavity substantially reduced the total pressure loss through the shock system (and thus wave drag) by causing a more isentropic compression over a larger lateral extent. However, the boundary-layer losses downstream of the shock were significantly increased. The two methods offered different advantages and disadvantages. For example, if wave drag reduction of an isolated airfoil was required, then the passive cavity approach was

favoured. However, if a supersonic diffuser was the application then the vortex generator approach was probably favoured because the shock-induced separation, which usually limits diffuser performance, was suppressed allowing more subsonic pressure recovery to be obtained.

Smith et al. [32] performed the Reynolds Averaged Navier-Stokes computations of groove controlled and uncontrolled shock wave / boundary layer at a Mach number of 1.29, and the results validated against experiment. Features of the uncontrolled interaction were accurately captured, including the upstream influence, static pressure rise, and the effect of shock structure on downstream total pressure losses. The main features of the groove controlled interaction were also predicted by the RANS solver and the interaction featured a large lambda type structure with an oblique leading leg and a curved rear leg separated by a region of expansion. These expansion waves were a result of boundary layer relaxation over the groove. The expansion waves were responsible for the curved, nearly normal rear leg of the shock structure, which increased total pressure losses downstream of the interaction and reduced the beneficial effects of control. Two pairs of counter rotating vortices were detected in the interaction. The origins of one pair of vortices was found to be at the leading edge of the grooves and was formed due to a roll up fluid blown from the groove. The second pair of counter rotating vortices was also a result of transpiration from the groove. Blowing from the groove produced a flow separation, leading to the formation of a vortex pair. These vortices were found to move over the groove at a stream wise location which corresponded to reduced transpiration from the control. This reduced transpiration was responsible for the relaxation of the boundary layer.

Rowley and Williams [33]. reviewed the significant progress in understanding and controlling cavity flow oscillations that was made in the past few decades. Early experiments used passive techniques, open-loop forcing, or closed-loop forcing with only the broadest heuristics to guide the control design. In the review closed-loop control had demonstrated the potential for reduction in oscillations with an order of magnitude less power required, and adaptive controllers had demonstrated control over a range of flow conditions. They suggested that the development of better control-oriented models, and the validation of these models with careful experiments and simulations, can help to fill these gaps in our understanding, and enable the benefits experienced in the laboratory to be achieved at full scale.

Olsman and Colonius [34] performed two-dimensional direct numerical simulation of the flow over a NACA0018 airfoil with a cavity. The low Reynolds number simulations were validated by means of flow visualizations carried out in a water channel. From the simulations, it followed that there were two main regimes of flow inside the cavity. Depending on the angle of attack, the first or the second shear-layer mode (Rossiter tone) was present. The global effect of the cavity on the flow around the airfoil was the generation of vortices that reduced flow separation downstream of the cavity. At high positive angles of attack, the flow separates in front of the cavity, and the separated flow interacted with the cavity, causing the generation of smaller-scale structures and a narrower wake compared with the case when no cavity was present. At certain angles of attack, the numerical results suggested the possibility of a higher lift-to-drag ratio for the airfoil with cavity compared with the airfoil without cavity. The simulations have revealed interesting flow physics associated with the interaction of no less than three different types of instabilities. These are the first- and second-cavity shear-layer modes and separation bubble behavior, which is forced by a shear-layer oscillation.

Very recently, an investigation for self-excited shock oscillation around a biconvex circular arc airfoil in transonic internal flows has been performed by Rahman et al [35]. The upstream Mach number is kept at 0.61 while the airfoil was at zero angle of attack. The computational results are validated with available experimental data. In case of baseline airfoil, the self-excited shock oscillation is observed for all the cases of pressure ratio 0.71 to 0.75. The self-excited shock oscillation disappears and shock wave remains steady with the introduction of cavity in the airfoil surfaces for pressure ratio 0.71. Amplitude of pressure oscillation in the flow field is reduced in case of airfoil with cavity at pressure ratio 0.72 to 0.75. The RMS of pressure oscillation significantly reduced throughout the flow field in case of airfoil with cavity. However, frequency of shock oscillation increases for the case of airfoil with cavity compared to baseline airfoil.

The passive control by surface modification was demonstrated experimentally by Bahi et al. [38]. This study includes experimentation of a porous surface and a cavity or plenum underneath. The control device is installed in the region of shock boundary layer interaction. It is suggested that the pressure rise across the shock wave will results in flow through the cavity from downstream to the upstream of the shock. This is equivalent to a combination of suction of downstream and blowing of upstream. The cavity could also increase the communication of signals across the shock wave. These

effects could lead to a rapid thickening of boundary layer just ahead of the shock which produces a system of weaker shock with a extended interaction zone.

Then many researchers studied the effect of surface modification of airfoil to control the shock oscillations, high speed impulsive (HIS) noise etc. Nagamatsu et al. [39] experimentally studied the transonic flow over airfoil and investigated the effect of perforated cavity on drag minimization. The same results were obtained by Raghunathan et al. [40], suggesting a secondary reverse flow through the cavity. This study shows that perforated cavity can be used effectively only for strong shock wave.

Doerffer et al. [41] investigated the effect of perforated cavity on high speed noise reduction for a high speed helicopter rotor. This study concluded that the perforated cavity can lower the pressure fluctuation on the airfoil surface and thus the high speed noise is reduced. Yamamoto et al. [42] investigated a self excited oscillation of transonic flow in a simplified cascade model. The study includes experimental, numerical and theoretical analysis. The results predicted a close loop mechanism of self sustained oscillation as proposed by Lee [17]. The conclusion of this study include that the flow field is more stable acoustically when the shock wave stands near the trailing edge because for this case generation of much larger pressure wave is necessary for shock oscillation.

Hamid et al. [44] studied the internal flow over a 12% thick airfoil and showed that the variation of flow characteristics and shock oscillation is dependent on the downstream pressure of the airfoil. The study shows that a clean biconvex circular arc airfoil (with no control technique) operating at pressure ratio (ratio of back pressure to upstream total pressure) 0.70 results a discontinuous shock oscillation which is known as Tijdeman type B shock oscillation.

CHAPTER 3

COMPUTATIONAL METHOD

3.1 BASICS OF CFD

Computational fluid dynamics constitutes a new third approach in the philosophical study and development of the whole discipline of fluid dynamics. The advent of the high speed digital computer combined with the development of accurate numerical algorithms for solving physical problems on these computers has revolutionized the way we practice fluid dynamics today. Computational fluid dynamics is today an equal partner with pure theory and pure experiment in the analysis and solution of fluid dynamics problems. There is no doubt that computational fluid dynamics will continue to play this role indefinitely.

Applying the fundamental laws of mechanics to a fluid gives the governing equations for a fluid. The conservation of mass equation is

$$\frac{\partial \rho}{\partial t} + \nabla.(\rho \vec{v}) = 0 \qquad (3.1.1)$$

and the conservation of momentum equation is

$$\rho \frac{\partial \vec{V}}{\partial t} + \rho(\vec{V}.V)\vec{V} = -\nabla p + \rho \vec{g} + \nabla.\tau ij \qquad (3.1.2)$$

These equations along with the conservation of energy equation form a set of coupled, non- linear partial differential equations. It is not possible to solve these equations analytically for most engineering problems. However, it is possible to obtain approximate computer-based solutions to the governing equations for a variety of engineering problems. This is the subject matter of Computational Fluid Dynamics (CFD).

3.2 APPLICATIONS OF CFD:

CFD is useful in a wide variety of applications and here is a few note to give you an idea of its use in industry.

1. CFD can be used to simulate the flow over a vehicle. For instance, it can be used to study the interaction of propellers or rotors with the aircraft fuselage.
2. The CFD analysis showed the effectiveness of a simpler manifold design without the need for field testing.
3. Bio-medical engineering is a rapidly growing field and uses CFD to study the circulatory and respiratory systems.
4. CFD is attractive to industry since it is more cost-effective than physical testing. However, one must note that complex flow simulations are challenging and error-prone and it takes a lot of engineering expertise to obtain validated solutions.

3.3 FUNDAMENTAL EQUATIONS

The most complete model of the flow of air is the two-dimensional Navier Stokes equations. They represent the three conservation laws:

1. Conservation of mass

$$\frac{\partial \rho}{\partial t} + \frac{\partial (\rho u)}{\partial x} + \frac{\partial (\rho v)}{\partial y} = 0 \tag{3.3.1}$$

2. Conservation of momentum

$$\frac{\partial (\rho u)}{\partial t} + \frac{\partial (\rho u^2)}{\partial x} + \frac{\partial (\rho uv)}{\partial y} = \frac{\partial \tau_{xx}}{\partial x} + \frac{\partial \tau_{xy}}{\partial y} \tag{3.3.2}$$

$$\frac{\partial (\rho v)}{\partial t} + \frac{\partial (\rho v^2)}{\partial x} + \frac{\partial (\rho uv)}{\partial y} = \frac{\partial \tau_{xy}}{\partial x} + \frac{\partial \tau_{yy}}{\partial y} \tag{3.3.3}$$

3. Conservation of energy

$$\frac{\partial (\rho E)}{\partial t} + \frac{\partial (\rho uE)}{\partial x} + \frac{\partial (\rho vE)}{\partial y} = \frac{\partial (\rho q)}{\partial t} + \frac{\partial (\rho uq)}{\partial x} + \frac{\partial (\rho vq)}{\partial y} + [\frac{\partial}{\partial x}(u\tau_{xx} + v\tau_{xy}) + \frac{\partial}{\partial y}(u\tau_{xy} + v\tau_{yy})] \tag{3.3.4}$$

They are not the physical truth because they involve a number of statistical quantities such as viscosity and density.

3.4 STRATEGY OF CFD:

The strategy of CFD is to replace the continuous problem domain with a discrete domain using a grid. In the continuous domain, each flow variable is defined at every point in the domain. For instance, the pressure *p* in the continuous 1D domain shown in the figure below would be given as

$p = p(x),\ 0 < x < 1$

In the discrete domain, each flow variable is defined only at the grid points. So, in the discrete domain shown below, the pressure would be defined only at the N grid points.

$P_i = p(x_i),\quad i = 1, 2, \ldots, N$

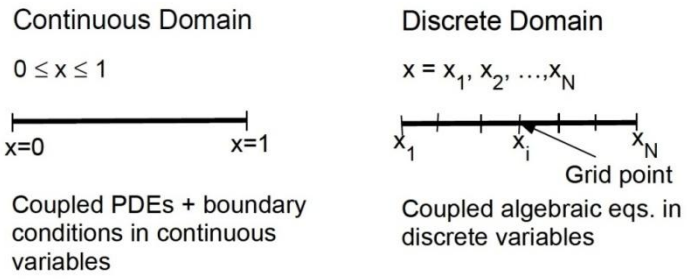

In a CFD solution, one would directly solve for the relevant flow variables only at the grid points. The values at other locations are determined by interpolating the values at the grid points.

The governing partial differential equations and boundary conditions are defined in terms of the continuous variables *p, V* etc. One can approximate these in the discrete domain in terms of the discrete variables p_i , V_i etc. The discrete system is a large set of coupled, algebraic equations in the discrete variables. Setting up the discrete system and solving it (which is a matrix inversion problem) involves a very large number of repetitive calculations, a task we humans palm over to the digital computer.

This method of deriving the discrete equation using Taylor's series expansions is called the finite-difference method. However, most commercial CFD codes use the finite-volume or finite-element methods which are better suited for modeling flow past complex geometries.

3.5 DISCRETIZATION USING FINITE VOLUME METHOD

The finite volume method is a method for representing and evaluating partial differential equations in the form of algebraic equations. Similar to the finite difference method or finite element method, values are calculated at discrete places on a meshed geometry. "Finite volume" refers to the small volume surrounding each node point on a mesh. In the finite volume method, volume integrals in a partial differential equation that contain a divergence term are converted to surface integrals, using the divergence theorem. These terms are then evaluated as fluxes at the surfaces of each finite volume. Because the flux entering a given volume is identical to that leaving the adjacent volume, these methods are conservative. Another advantage of the finite volume method is that it is easily formulated to allow for unstructured meshes. The method is used in many computational fluid dynamics packages.

The integral conservation equation are written for a discrete volume,

$$\frac{\partial}{\partial x}\iiint U d\Omega + \oint_S F.dS = \iiint Q d\Omega \tag{3.5.1}$$

and applied to control volume Ω_J, when the discretized equation associated with U_J is to be defined. This equation can be replaced by the discrete form,

$$\frac{\partial}{\partial x}\left(U_J \Omega_J\right) + \sum_{sides}(F.S) = Q_J \Omega_J \tag{3.5.2}$$

where the sum of the flux terms refers to all the external sides of the control cell Ω_J. This is the general formulation of the finite volume method, and the user has to define, for a selected Ω_J, how to estimate the volume and cell face areas of the control volume Ω_J and how to approximate the fluxes at the faces.

The following constraints on the choice of the choice of the Ω_J volumes for a conservative finite volume method have to be satisfied:

1. The sum should cover the whole domain Ω;
2. Adjacent Ω_J may overlap if each internal surface is common to two volumes;
3. Fluxes along a cell surface have to be computed by formulas independent of the cell in which they are considered.

The first term of equation (3.9) represents the time rate of change of the averaged flow variable over the selected finite volume. In absence of source terms, the finite volume formulation expresses that the variation of the average value U over the time interval Δt is equal to the sum of the fluxes

exchanged between neighboring cells. For stationary flows the numerical solution is obtained as a result of balance of all the fluxes entering the control volume. That is,

$$\sum_{sides} (F.S) = 0 \qquad (3.5.3)$$

Physically, this equation means that the net volume flow into the control volume is zero. Here is a rectangular cell shown below.

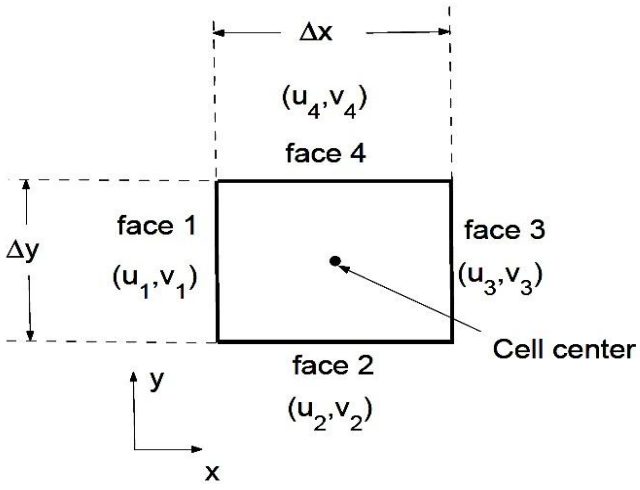

The velocity at face i is taken to be $V_i = u_i\ i + v_i\ j$. Applying the mass conservation equation to the control volume defined by the cell gives

$$-u_1 \Delta y - v_2 \Delta x + u_3 \Delta y + v_4 \Delta x = 0 \qquad (3.5.4)$$

This is the discrete form of the continuity equation for the cell. It is equivalent to summing up the net mass flow into the control volume and setting it to zero. So it ensures that the net mass flow into the cell is zero i.e. that mass is conserved for the cell. Usually, though not always, the values at the cell centers are solved for directly by inverting the discrete system.

The face values u_1, v_2, etc. are obtained by suitably interpolating the cell-center values at adjacent cells. Similarly, one can obtain discrete equations for the conservation of momentum and energy for the cell. One can readily extend these ideas to any general cell shape in 2D or 3D and any conservation equation.

The code finds solution such that mass, momentum, energy and other relevant quantities are being conserved for each cell. Also, the code directly solves for values of the flow variables at the cell centers; values at other locations are obtained by suitable interpolation.

3.6 DISCRETIZATION OF THE DOMAIN

1. The vertex data of the biconvex (base case) was imported and connected using NURBS. Here the length of the chord *c* is 0.048 m. It can be done in another way using Gambit locating the three points on each surfaces and draw the airfoil using circular arc provision.

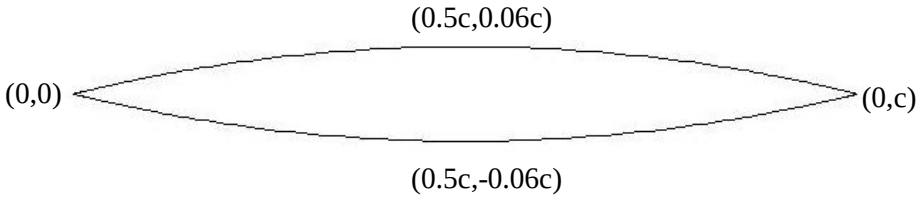

Figure 3.6.1: Base airfoil surfaces with vertex data points

2. A local coordinate is applied where the leading edge (LE) at (0,0) and the trailing edge is at (c,0).
3. The inlet is at a distance five times of the chord (5c) to the left. The tunnel dimension is equal to the chord length (c). The tunnel is extended up to 2c distance from the trailing edge towards right. The outlet is at 50c distance beyond the end of the tunnel. The outlet tunnel dimension is 51c and spread evenly on the both side of the airfoil axis.

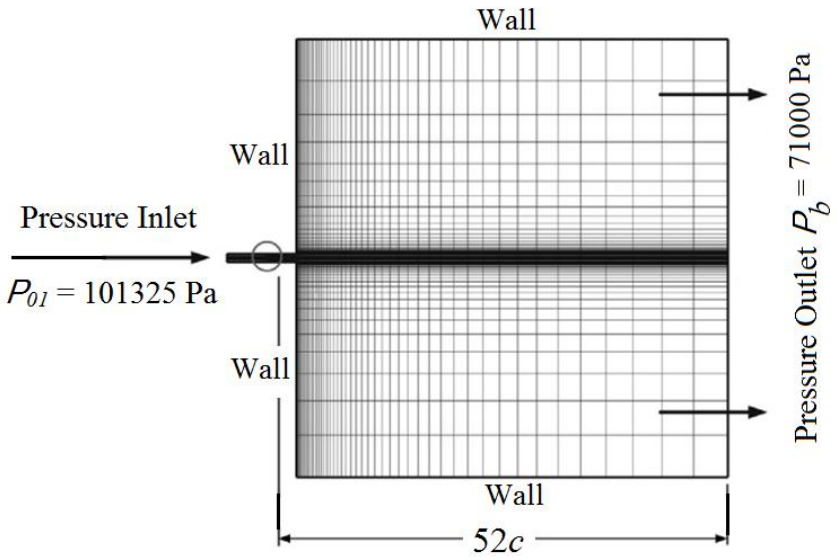

Figure 3.6.2: Computational domain

The matter of grid generation is a significant consideration in CFD. The generation of an appropriate grid or mesh is one thing, the solution of the governing flow equations over such a grid is quite another thing .Quadrilateral cells were used for this simple geometry because they can be stretched easily to account for different flow gradients in different directions. 250 points have been taken on both the surfaces of the airfoil. Consequently, the cells near the

surface have high aspect ratios. For viscous flow over the airfoil, finely spaced grid was constructed to calculate the details of the flow near the airfoil.

4. Those points are located on each surface for the acceptable average y^+ values less than unity. This type of grid is usually used for the study of various airfoils.

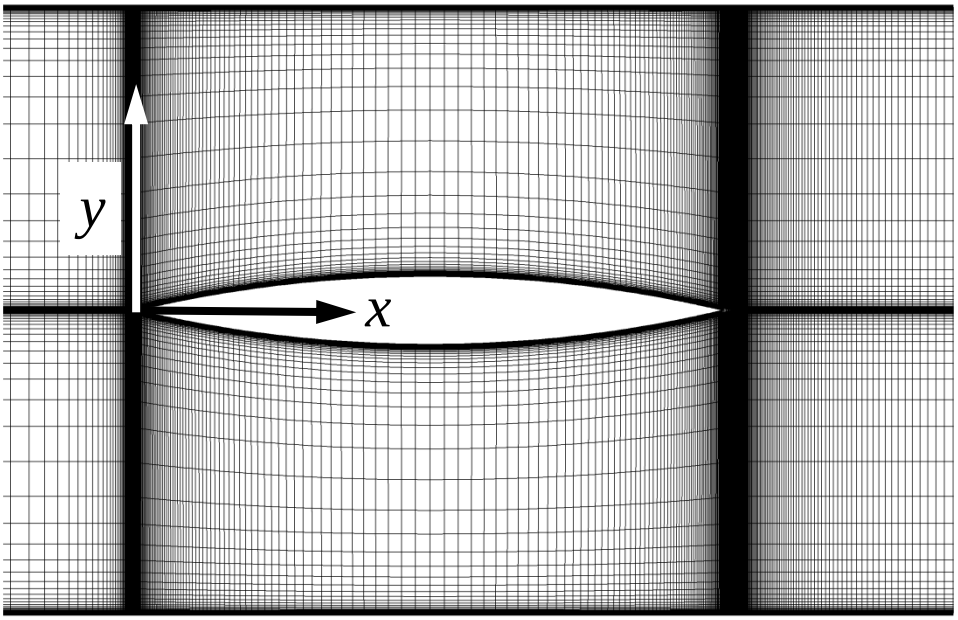

Figure 3.6.3: Grid closed-up look for 12% biconvex airfoil (Base airfoil)

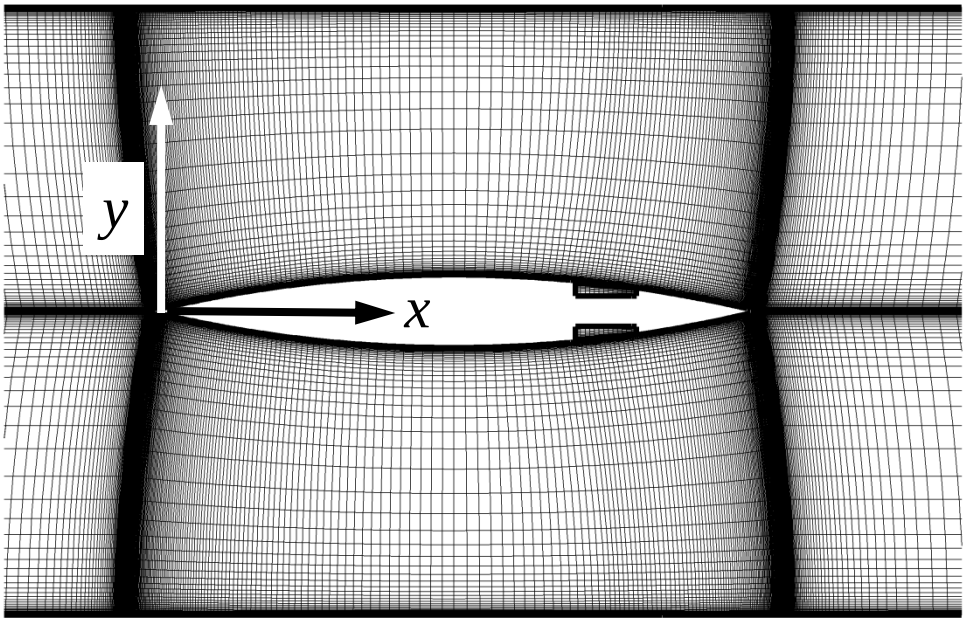

Figure 3.6.4: Grid closed-up look for 12% biconvex airfoil with cavity

3.7 SOLVER SETTING

CFD allows to choose one of the two numerical methods:

- Pressure-based solver
- Density-based solver

The pressure-based approach was developed for low-speed incompressible flows, while the density-based approach was mainly used for high-speed compressible flows. However, recently both methods have been extended and reformulated to solve and operate for a wide range of flow conditions beyond their traditional or original intent.

In both methods the velocity field is obtained from the momentum equations. In the density based approach, the continuity equation is used to obtain the density field while the pressure field is determined from the equation of state. On the other hand, in the pressure-based approach, the pressure field is extracted by solving a pressure or pressure correction equation which is obtained by manipulating continuity and momentum equations. Using either method, the present CFD tool will solve the governing integral equations for the conservation of mass and momentum, and for energy and other scalars such as turbulence and chemical species. In present numerical analysis density based solver is used. Detailed solver settings are shown below:

Solver Setting		Viscous Model	
Solver	Coupled	Model	k-ω (2 eqn)
Space	2D	k-ω model	SST
Gradient Option	Cell-based	k-ω option	N/A
Formulation	Implicit	Turbulent viscosity	none
Time	Unsteady	Viscous Heating	N/A

Table 3.7.1: solver settings

3.7.1 Discretization Scheme

For Density, Momentum, Turbulent Kinetic Energy, Specific Dissipation Rate, Energy equations have First Order Upwind, Second Order Upwind, QUICK and Third-Order MUSCL. schemes. For all cases Second Order Upwind schemes were selected. When the flow is aligned with the grid (e.g., laminar flow in a rectangular duct modeled with a quadrilateral or hexahedral grid) the first-order upwind discretization is acceptable. When the flow is not aligned with the grid (i.e., when it crosses the grid lines obliquely), however, first order convective discretization increases the numerical discretization

error (numerical diffusion). For triangular and tetrahedral grids, since the flow is never aligned with the grid, generally more accurate results are obtained by using the second-order discretization. For quad/hex grids, better results using the second-order discretization is obtained, especially for complex flows.

3.7.2 The Density Based Algorithm:

Density based solver solves the governing equations of continuity, momentum, energy and species transport simultaneously (coupled together). Governing equations for turbulence and other scalar quantities are solved afterward and sequentially. The steps for density based solver are given bellow:

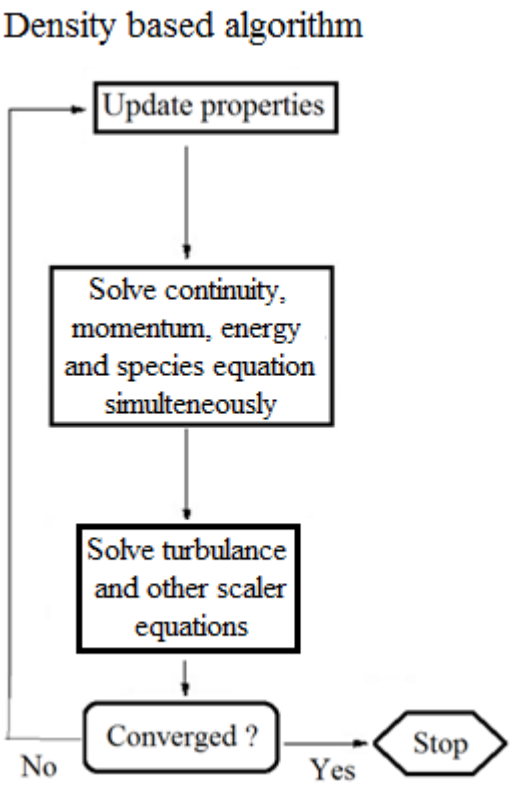

The density based coupled solver solves the turbulence equation sequentially after solving the set of equations of continuity, momentum and energy equations for each node. This density based solver can be used along with either implicit or explicit scheme. The implicit scheme forms a set of linear equations containing all the unknown parameters in all equations for every node. Here each equation consists of both unknown and existing variables. Meanwhile explicit scheme forms a set of linear equations consisting only existing variables. In the present study density based coupled solver has been implied with implicit scheme.

3.8 TURBULENCE MODELING

Turbulent flows are characterized by fluctuating velocity fields. These fluctuations mix transported quantities such as momentum, energy, and species concentration, and cause the transported quantities to fluctuate as well. This approach is referred to as Direct Numerical Simulation (DNS). Another approach is the large eddy simulation (LES), where large scale structure in the flow is directly simulated whereas small scales are filtered out. Due to large computational time and computational research requirements for DNS and to some extent, for LES, these techniques are used more or less for research-oriented applications. Since these fluctuations can be of small scale and high frequency, they are too computationally expensive to simulate directly in practical engineering calculations. So, over the last several decades approximate procedures have been developed which allow us to solve turbulent flow fields. The scheme is based on averaging of the fluid properties whereby the high frequency (small scale) fluctuations are removed. These fluctuating terms are then related to the mean flow properties by relations, which are known as turbulence models.

Instead, the instantaneous (exact) governing equations can be time-averaged, ensemble-averaged, or otherwise manipulated to remove the small scales, resulting in a modified set of equations that are computationally less expensive to solve. However, the modified equations contain additional unknown variables, and turbulence models are needed to determine these variables in terms of known quantities.

A turbulence model is a semi-empirical equation relating the fluctuating correlation to mean flow variables with various constants provided from experimental investigations. These models are developed based on experimental data obtained from relatively simple flows under controlled environment. That in turn limits the range of applicability of turbulence models. When this equation is expressed as an algebraic equation, it is referred to as the zero-equation model. When partial differential equations are used, they are referred to as one-equation or two equation models, depending on the number of PDEs used. Some models employ ordinary differential equations, in which case they are referred to as half-equation models. Finally, it is possible to write a partial differential equation directly for each of the turbulence correlations in which case they compose a system of PDEs known as the Reynolds stress equations.

A number of turbulence models are there to match the conditions like

1. Spalart-Allmaras model
2. k-ε model
3. k-ω model

4. v^2-f model
5. Reynolds Stress model(RSM)
6. Detached Eddy Simulation(DES) model
7. Large eddy simulation (LES) model

3.8.1 *k*-ω two equations Turbulence Model

Convection of turbulence is not modeled in zero-equation models. Therefore the physical effect of past history of the flow is not included in simple algebraic models. In order to account for this physical effect, a transport equation based on Navier-Stokes equation may be derived. When one such equation is employed, it is referred to as a one-equation model. When two transport equations are used, it is known as a two-equation model.

Two different models are there for *k*-ω model. These are

1. Standard
2. Shear Stress Transport (SST)

3.8.1.1 Standard *k*-ω model:

This two equation model includes one equation for the turbulent kinetic energy (*k*), as developed previously and a second equation for the specific turbulent dissipation rate (ω).The standard *k*-ω model is an empirical model based on model transport equations for the turbulence kinetic energy (*k*) and the specific dissipation rate (ω), which can also be thought of as the ratio of ε to *k*.

As the *k*-ω model has been modified over the years, production terms have been added to both the*k* and ω equations, which have improved the accuracy of the model for predicting free shear flows.

The turbulence kinetic energy, *k*, and the specific dissipation rate, ω, are obtained from the following transport equations:

$$\frac{\partial}{\partial t}(\rho k) + \frac{\partial}{\partial x_i}(\rho k u_i) = \frac{\partial}{\partial x_j}\left(\Gamma_k \frac{\partial k}{\partial x_i}\right) + G_k - Y_k + S_k \qquad (3.8.1.1.1)$$

and

$$\frac{\partial}{\partial t}(\rho \omega) + \frac{\partial}{\partial x_i}(\rho \omega u_i) = \frac{\partial}{\partial x_j}\left(\Gamma_\omega \frac{\partial \omega}{\partial x_j}\right) + G_\omega - Y_\omega + S_\omega \qquad (3.8.1.1.2)$$

In these equations, G_k represents the generation of turbulence kinetic energy due to mean velocity gradients. G_ω represents the generation of ω. Γ_k and $\Gamma\omega$ represent the effective diffusivity of *k* and ω,

respectively. Y_k and Y_ω represent the dissipation of k and ω due to turbulence. S_k and S_ω are user-defined source terms.

3.8.1.2 Shear Stress Transport *k*-ω model:

The major ways in which the SST model differs from the standard model are as follows:

1. Gradual change from the standard *k*-ω model in the inner region of the boundary layer to a high-Reynolds-number version of the *k*-ω model in the outer part of the boundary layer.
2. Modified turbulent viscosity formulation to account for the transport effects of the principal turbulent shear stress.

In this computation SST *k*-ω model has been used which uses two equations and has better accuracy than other models of one equation.

The shear-stress transport (SST) *k*-ω model was developed by Menter to effectively blend the robust and accurate formulation of the *k*-ω model in the near-wall region with the free-stream independence of the *k*-ω model in the far field.

To achieve this, the *k*-ε model is converted into a *k*-ω formulation. The SST *k*-ω model is similar to the standard *k*-ω model, but includes the following refinements:

1. The standard *k*-ω model and the transformed *k*-ε model are both multiplied by a blending function and both models are added together. The blending function is designed to be one in the near-wall region, which activates the standard *k*-ω model, and zero away from the surface, which activates the transformed *k*-ε model.
2. The SST model incorporates a damped cross-diffusion derivative term in the ω equation.
3. The definition of the turbulent viscosity is modified to account for the transport of the turbulent shear stress.
4. The modeling constants are different.

These features make the SST *k*-ω model more accurate and reliable for a wider class of flows (e.g., adverse pressure gradient flows, airfoils, transonic shock waves) than the standard *k*-ω model. Other modifications include the addition of a cross-diffusion term in the ω equation and a blending function to ensure that the model equations behave appropriately in both the near-wall and far-field zones.

The SST *k*-ω model has a similar form to the standard *k*-ω model:

$$\frac{\partial}{\partial t}(\rho k) + \frac{\partial}{\partial x_i}(\rho k u_i) = \frac{\partial}{\partial x_j}\left(\Gamma_k \frac{\partial k}{\partial x_j}\right) + \widetilde{G_k} - Y_k + S_k \quad (3.8.1.2.1)$$

and

$$\frac{\partial}{\partial t}(\rho \omega) + \frac{\partial}{\partial x_i}(\rho \omega u_i) = \frac{\partial}{\partial x_j}\left(\Gamma_\omega \frac{\partial \omega}{\partial x_j}\right) + G_\omega - Y_\omega + D_\omega + S_\omega \quad (3.8.1.2.2)$$

In these equations, $\widetilde{G_k}$ represents the generation of turbulence kinetic energy due to mean velocity gradients. G_ω represent the generation of ω. Γ_k and Γ_ω represents the effective diffusivity of *k* and ω, respectively, which are calculated as described below. Y_k and Y_ω represent the dissipation of *k* and ω due to turbulence. D_ω represent the cross-diffusion term. S_k and S_ω are user-defined source terms. These source terms may be implemented for analysis of a scientific problem that composes multi-physical phenomenon.

3.9 TURBULANCE INTENSITY

The turbulence intensity, also referred as turbulence level, is defined as:

$$\mathrm{I} \equiv \frac{u'}{U} \quad (3.9.1)$$

Where u' is the root-mean-square of the turbulent velocity fluctuations and *U* is the mean velocity (Reynolds averaged).

If the turbulent energy (*k*) is known u' can be computed as:

$$u' \equiv \sqrt{\frac{1}{3}\left(u_x'^2 + u_y'^2 + u_z'^2\right)} \quad (3.9.2)$$

U can be computed from the three mean velocity components U_x , U_y and U_z as:

$$U \equiv \sqrt{\left(U_x^2 + U_y^2 + U_z^2\right)} \quad (3.9.3)$$

When setting boundary conditions for a CFD simulation it is often necessary to estimate the turbulence intensity at the inlet. To do this accurately it is good to have some form of measurements or previous experience to estimate. Here are a few examples of common estimations of the incoming turbulence intensity:

High-turbulence cases: These cases include high-speed flow inside complex geometries like heat-exchangers and flow inside rotating Machinery (turbines and compressors). Typically the turbulence intensity is between 5% and 20%

Medium-turbulence case: These cases include flow in not-so-complex devices like large pipes, ventilation flows or low speed flows (low Reynolds number). Typically the turbulence intensity is in between 1% to 5%

Low-turbulence case: These cases include flow originating from a fluid that stands still, like external flow across cars, submarines and aircrafts. Very high-quality wind-tunnels can also reach really low turbulence levels. Typically the turbulence intensity is very low, well below 1%.

3.10 OPERATING CONDITION

Operating pressure is significant for incompressible ideal gas flows because it directly determines the density. Operating pressure is less significant for compressible flows. The pressure changes in such flows are much larger than those in incompressible flows, so there is no real problem with round off error and there is therefore no real need to use gauge pressure. In fact, it is common convention to use absolute pressures in such calculations. Operating pressure has been set to zero making gauge and absolute pressures equivalent.

3.11 BOUNDARY CONDITION

Gauge pressure of 101325 Pa has been selected which is recommended for reasonable accuracy. The temperature has been set at 300 K. The back pressure ratio has been applied as an indication for different flow cases. The whole study has been done for zero angle of attack.

A detailed overview of boundary condition is given below:

Boundary Condition			
	Inlet	Outlet	Wall
Type	Pressure –inlet	Pressure-Outlet	No slip condition
Total Gauge pressure(Pa)	101325	71000	
Temperature(K)	300	300	
Initial Gauge Pressure	99000	----------	
Direction Sprefication Method	Normal-to-Boundary	Normal-to-Boundary	
Turbulence Specification Method	Intensity and Viscosity Ratio	Intensity and Viscosity Ratio	
Turbulece intensity	1%	10%	
Turbulece Viscosity Ratio	10	10	

Table 3.11.1: Overview of boundary conditions

3.12 MATERIAL SELECTION

Fluid Material is air, which is the working fluid in this problem. Here compressibility and variations of the thermo physical properties have been made dependent on temperature. Ideal gas law and intermolecular-force potential Sutherland's law have been set for density and viscosity. While Density and Viscosity have been made temperature dependent, specific heat (c_p) and Thermal Conductivity have been left constant. For compressible flows, thermal dependency of the physical properties is generally recommended. For simplicity, Thermal Conductivity and specific heat (c_p) are assumed to be constant.

3.12.1 SUTHERLAND'S LAW

In 1893 William Sutherland, an Australian physicist, published a relationship between the dynamic viscosity, μ, and the absolute temperature, T, of an ideal gas. This formula, often called Sutherland's law, is based on kinetic theory of ideal gases and an idealized intermolecular-force potential. Sutherland's law is still commonly used and most often gives fairly accurate results with an error less than a few percent over a wide range of temperatures. Sutherland's law can be expressed as:

$$\mu = \mu_{ref} \left(\frac{T}{T_{ref}}\right)^{\frac{3}{2}} \frac{T_{ref} + S}{T + S} \qquad (3.12.1.1)$$

T_{ref} is a reference temperature.

μ_{ref} is the viscosity at the reference temperature

S is the Sutherland temperature

Some authors instead express Sutherland's law in the following form:

$$\mu = \frac{C_1 T^{3/2}}{T + S} \qquad (3.12.1.2)$$

Comparing the formulas above the constant can be written as:

$$C_1 = \frac{\mu_{ref}}{T_{ref}^{3/2}} \left(T_{ref} + S\right) \qquad (3.12.1.3)$$

Sutherland's law coefficients				
Gas	$\mu_0 \left[\frac{kg}{ms}\right]$	T_0 [K]	S [K]	$C_1 \left[\frac{kg}{ms\sqrt{K}}\right]$
Air	1.716×10^{-5}	273.15	110.4	1.458×10^{-6}

3.13 STEADY ANALYSIS

First a steady computation has been performed using steady solver. The steady computation has been done to develop the flow field for further unsteady study. The steady computation was performed until the flow field was fully developed. This computation is done as steady solver requires less time than the unsteady solver.

3.14 UNSTEADY ANALYSIS

The solution obtained from steady solver is used for unsteady case as a reference. Second order implicit formulation has been used for unsteady cases with fixed time stepping method. Time step size has been chosen 10^{-6} sec with 10 iterations per time step.

During the computation the local pressure on the airfoil surface was documented. Total 48 points were monitored to gather the pressure history. The points were evenly distributed over both of the surfaces.

CHAPTER 4

CONTROL WITH OPEN CAVITY

4.1 VALIDATION OF NUMERICAL METHOD

Before going to the detailed discussion, the numerical code is validated with the experimental results. Since the experimental flow structures are available for 15% thick arc airfoil [12], the present simulation was first carried out with the same airfoil for verification of numerical schemes.

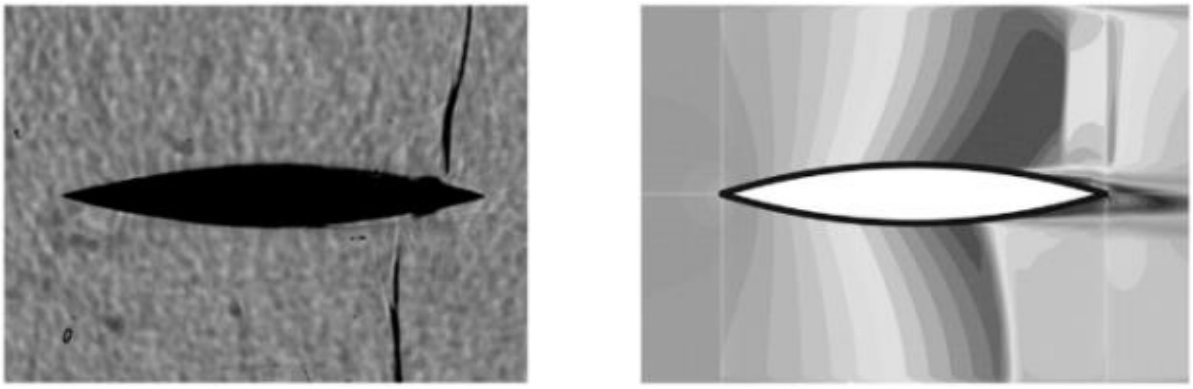

(a) (b)

Fig 4.1.1: Instantaneous flowfield with shock waves. (a) Experimental Schlieren photograph [12] for p_{b0}/p_{01}=0.70 and (b) Mach contour from present computation for p_b/p_{01}=0.69 (15% thick airfoil)

Figure 4.1.1(a) shows the schlieren image obtained from the experiments of Hasan et al [12] for p_{b0}/p_{01}=0.70. The same flow case corresponds to p_b/p_{01}=0.69 which is defined as the pressure ratio (PR, ratio of outlet pressure to inlet pressure) in the present study. The numerically obtained flow field with shock waves is shown in figure 4.1.1(b). It is found that the flow structures are almost similar with two shock waves on both upper and lower surfaces of the airfoil. The shock on upper surface is closer to trailing edge than the shock on lower surface. So the computed flow field is almost identical with the experimental results except the locations of shock waves.

Figure 4.1.1 shows the qualitative comparison of the numerical code used. For quantitative comparison time averaged pressure coefficient is considered and shown in figure 4.1.2.

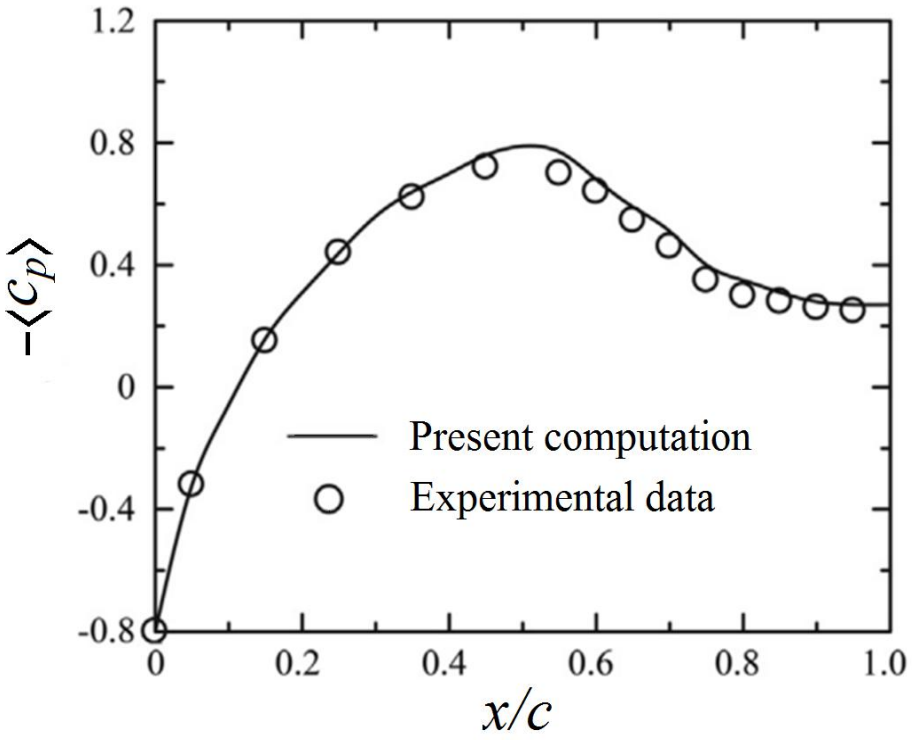

Fig 4.1.2: Distribution of time averaged pressure coefficient; Experimental data from [1]

In figure 4.1.2. The solid line represents the present computational results and open circle symbol represents experimental results of McDevitt et al. [1]. The figure shows that for most of the flowfield the computational results are almost same with the experimental data. The computational results slightly over predict the value of c_p in the mean shock position and the region of the intense shock boundary layer interaction.

The differences in shock structure and pressure coefficient are obviously due to the complexities in real flows, the mean flow non-uniformity and the sidewall boundary layer, which are never taken into account in present 2D numerical computation. In addition to the above discussion, the unsteady shock oscillation frequencies are taken into consideration for further validation. The present 2D computation predicts oscillation frequency which is 35% higher in magnitude compared to experimental data [12]. This means that there might be three dimensional mechanisms that govern the oscillation frequency. Similar observations were mentioned in the work of Xiong et al. [13].

4.2 FLOW FIELD CHARACTERISTICS

To analyze the flow, one complete cycle of oscillation is divided into equal 24 divisions for base airfoil and all the control cases. For brevity only 8 contours of schlieren images are shown. For base airfoil the flow field is shown as the sequential contour of schlieren image (figure 4.2.1), calculated by the first derivative of density in both x and y direction. The dark mark in the image represents the shock wave. The images clearly reveal the presence of normal shock wave over the airfoil and its oscillation with time. Considering the cycle starts when the upper shock is at its most distant location from the leading edge (LE), a cycle order is determined.

From the figure 4.2.1 it is observed that the shock wave is of normal type throughout the cycle for base airfoil. From the beginning of the cycle (t/T = 0) the shock wave on the upper surface starts to move toward the leading edge (LE) and gain strength. Then after a while it starts to become weaker but still maintain its forward movement. At about the end of the cycle the shock vanishes on the upper surface. The shock on the lower surface shows the same characteristics like upper surface shock except the shock is at the most distant location at time t/T = 0.5 and the cycle starts then. This type of shock oscillation is known as type B shock oscillation. This can be understand more clearly from the plot of shock location (x_s) against non dimensional time from figure 4.3.2(a) (detail is in section 4.3.1).

The corresponding flow field visualization for control cases OC_1, OC_2 and OC_3 are shown in figure 4.2.2, 4.2.3 and 4.2.4 respectively. From the figure of schlieren images of control cases it is clear that the flow field is greatly affected by the incorporation of open cavities. Both the shock structure and type of oscillation is changed for all control cases of open cavity. The oscillation become continuous and type A while there is also a transformation of normal and λ shock structure. For OC_1, OC_2 and OC_3 the shock is initially λ structured and then it turns into normal with further forward movement. The shock remain in λ shape for time duration of t/T = 0.21, 0.30 and 0.37 for cases OC_1, OC_2 and OC_3 respectively. As the λ shock wave has a larger foot than that of normal shock wave in base case its interaction with boundary layer is much weaker.

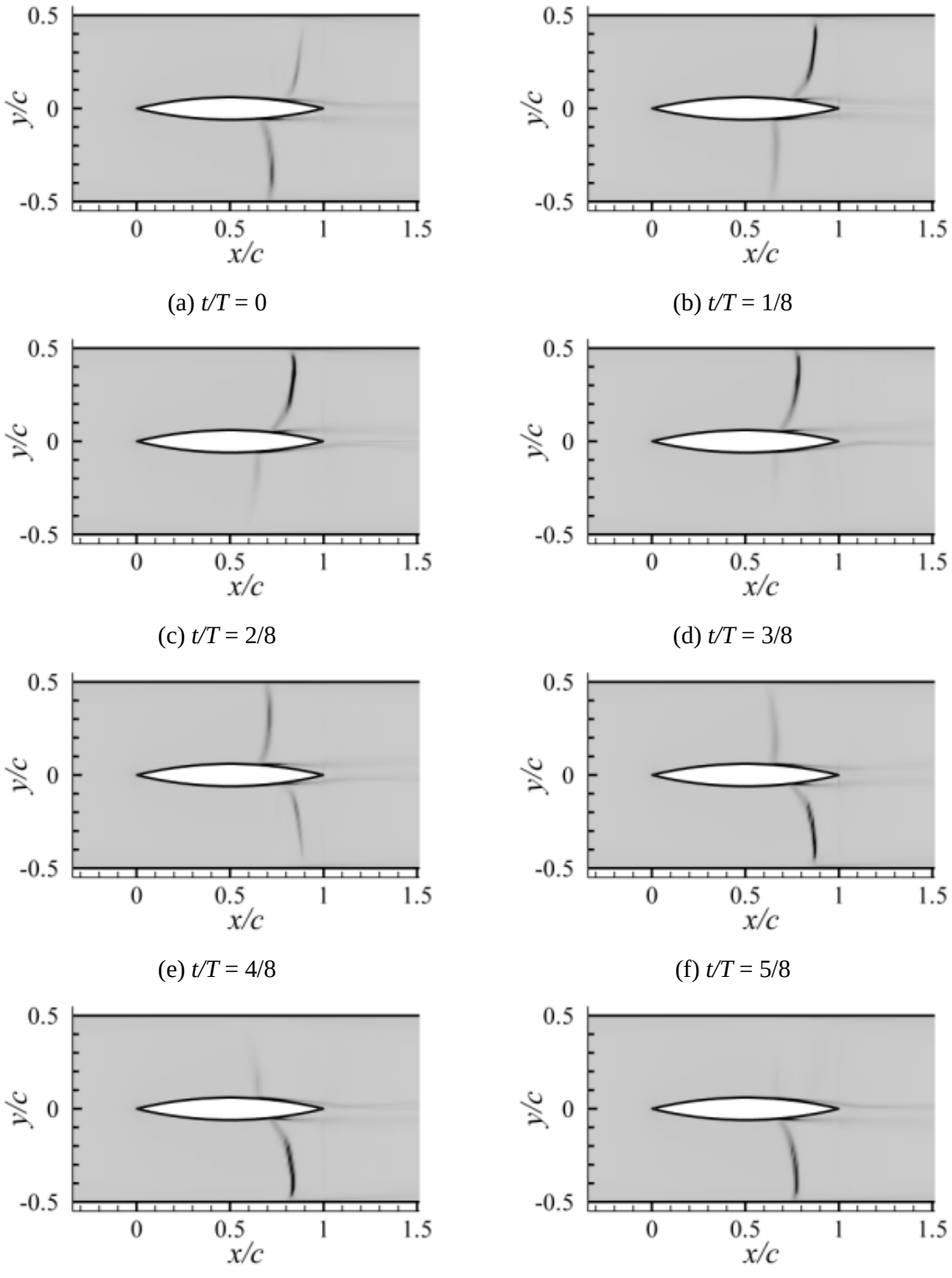

(a) $t/T = 0$ (b) $t/T = 1/8$

(c) $t/T = 2/8$ (d) $t/T = 3/8$

(e) $t/T = 4/8$ (f) $t/T = 5/8$

(f) $t/T = 6/8$ (h) $t/T = 7/8$

Fig 4.2.1: Flow field visualization (Schlieren image) for base airfoil

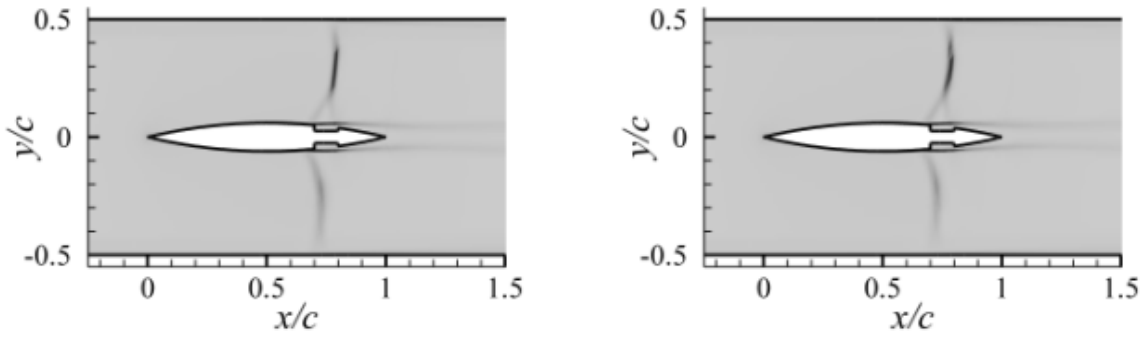

(a) $t/T = 0$ (b) $t/T = 1/8$

(c) $t/T = 2/8$ (d) $t/T = 3/8$

(e) $t/T = 4/8$ (f) $t/T = 5/8$

(f) $t/T = 6/8$ (h) $t/T = 7/8$

Fig 4.2.2: Flow field visualization (Schlieren image) for control case OC_1

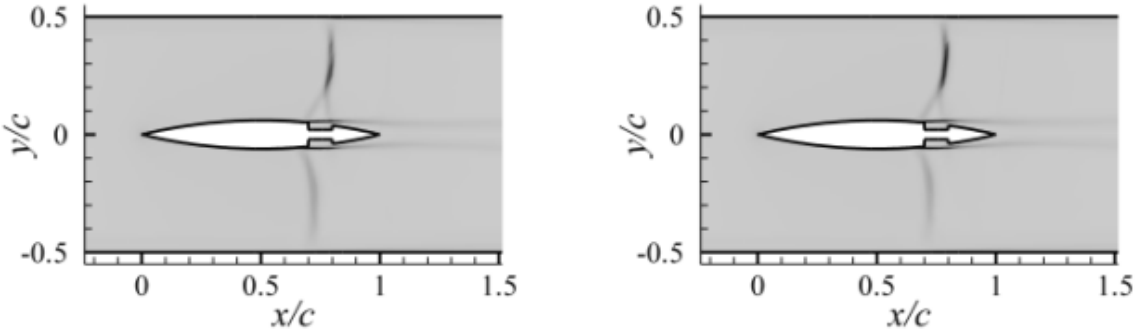

(a) t/T = 0 (b) t/T = 1/8

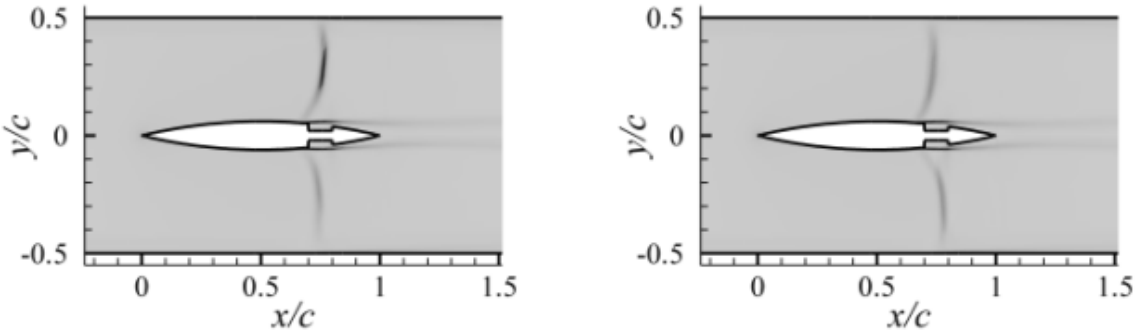

(c) t/T = 2/8 (d) t/T = 3/8

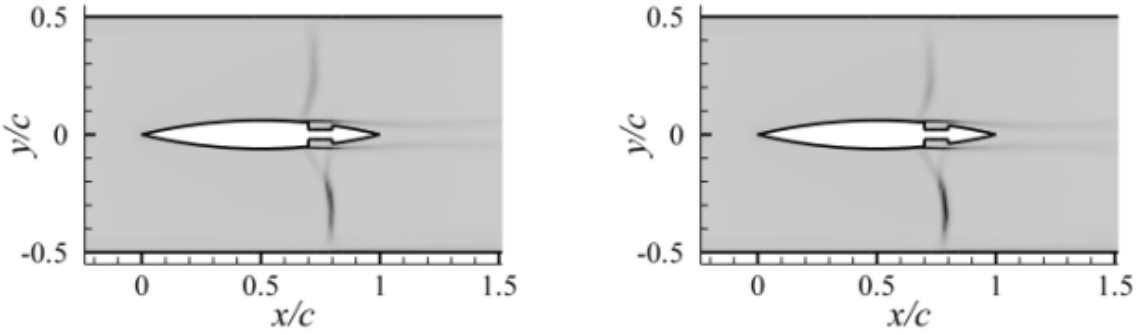

(e) t/T = 4/8 (f) t/T = 5/8

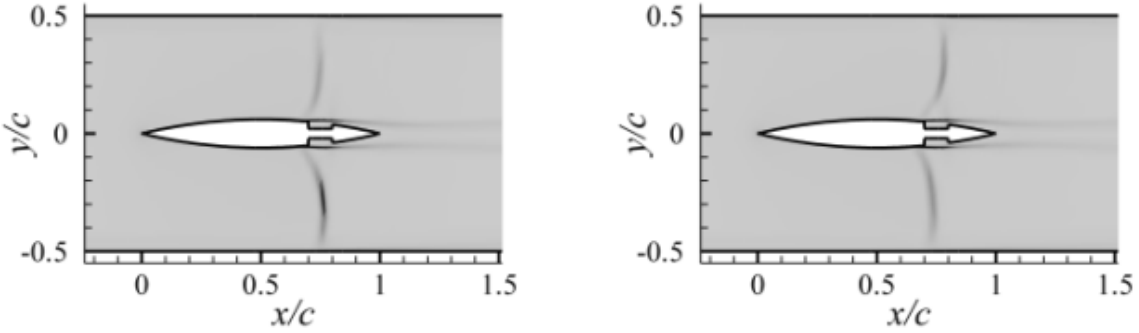

(f) t/T = 6/8 (h) t/T = 7/8

Fig 4.2.3: Flow field visualization (Schlieren image) for control case OC_2

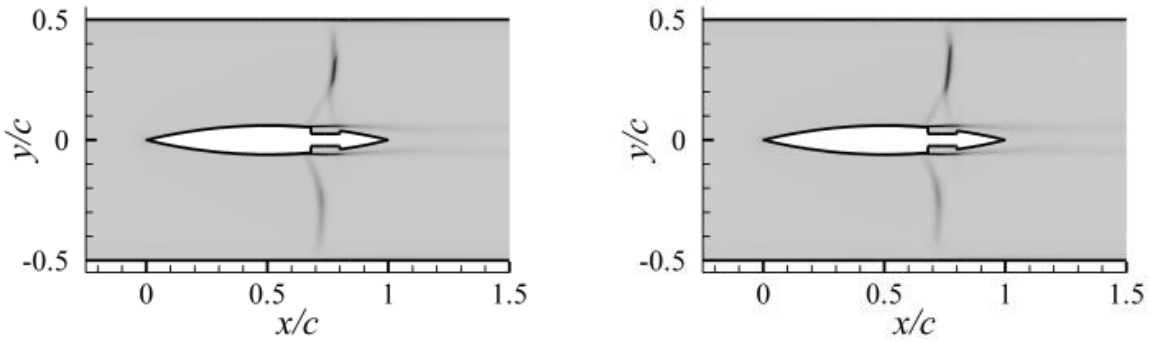

(a) $t/T = 0$ (b) $t/T = 1/8$

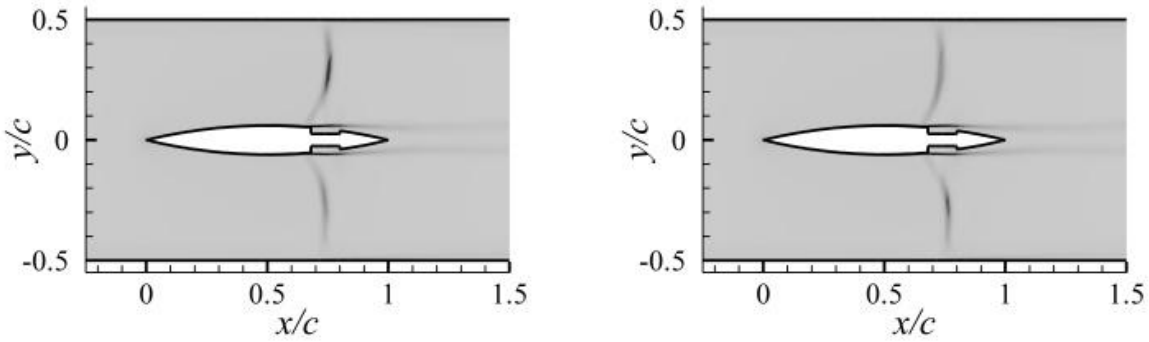

(c) $t/T = 2/8$ (d) $t/T = 3/8$

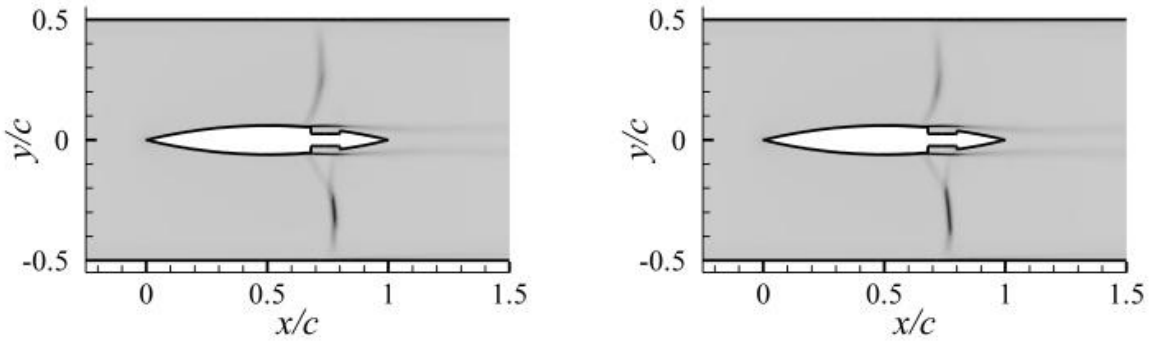

(e) $t/T = 4/8$ (f) $t/T = 5/8$

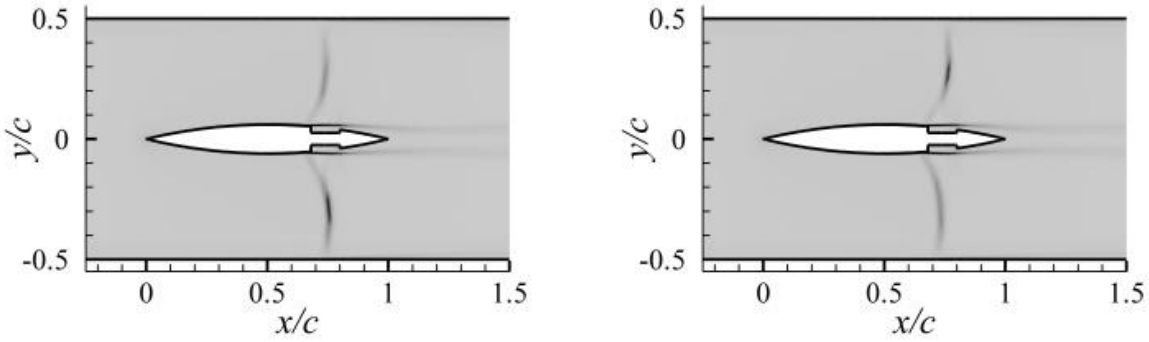

(f) $t/T = 6/8$ (h) $t/T = 7/8$

Fig 4.2.4: Flow field visualization (Schlieren image) for control case OC_3

4.3 SHOCK WAVE CHARACTERISTICS

The characteristics of the shock wave are studied by analyzing shock location (x_s/c), pressure rise across shock wave ($\Delta p/p_1$) and shock Mach number (M_s). These data are collected along two lines parallel to x axis (line 1 and line 2) passing through $y/c = \pm 0.1$ as shown in figure 4.3.1(a).

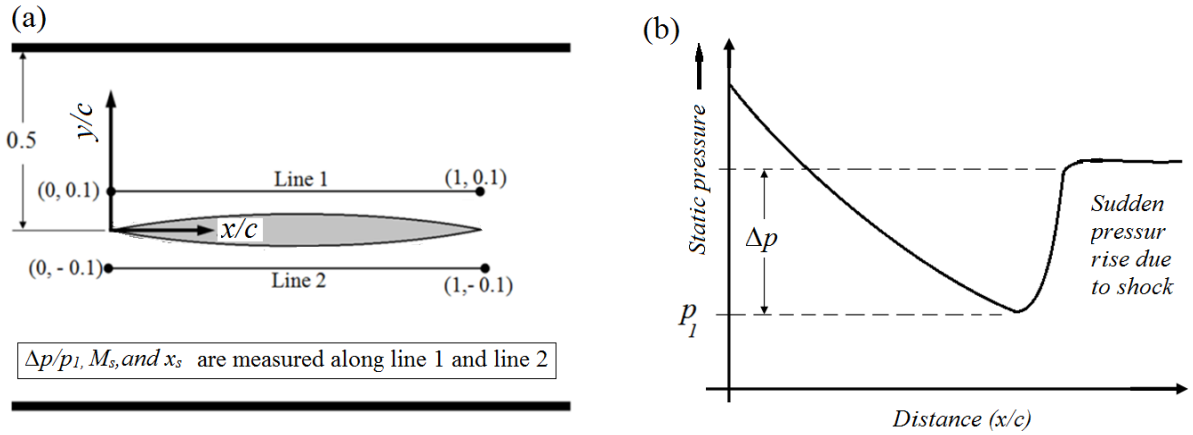

Fig 4.3.1: (a) Line for data collection and (b) Pressure rise across shock wave measurement

While calculating the shock location for λ shock, average location of two foots is considered as instantaneous shock location and plotted in figure 4.3.2. The pressure rise across shock wave ($\Delta p/p_1$) is measured by reading the minimum static pressure just ahead of the shock and the maximum sudden pressure rise across the shock as shown in the figure 4.3.1 (b). For λ shock sum of pressure rise in every steps is considered as total static pressure rise across shock wave.

4.3.1 SHOCK LOCATION

The unsteady shock location for base case, OC_1, OC_2 and OC_3 are shown in figure 4.3.2. For base case there is a very small time duration when shocks on both surfaces are present. Except that small fraction of time there is no shock on the lower surface while shock on the upper surface moves forward and vice versa.

This figure clearly reveals the type of shock oscillation as type B. Meanwhile for all the control cases with open cavity (OC_1, OC_2 and OC_3) the shock oscillation is continuous on both upper and lower surface, which is type A shock movement. So it is abundant that the incorporation of open cavity changes the type of shock oscillation.

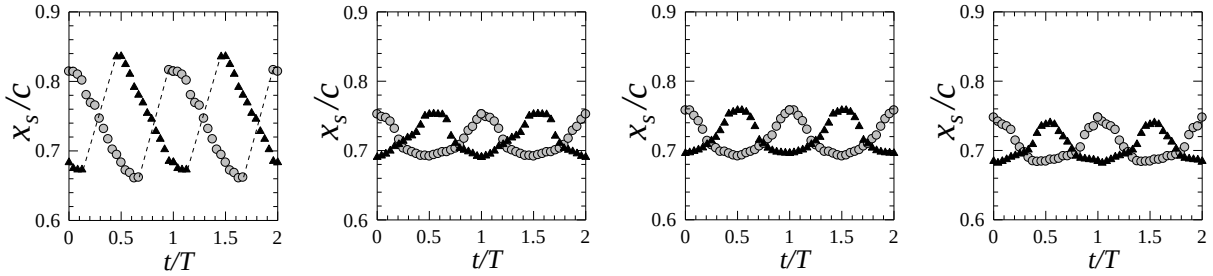

(a) Base Case (b) OC_1 (c) OC_2 (d) OC_3

Fig 4.3.2: Shock location with time. Line with circle and line with triangle represent shock location on line y/c = 0.1 and y/c = - 0.1 respectively

Another important finding of this figure is that due to open cavity the average shock location is moved toward the leading edge and the shock excursion zone is reduced significantly. The time averaged shock location for base case, OC_1, OC_2 and OC_3 are found to be x/c = 0.744, 0.716, 0.719 and 0.709. The excursion zone is reduced about 62.5%, 58.8% and 61.2% for cases OC_1, OC_2 and OC_3.

4.3.2 PRESSURE RISE ACROSS SHOCK WAVE

In the present study pressure rise across the shock is taken as the indicator of shock strength. The pressure rise across the shock along line x/c = 0.1 for all cases are plotted against time in figure 4.3.3. The figure clearly indicate the initial strength gain of the shock and then further reduction of shock strength with time for all the cases.

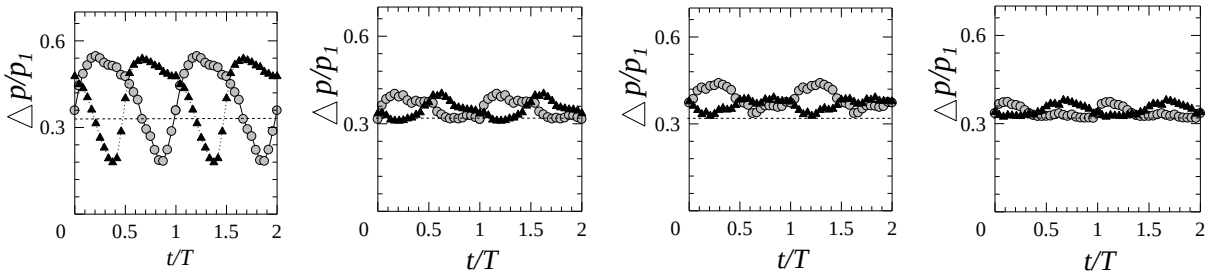

(a) Base Case (b) OC_1 (c) OC_2 (d) OC_3

Fig 4.3.3: Pressure rise across shock wave. Line with circle and line with triangle represent pressure rise across along line y/c = 0.1 and y/c = - 0.1 respectively.

With a close attention at figure 4.3.2(a) and 4.3.3(a) it can be noticed that for base case when the upper shock vanishes [t/T > 0.6, from figure 4.3.2 (a)] the value of $\Delta p/p_1$ for upper shock falls below 1/3. That means the shock wave become a compression wave when the total pressure rise ($\Delta p/p$) across it falls below 1/3. The same observation can be made for lower shock also. So for further analysis of all the control cases it is logical to consider $\Delta p/p_1$ = 1/3 as a threshold for shock to transform into a compression wave which is shown by a dotted line in the figure. This value is

obtained for a particular point on the shock ($y/c = \pm 0.1$) for present study which is transonic flow of air over a 12% thick circular arc airfoil at zero angle of incidence when upstream Mach number is 0.65. This threshold value can vary depending on the type of flow (internal/external), upstream Mach number, thickness of the airfoil, angle of incidence, operating conditions, position along shock length and properties of flowing fluid.

From figure 4.3.3 it can be concluded that the value of $\Delta p/p_1$ for control cases never falls below 1/3. So the shock oscillation for these cases are continuous and of type A. Which surely supports the conclusion from the flow field visualization in section 4.2 (figure 4.2.2, 4.2.3 and 4.2.4).

From the plot of $\Delta p/p_1$ (fig 4.3.3) and flow field visualizations it is found that for control cases the maximum shock strength is much lower than that of base case. This decrease in shock strength at the beginning of oscillation cycle is due to the incorporation of the open cavities. Again installation of open cavity increases the strength of the rearward moving compression wave. This could be possible by either of the following way:

i. The propagation of either pressure wave or upstream wave or may be both (further analysis is required) is interrupted so it supplies less energy during strength gaining period of the shock compared to the base case. This mechanism suggests that the shock is interacting weakly with upstream wave or the pressure wave is interacting weakly with the disturbances. Due to this weaker interaction the dissipation of energy is reduced during the time period when the shock is supposed to turns into compression wave. So the shock wave do not turn into compression wave and the oscillation become type A

ii. The propagation of either pressure wave or upstream wave or may be both (further analysis is required) is shifted with a time delay/advance in such a manner that the upstream wave provide energy to the shock when it already has turned into a compression wave. So the pressure waves do not provide any energy to the shock during its strongest period rather it provides energy during its weakest period and retard its transformation to compression wave.

iii. The above two could happen simultaneously which indicate that incorporation of open cavities can affect both the interaction and the phase of either pressure wave or the upstream wave or both.

4.3.3 SHOCK MACH NUMBER

The variation of shock Mach number, M_s (Mach number just ahead of the shock) along line $y/c = \pm 0.1$ is shown in figure 4.3.4. From the figure we can see a significant decrease in shock Mach fluctuation. For cases OC_1, OC_2 and OC_3 percent decrease in M_s fluctuation are found to be 78.3%, 73% and 85.2% respectively.

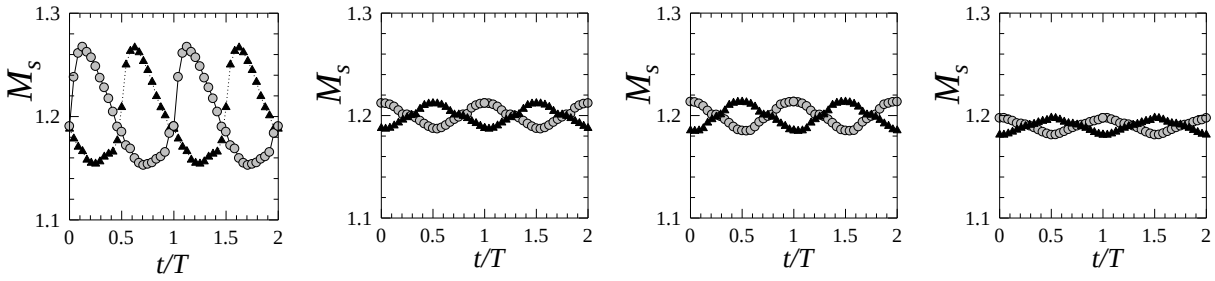

(a) Base Case (b) OC_1 (c) OC_2 (d) OC_3

Fig 4.3.4: shock Mach number. Line with circle and line with triangle represent shock Mach number on line $y/c = 0.1$ and $y/c = -0.1$ respectively

From the plot of M_s (fig 4.3.4) it can be said that for control cases the maximum shock Mach is much lower that of base case. Again there is a great difference between the base case and the open cavity cases at the beginning (t/T) of the cycle. The figure clearly reveals the phase difference between control cases shock Mach variation and base case shock Mach variation with time. For all the open cavity cases the shock Macs variation starts with a difference in shock mach for upper and lower shock wave. But for Base case the shock Mach for upper and lower shock wave is almost same at $t/T = 0$.

The phase difference in shock Mach at the beginning of oscillation cycle for open cavity installation supports the third mechanism most. So a possible and acceptable illustration of the mechanism might be as follows:

The propagation of either pressure wave or upstream wave or may be both (further analysis is required) could be interrupted and shifted with a time delay/advance in such a manner that the upstream wave provide less energy to the shock when the shock is supposed to gain strength. But it supplies energy to the shock wave when it is supposed to turn into a compression wave.

4.3.4 PRESSURE RISE ACROSS SHOCK WAVE ALONG SHOCK LENGTH

In section 4.3.2 the pressure rise across shock wave is taken on a particular point (y/c = 0.1) of the shock wave. To analyze the effect of open cavity on the shock strength the time averaged $\Delta p/p_1$ is calculated at eleven different points along the shock [figure 4.3.5(a)] length and is shown in figure 4.3.5(b). As for the base case the time averaged $\Delta p/p_1$ is maximum at y/c = 0.1, in earlier section (section 4.3.1, 4.3.2, 4.3.3) the fluctuation of $\Delta p/p_1$ is calculated along line passing through $|y/c|$ = 0.1.

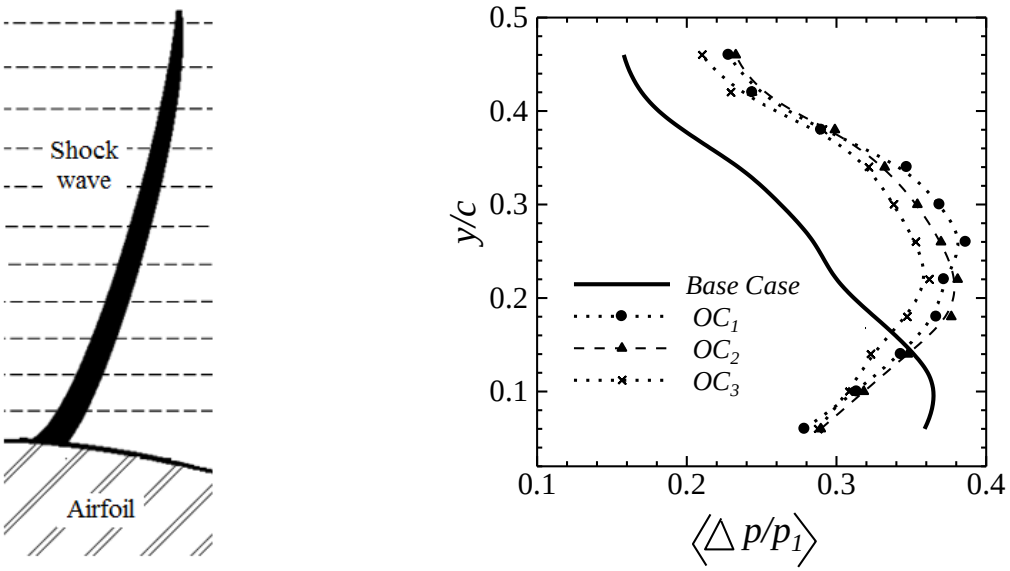

(a) (b)

Fig 4.3.5: (a) Lines for data collection; (b) Time averaged $\Delta p/p_1$ at different points along shock length

From the figure the overall view of shock control can be understood. The open cavities installed decrease the shock strength near the airfoil region (y/c ≤ 0.14) but increases the shock strength at far region (y/c > 0.14). The values of maximum time averaged $\Delta p/p_1$ are found to be 0.365, 0.386, 0.380 and 0.361 for base case, OC_1, OC_2 and OC_3 respectively. And the locations of maximum time averaged $\Delta p/p_1$ for base case, OC_1, OC_2 and OC_3 are found as y/c = 0.1, 0.26, 0.213 and 0.222. These reductions in shock strength near the airfoil region lower the pressure fluctuation on the airfoil surface (will be discussed in section 4.5). Meanwhile the increase in shock strength at far region can be a problem for real life applications especially where fluid flow through several airfoils situated side by side. The interaction of two strong shock waves between two consecutive airfoils may cause deterioration of overall performance of the Machinery. But for external flow over a single airfoil open cavity could be used for performance enhancement.

4.4 CONTROL MECHANISM

4.4.1 BOUNDARY LAYER THICKNESS

Figure 4.4.1 shows the velocity profile at trailing edge of the airfoil for eight different time steps for base case, OC_1, OC_2 and OC_3. To compare all the cases time averaged velocity is calculated from these unsteady data at 24 different time steps and shown in figure 4.4.2. From the time averaged velocity profile it is abundant that the thickness of the boundary layer at the trailing edge is reduced significantly after using the open cavities.

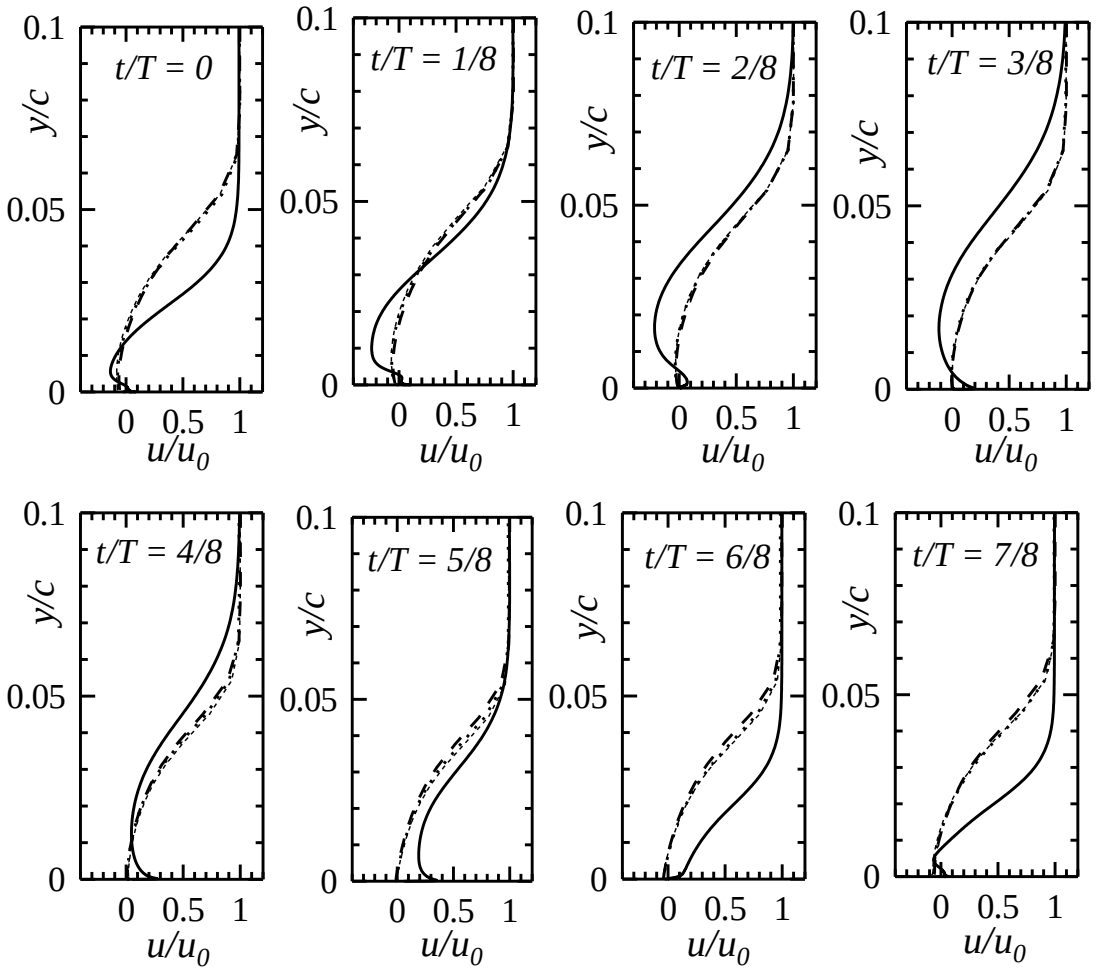

Fig 4.4.1: velocity profile at trailing edge for base case and open cavity cases. Solid line, dotted line, short dashed and dashed line represent base case, OC_1, OC_2 and OC_3

The time averaged boundary layer thickness is found as y/c = 0.092 for base case and 0.074 for cases OC_1, OC_2 and OC_3 which indicates about 20% reduction in boundary layer thickness. This decrease in boundary layer thickness could be due to the vortices created in the cavity which introduces a suction effect at the downstream of the shock wave.

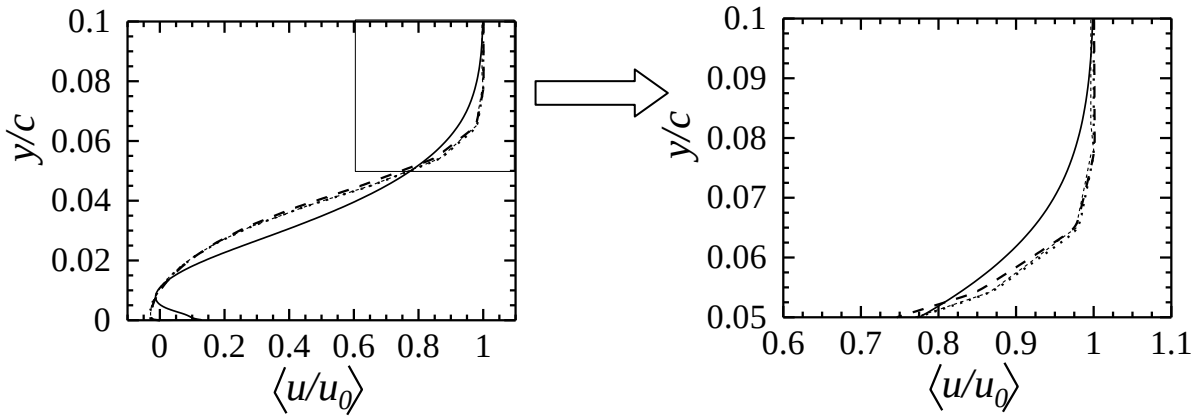

Fig 4.4.2: Time Averaged velocity profile at trailing edge for base case and open cavity cases. Solid line, dotted line, short dashed and dashed line represent base case, OC_1, OC_2 and OC_3

4.4.2 SHOCK BOUNDARY LAYER INTERACTION

Figure 4.4.3 shows the time variation of shock boundary layer interaction zone with time. The interaction zone was calculated as the chord wise distance between points of maximum Mach number and the point where Mach number is unity [as shown in figure 4.4.3(a)] and shown in figure 4.4.3(b).

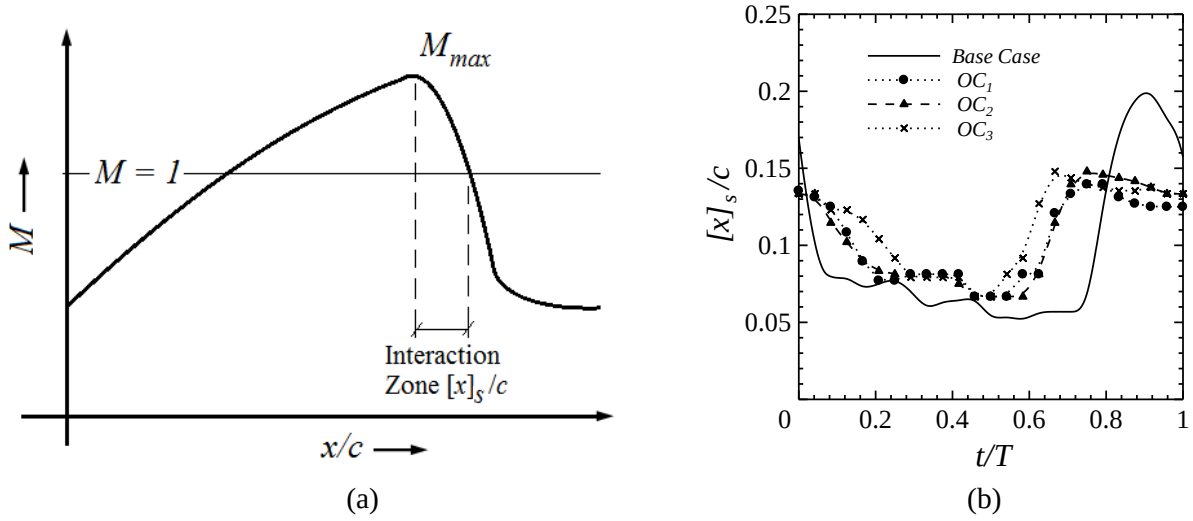

Fig 4.4.3: (a) Measurement procedure of shock boundary layer interaction zone; (b) Shock boundary layer interaction zone variation with time for open cavity cases

The figure reveals that the shock boundary layer interaction zone ($[x]_s/c$) for control cases OC_1, OC_2 and OC_3 is higher than the base case at any time instant. The time averaged value are of $[x]_s/c$ are 0.086, 0.104, 0.106 and 0.133 for base case, OC_1, OC_2 and OC_3. From section 5.1, the time duration in which shock move as λ shock for OC_1, OC_2 and OC_3 are found as t/T = 0.21, 0.3 and 0.37 respectively. So it can be concluded that for more time duration as a λ shock wave the shock boundary interaction zone is larger. This means that the gradient of fluid properties is reduced at the shock foot. This increase of $[x]_s/c$ for control cases enhances the communication between the upstream and downstream of the shock. This communication allows the reduction of pressure fluctuation on the airfoil surface (section 4.5).

4.5 PRESSURE FLUCTUATION ON AIRFOIL SURFACE

The unsteady pressure fluctuations over upper airfoil surface at different chord wise location are shown in figure 4.5.1. From these figure the oscillation frequency of the shock oscillation is calculated as 760 Hz for base case, OC_1 and OC_2. For case OC_3 the oscillation frequency is observe as 700 Hz indicating around 8% reduction in oscillation frequency. For all the cases frequency of shock oscillation is measured at point where pressure fluctuation is maximum.

The RMS of static pressure fluctuation on airfoil surface is given in figure 4.5.2. The RMS of pressure fluctuation is calculated by the following equation:

$$p_{rms} = \sqrt{\sum_{i=1}^{n} (p_i - \bar{p})^2 / n} \qquad \text{where,} \qquad \bar{p} = \sum_{i=1}^{n} p_i / n$$

Here p_i is the instantaneous static pressure; $\bar{p}$ is averaged pressure; n is number of data points

The figure shows a maximum pressure fluctuation of base case occurs at about x/c = 0.75. This is the reason the cavities are installed with mean position at x/c = 0.75. The maximum values of p_{rms}/q_0 are 0.377, 0.096, 0.109 and 0.073 meanwhile the location of maximum pressure fluctuation are x/c = 0.75, 0.68, 0.68 and 0.66 for base case, OC_1, OC_2 and OC_3 respectively.

From figure 4.5.1 and 4.5.2 it can be concluded that the open cavity can reduce the surface pressure fluctuation. So incorporation of open cavity could be used as an effective device to reduce noise and vibration in an external flow. But use of open cavity in case of internal flow needs further study (see section 4.3.4).

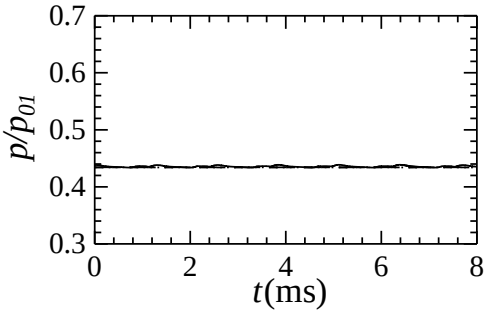

(a) *x/c* = 0.583

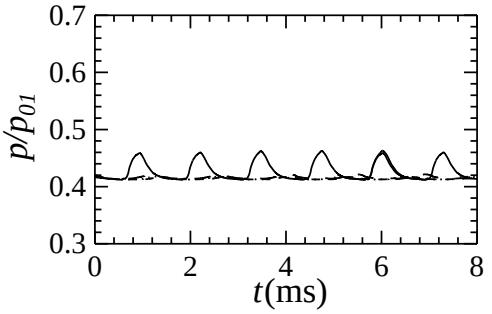

(b) *x/c* = 0.625

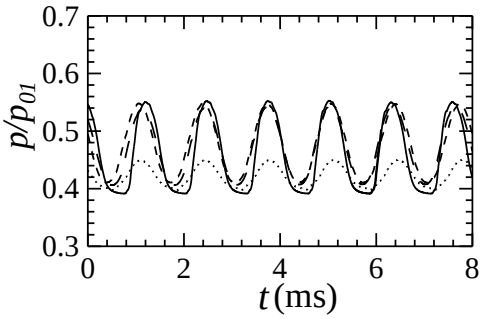

(c) *x/c* = 0.667

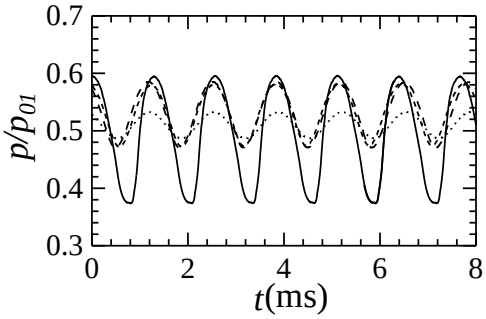

(d) *x/c* = 0.708

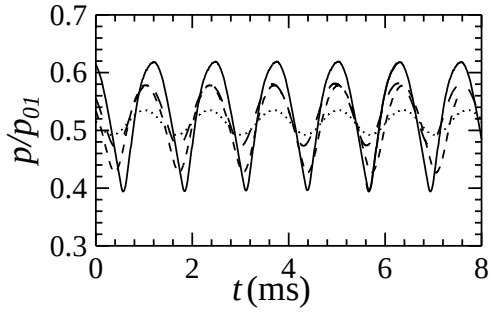

(e) *x/c* = 0.750

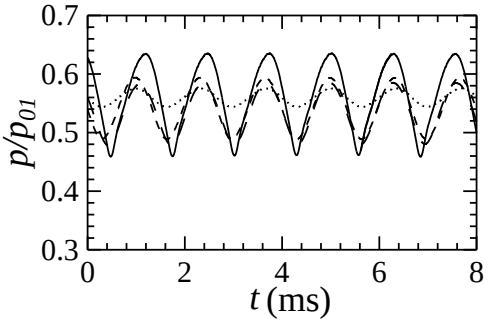

(f) *x/c* = 0.792

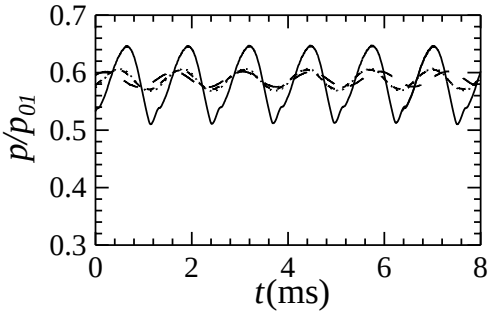

(g) *x/c* = 0.833

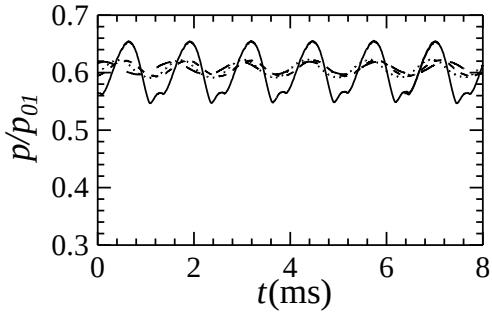

(h) *x/c* = 0.875

Fig 4.5.1: Pressure variation history with time at different location on upper airfoil surface for open cavity. Solid, dashed, dotted and long dashed line represents base case, OC_1, OC_2 and OC_3

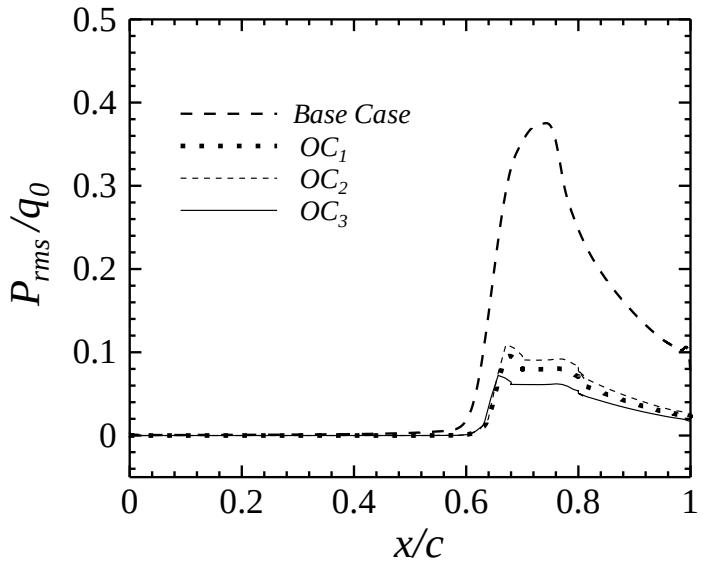

Fig 4.5.2: RMS pressure fluctuation over upper airfoil surface for open cavity cases

The shock oscillation frequency is reduced only for control case OC_3, this could mean that the length of the cavity is one of the major factors that affects the shock oscillation frequency. Further study could be carried out by calculating the speed of the pressure wave and the upstream wave to analyze the effect of open cavities on shock oscillation frequency.

4.6 TOTAL PRESSURE LOSS

As the open cavities can reduce the shock strength over the airfoil surface but increase the shock strength at the far region, there arises a question about the economic feasibility. To assess the economic feasibility total pressure loss is considered and studied at the airfoil trailing edge. The time averaged total pressure loss is calculated as a percentage of upstream total pressure (p_{01}). Figure 4.6.1 shows the time averaged total pressure loss along the line parallel to *y*-axis passing through $x/c = 1$.

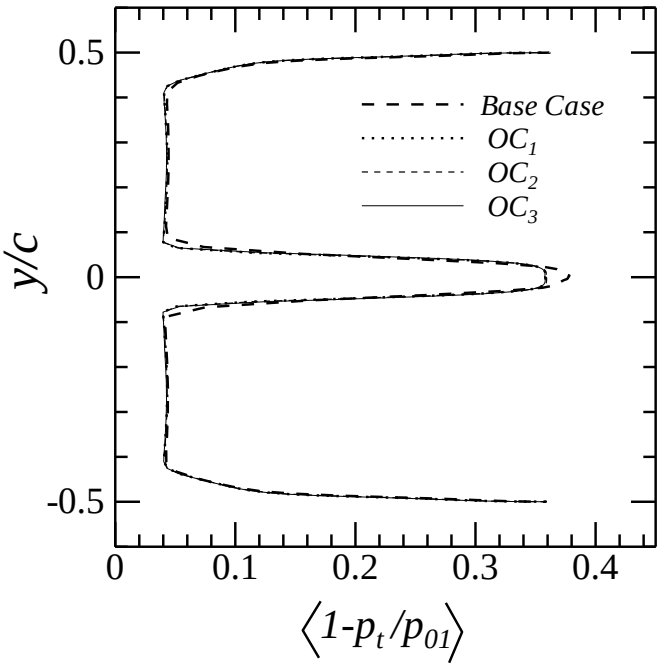

Fig 4.6.1: Time averaged total pressure loss for open cavity cases at trailing edge

The figure shows that the total pressure loss for the control cases is significantly reduced for the near regional flow field ($|y/c| \leq 0.1$). At $y/c = 0$ the time average total pressure loss is calculated as 0.379 for base case and 0.359 for OC_1, OC_2 and OC_3. For $|y/c| > 0.1$ the total pressure loss is almost same as the base airfoil, this could be the effect of increasing shock strength in the far region of the airfoil (section 4.3.4).

For further assessment of the open cavities the integrated total pressure loss (*ITPL*) is calculated as a percentage of upstream total pressure (p_{01}) at the trailing edge of the airfoil. The total pressure loss is calculated using the following equation:

$$ITPL = 100 \times \int_{-c/2}^{c/2} \left[1 - \frac{p_t}{p_{01}}\right] d(y) \quad \%$$

Here, p_t is the total local pressure; p_{01} is the total inlet pressure.

The values of *ITPL* (in percentage) are 8.60, 8.27, 8.28 and 8.27 for base case, OC_1, OC_2 and OC_3 respectively. This decrease in pressure loss could lead toward the enhancement of performance of turbo-machineries where high speed external flow occurs over a curved surface.

CHAPTER 5

CONTROL WITH PERFORATED CAVITY

As open cavity installation in real internal flows is questionable, the configuration of the cavity need further modification for being used in machineries like compressors and turbines. The present study provides a solution to this problem by using perforated cavity. Total of nine perforated cavity with 3 different configurations and each configuration with 3 different percentage of perforation has been studied in the present study. The results obtained for perforated cavity is compared with the base case in two ways.

- **To find out the effect of cavity configuration**: Here the results are compared with the base case for fixed percentage of perforation while the cavity configuration is changed. i.e. results of control case $PC_{30\% - 1}$, $PC_{30\% - 2}$ and $PC_{30\% - 3}$ are compared with results of base case. To find out the effect of the percentage perforation of the cavity the results are represented configuration wise and compared with the base case. For that purpose configuration of perforated cavities have been divided into three categories and are designated as follows:

Configuration 1: Two identical openings at the ends of the cavity	Configuration 2: Two openings located symmetrically but none is at the ends of the cavity	Configuration 3: Three openings with one at middle and two at the ends of the cavity
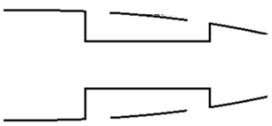	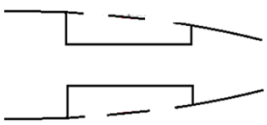	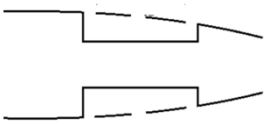
30%, 50% and 70% ($PC_{30\% - 1}$, $PC_{50\% - 1}$ $PC_{70\% - 1}$)	30%, 50% and 70% ($PC_{30\% - 2}$, $PC_{50\% - 2}$, $PC_{70\% - 2}$)	30%, 50% and 70% ($PC_{30\% - 3}$, $PC_{50\% - 3}$, $PC_{70\% - 3}$)

- **To find out the effect of percentage of perforation**: Here the results are compared with the base case for identical configuration of perforated cavity while varying their percentage of perforation. i.e. results of control case $PC_{30\% - 1}$, $PC_{50\% - 1}$ and $PC_{70\% - 1}$ are compared with results of base case.

5.1 EFFECT OF CAVITY CONFIGURATION

5.1.1 FLOW FIELD CHARACTERISTICS

5.1.1.1 Control cases $PC_{30\%-1}$, $PC_{30\%-2}$ and $PC_{30\%-3}$

The Schlieren image for control cases $PC_{30\%-1}$, $PC_{30\%-2}$ and $PC_{30\%-3}$ are shown in figures 5.1.1, 5.1.2 and 5.1.3 respectively. These figures provide some primary information about the shock structure and type of shock oscillation. For cases $PC_{30\%-1}$ it is seen that there is a weak normal shock wave on the upper surface at the beginning of the cycle (from figure 5.1.1). After some time, the shock become λ structured, then again it becomes normal type and finally vanishes at the end of the cycle. The shock on the lower surface follows the same life pattern except that its cycle starts at time t/T = 0.5. For case $PC_{30\%-2}$ and $PC_{30\%-3}$ the initial structure of the shock is λ and it become normal after some time and turn into a compression wave. The time duration for which the shock is in λ structure are found as t/T = 0.152, 0.213 and 0.251 for cases $PC_{30\%-1}$, $PC_{30\%-2}$ and $PC_{30\%-3}$ respectively.

For 30% perforated cavity the last two cases ($PC_{30\%-2}$ and $PC_{30\%-3}$) are different from the first case ($PC_{30\%-1}$,) in term of the initial (t/T = 0) structure of the shock wave. For last two cases the shock is initially λ structured while for first case the shock is initially normal. For all the cases of 30% perforated cavity the shock oscillation is of Tijdeman type B.

5.1.1.2 Control cases $PC_{50\%-1}$, $PC_{50\%-2}$ and $PC_{50\%-3}$

The flow field for control cases $PC_{50\%-1}$, $PC_{50\%-2}$ and $PC_{50\%-3}$ are shown in figures 5.1.4, 5.1.5 and 5.1.6 respectively. The figures reveal that for case $PC_{50\%-1}$ and $PC_{50\%-3}$ the type of shock oscillation is Tijdeman B while for control case $PC_{50\%-2}$ the oscillation is of type A. For control case $PC_{50\%-1}$ $PC_{50\%-2}$ and $PC_{50\%-3}$ the shock on upper surface is initially λ structured and remain in this structure for time period t/T = 0.24, 0.23 and 0.29. Then the shock become normal and then turns into compression wave with further forward movement.

The Schlieren images show that the shock is in λ structure during the time when shock is stronger. This eventually reduce the property (pressure, velocity density etc) gradients across the shock foot. Again it can be observe that the compression wave in control cases are stronger than that in base case. For case $PC_{50\%-2}$ a complete different scenario is observed. The shock wave on both upper and lower surfaces are stronger throughout the entire shock length compared to cases $PC_{50\%-1}$ and $PC_{50\%-3}$. Again as the shock oscillation is continuous with time it could be suggested that the configuration of the perforation has a prime role in determining the flow characteristics. For this case the shock appears to have smaller shock foot and more uniform strength compared to other to control cases of 50% perforation.

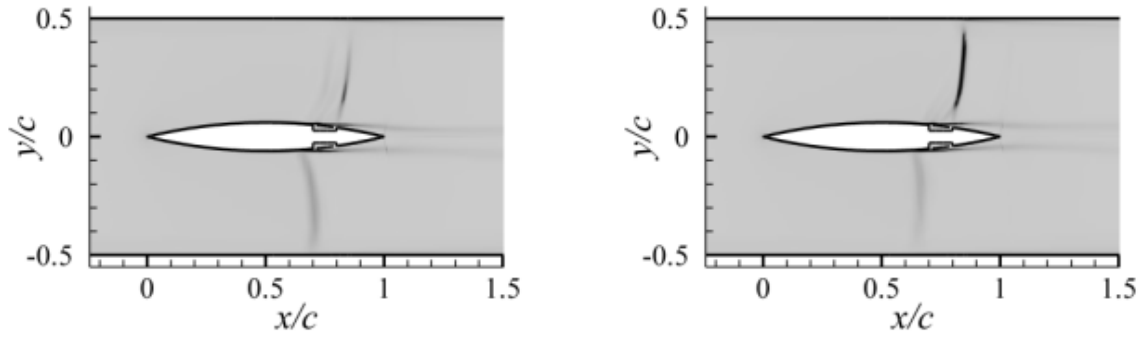

(a) t/T = 0 (b) t/T = 1/8

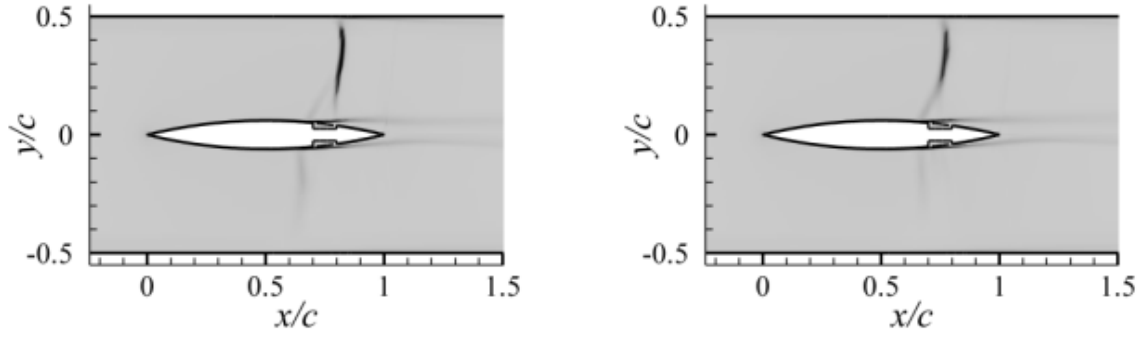

(c) t/T = 2/8 (d) t/T = 3/8

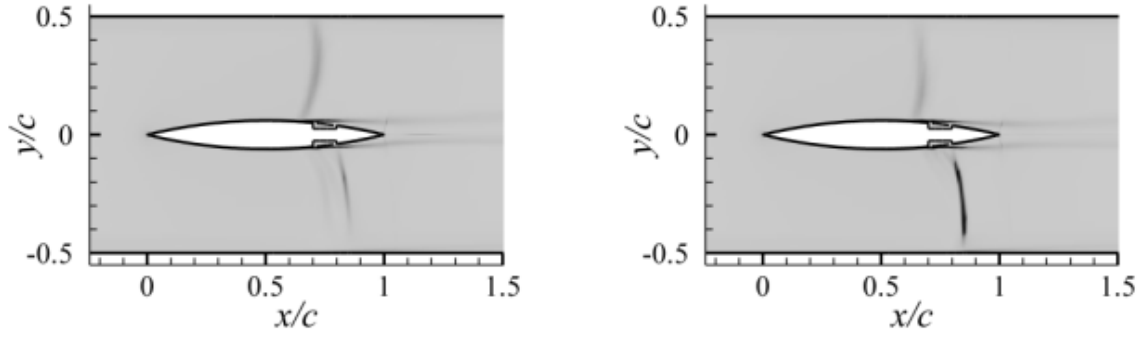

(e) t/T = 4/8 (f) t/T = 5/8

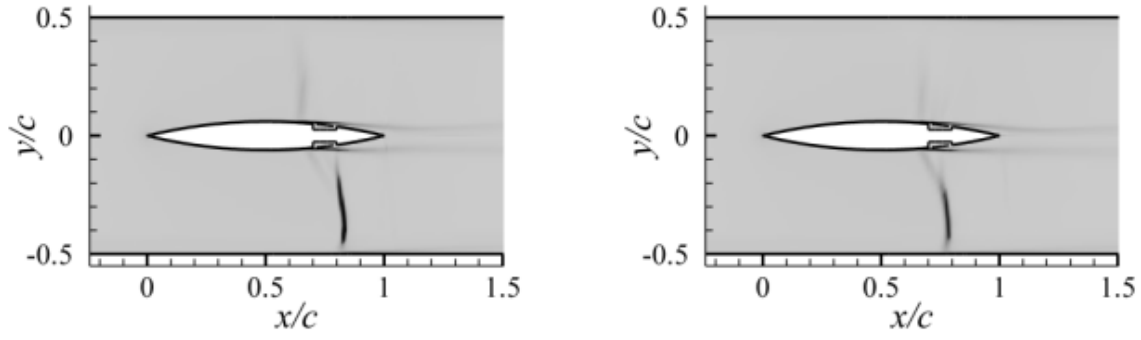

(f) t/T = 6/8 (h) t/T = 7/8

Fig 5.1.1: Flow field visualization (Schlieren image) for control case $PC_{30\%-1}$

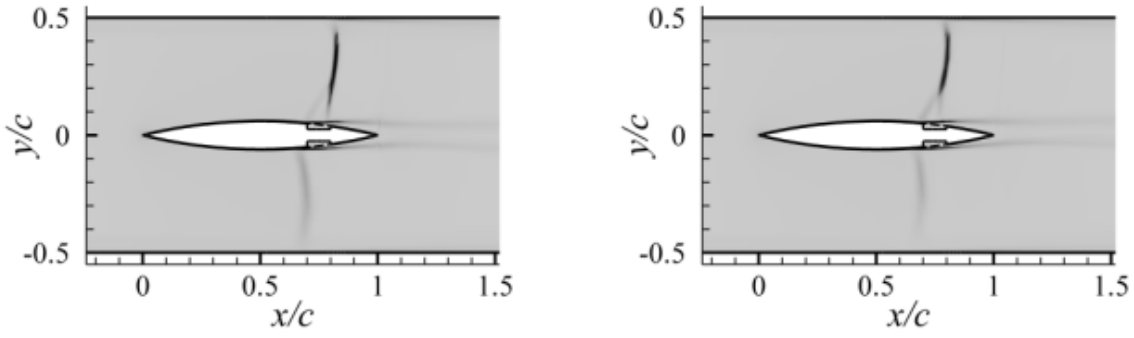

(a) t/T = 0 (b) t/T = 1/8

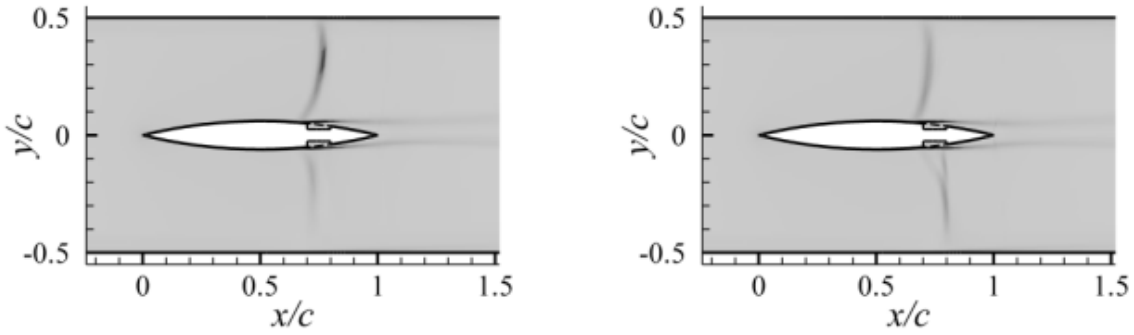

(c) t/T = 2/8 (d) t/T = 3/8

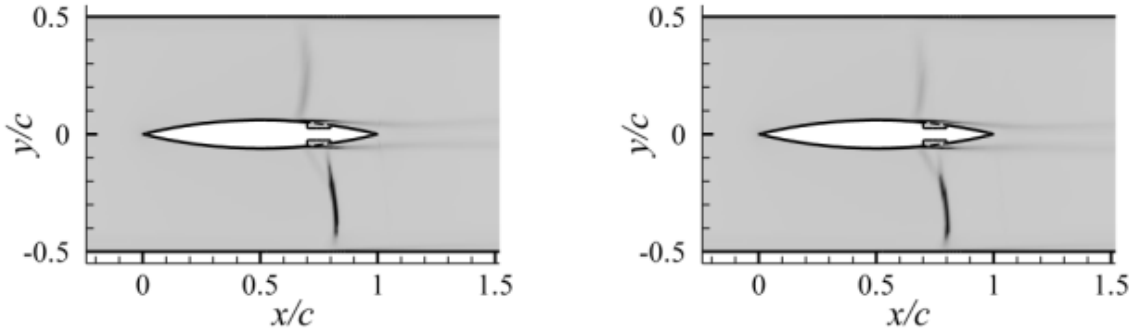

(e) t/T = 4/8 (f) t/T = 5/8

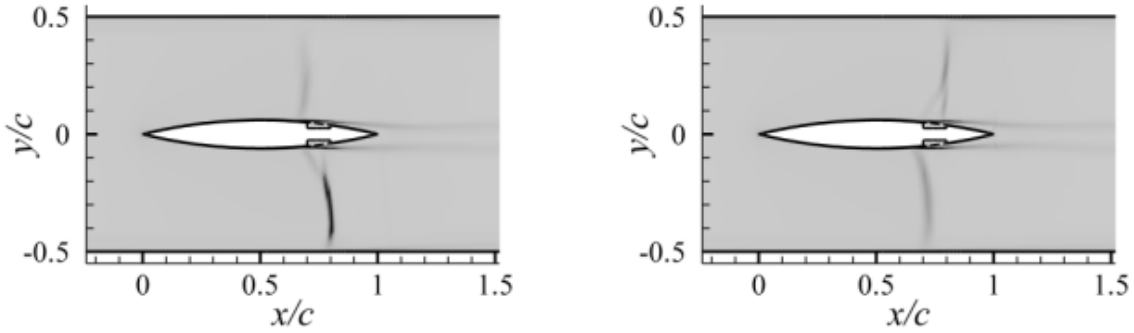

(f) t/T = 6/8 (h) t/T = 7/8

Fig 5.1.2: Flow field visualization (Schlieren image) for control case $PC_{30\%-2}$

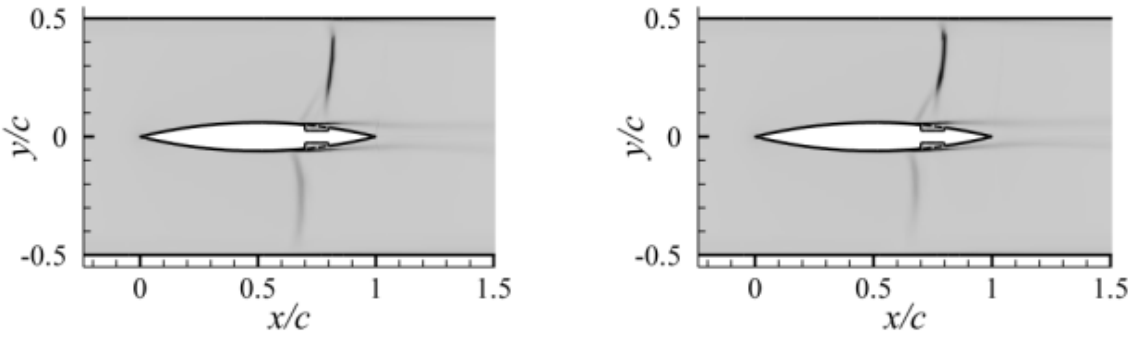

(a) t/T = 0 (b) t/T = 1/8

(c) t/T = 2/8 (d) t/T = 3/8

(e) t/T = 4/8 (f) t/T = 5/8

(f) t/T = 6/8 (h) t/T = 7/8

Fig 5.1.3: Flow field visualization (Schlieren image) for control case $PC_{30\%-3}$

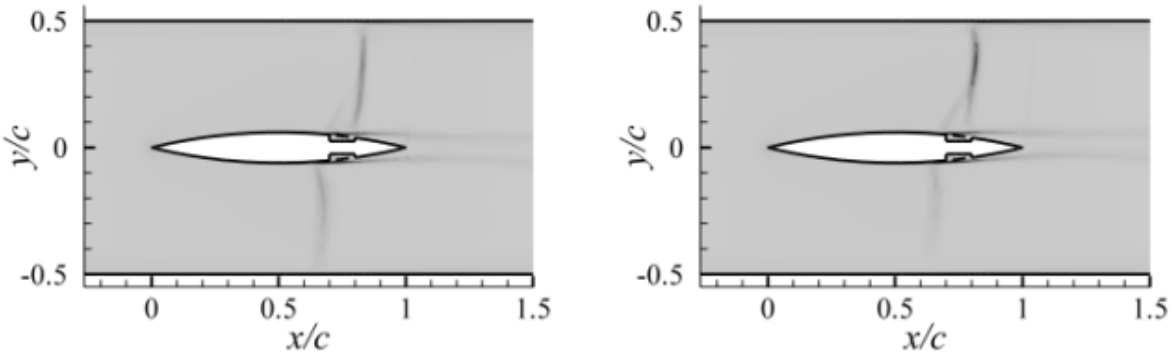

(a) t/T = 0 (b) t/T = 1/8

(c) t/T = 2/8 (d) t/T = 3/8

(e) t/T = 4/8 (f) t/T = 5/8

(f) t/T = 6/8 (h) t/T = 7/8

Fig 5.1.4: Flow field visualization (Schlieren image) for control case $PC_{50\%-1}$

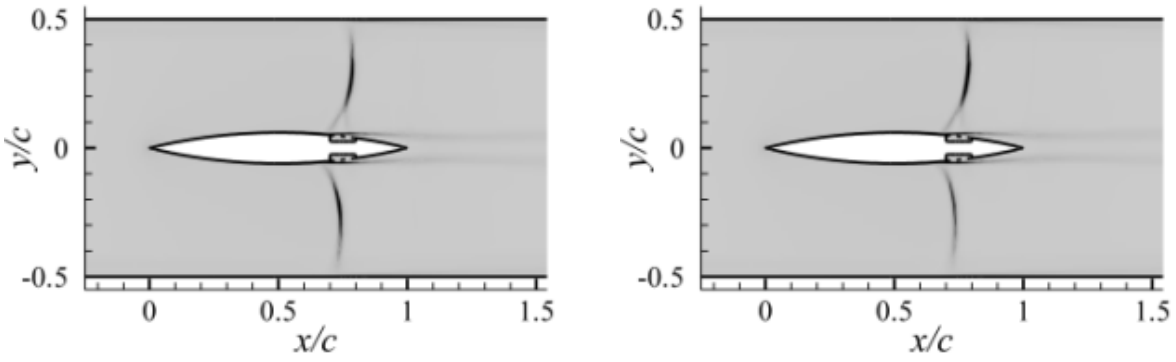

(a) t/T = 0 (b) t/T = 1/8

(c) t/T = 2/8 (d) t/T = 3/8

(e) t/T = 4/8 (f) t/T = 5/8

(f) t/T = 6/8 (h) t/T = 7/8

Fig 5.1.5: Flow field visualization (Schlieren image) for control case $PC_{50\%-2}$

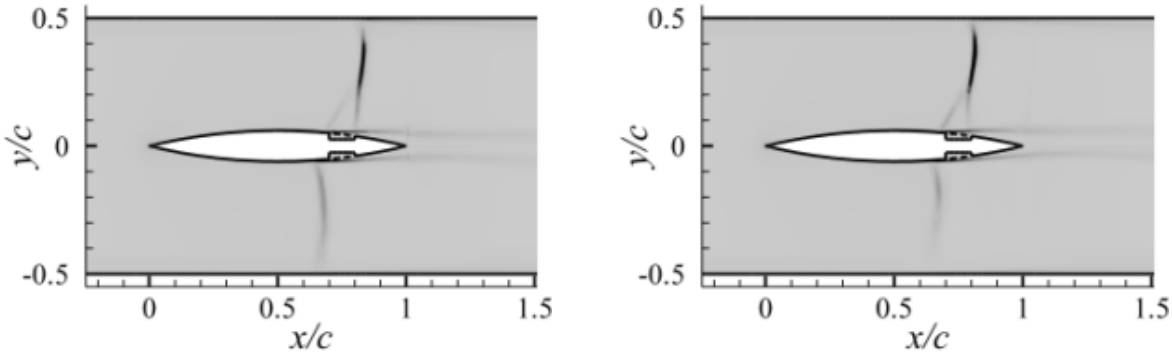

(a) t/T = 0 (b) t/T = 1/8

(c) t/T = 2/8 (d) t/T = 3/8

(e) t/T = 4/8 (f) t/T = 5/8

(f) t/T = 6/8 (h) t/T = 7/8

Fig 5.1.6: Flow field visualization (Schlieren image) for control case $PC_{50\%-3}$

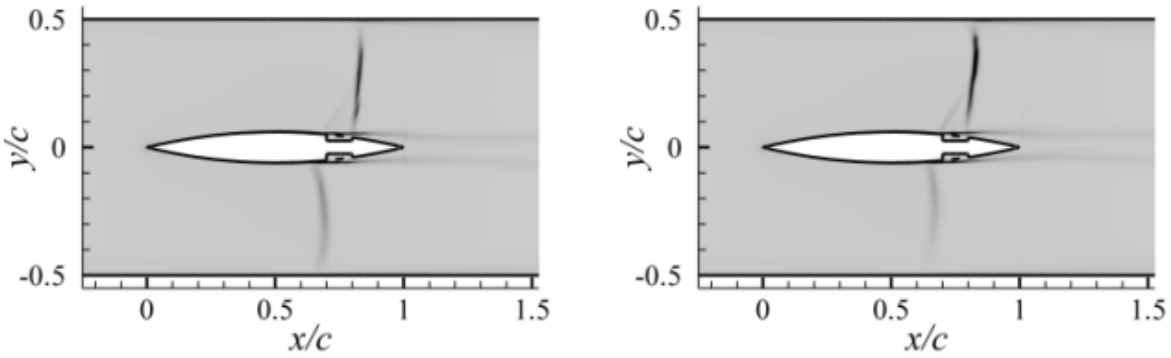

(a) t/T = 0 (b) t/T = 1/8

(c) t/T = 2/8 (d) t/T = 3/8

(e) t/T = 4/8 (f) t/T = 5/8

(f) t/T = 6/8 (h) t/T = 7/8

Fig 5.1.7: Flow field visualization (Schlieren image) for control case $PC_{70\%-1}$

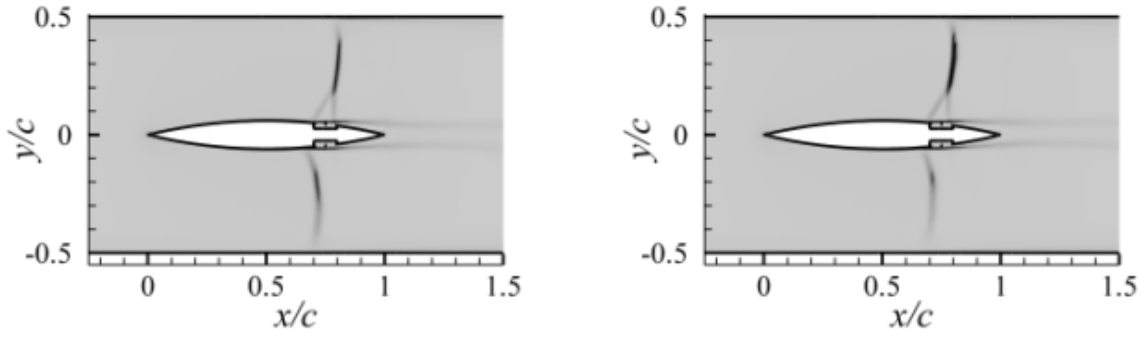

(a) $t/T = 0$ (b) $t/T = 1/8$

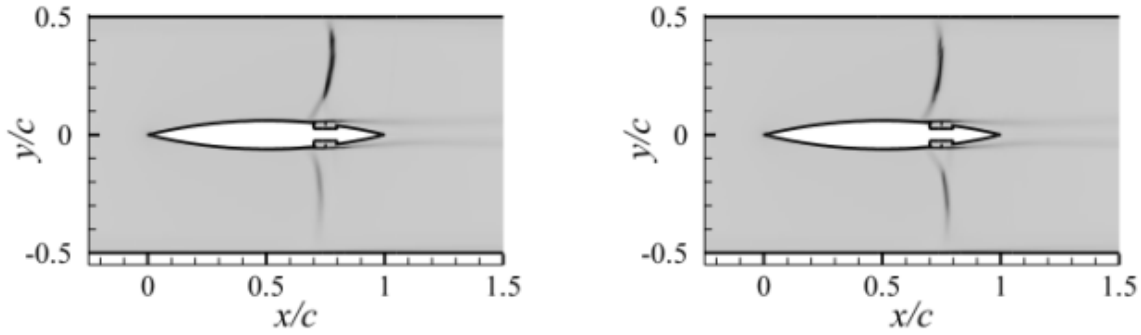

(c) $t/T = 2/8$ (d) $t/T = 3/8$

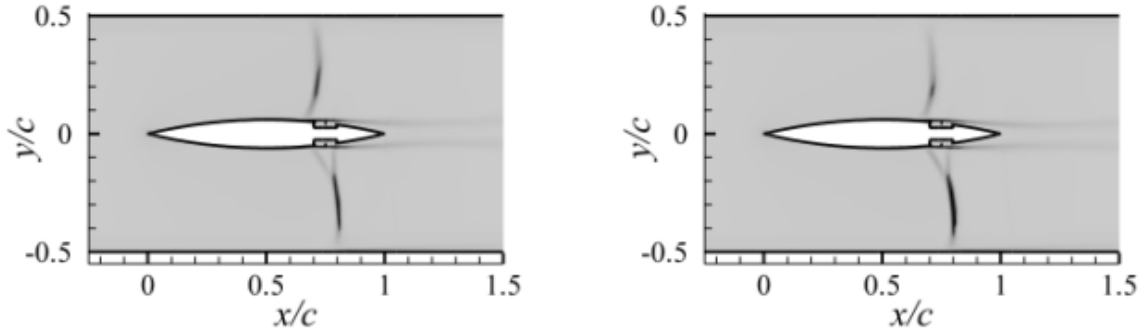

(e) $t/T = 4/8$ (f) $t/T = 5/8$

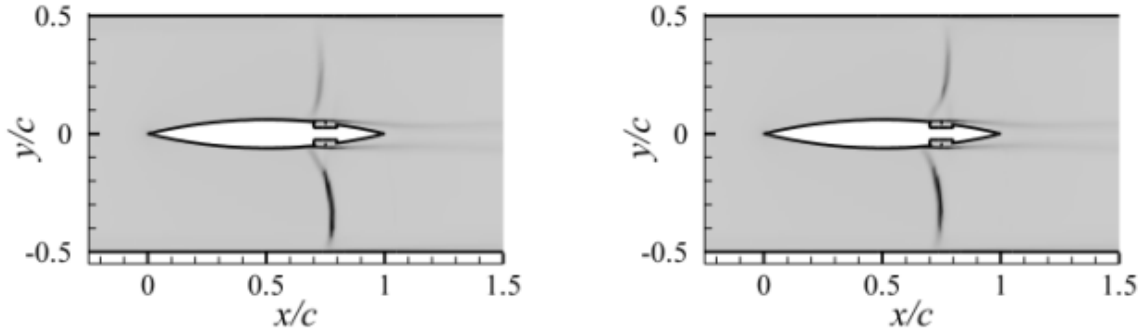

(f) $t/T = 6/8$ (h) $t/T = 7/8$

Fig 5.1.8: Flow field visualization (Schlieren image) for control case $PC_{70\%-2}$

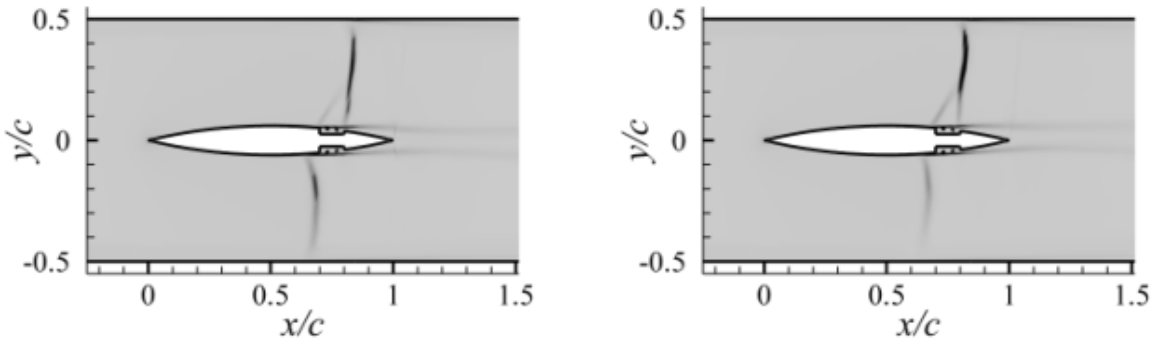

(a) t/T = 0 (b) t/T = 1/8

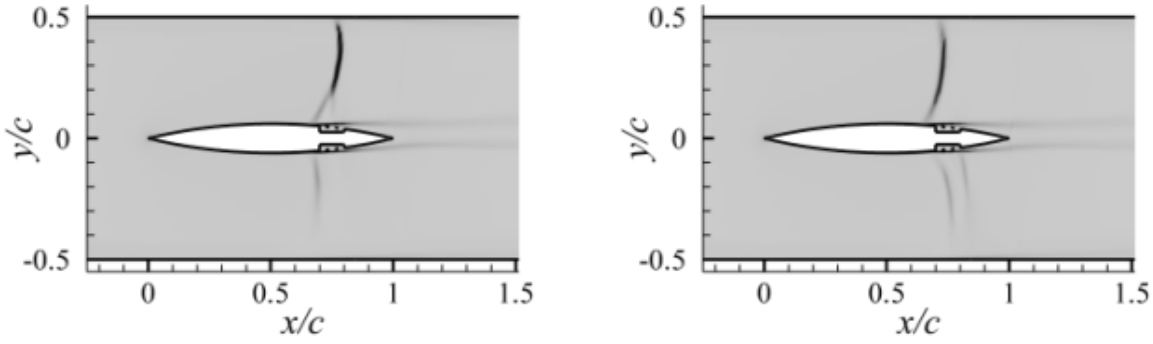

(c) t/T = 2/8 (d) t/T = 3/8

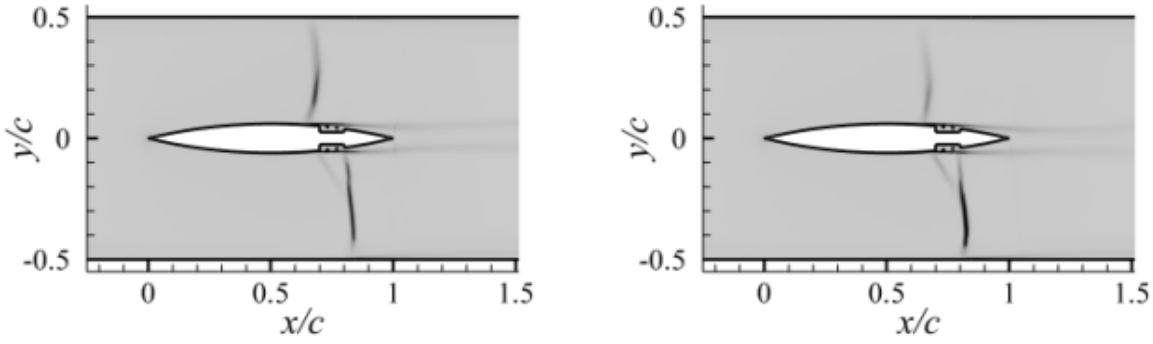

(e) t/T = 4/8 (f) t/T = 5/8

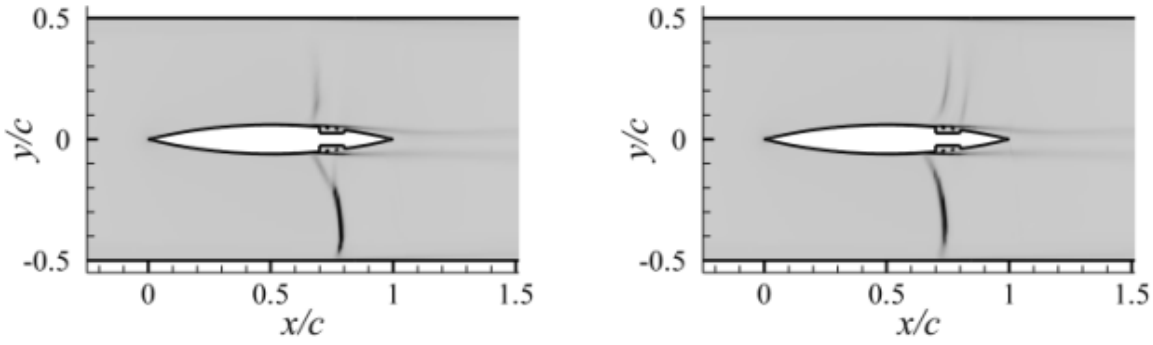

(f) t/T = 6/8 (h) t/T = 7/8

Fig 5.1.9: Flow field visualization (Schlieren image) for control case $PC_{70\%-3}$

5.1.1.3 Control cases $PC_{70\%-1}$, $PC_{70\%-2}$ and $PC_{70\%-3}$

The flow field for cases $PC_{70\%-1}$, $PC_{70\%-2}$ and $PC_{70\%-3}$ are shown as Schlieren images in figures 5.1.7, 5.1.8 and 5.1.9. The initial structure of the shock for these cases are λ shaped and it remains in that shape for time duration of t/T = 0.26, 0.33 and 0.30 for cases $PC_{70\%-1}$, $PC_{70\%-2}$ and $PC_{70\%-3}$ respectively. The flow field variation for cases $PC_{70\%-1}$ and $PC_{70\%-3}$ are similar to the cases $PC_{50\%-1}$ and $PC_{50\%-3}$ with a discontinuous shock oscillation except the foot length of the shock wave. Case $PC_{70\%-1}$ and $PC_{70\%-3}$ create larger shock foot compared to cases $PC_{50\%-1}$, $PC_{50\%-3}$ and cases $PC_{30\%-1}$, $PC_{30\%-3}$. This indicates that for configuration 1 and 3 (cases $PC_{30\%-1}$, $PC_{30\%-3}$, $PC_{50\%-1}$, $PC_{50\%-3}$, $PC_{70\%-1}$ and $PC_{70\%-3}$) larger shock foot can be attained with increasing percentage perforation.

A total different scenario is observed for case $PC_{70\%-2}$ also. The shock oscillation is of type A while for cases $PC_{70\%-1}$ and $PC_{70\%-3}$ it is of type B. Also for control case $PC_{70\%-2}$ the shock wave on both upper and lower surfaces are stronger throughout the entire shock length compared to cases $PC_{70\%-1}$ and $PC_{70\%-3}$. This again suggests that the configuration of the perforation has a prime role in determining the flow characteristics.

5.1.2 SHOCK WAVE CHARACTERISTICS

The characteristics of the shock wave are studied by analyzing shock location (x_s/c), pressure rise across shock wave ($\Delta p/p_1$) and shock Mach number (M_s). These data are collected along two lines parallel to x axis (line 1 and line 2) passing through $y/c = \pm 0.1$ as shown in figure 4.3.1(a).

5.1.2.1 Shock location

Shock location for control case with 30%, 50% and 70% perforation are shown in figure 5.1.10. For all the cases data are collected along lines shown in figure 5.2.1(a). From the shock location variation with time, the shock oscillation type for all perforated cases are easily conceivable. For all the cases the shock oscillations are discontinuous except case $PC_{50\%-2}$ and $PC_{70\%-2}$, where the oscillation appears to be continuous. Thess results are perfectly consistant with the Schlieren images discussed earlier.

For base case shock excursion zone is 0.16

Percentage of perforation	Configuration 1	Configuration 2	Configuration 3
30%	0.145	0.115	0.129
50%	0.134	0.044	0.150
70%	0.152	0.085	0.158

Table 5.1.1: Shock excursion zone for different control cases with perforated cavity.

Figure 5.1.10 reveals the effect of different configuration on the shock oscillation. From the figure the values of shock excursion zone found are presented in table 5.1.1 for easier representation of the results.

The results show that the shock excursion zone for perforated cavity cases depends on the configuration of the airfoil. For configuration 1 and 2 excursion zone decrease first with increase in percentage perforation and then increases. But for configuration 3 the excursion zone increases with increasing percentage perforation.

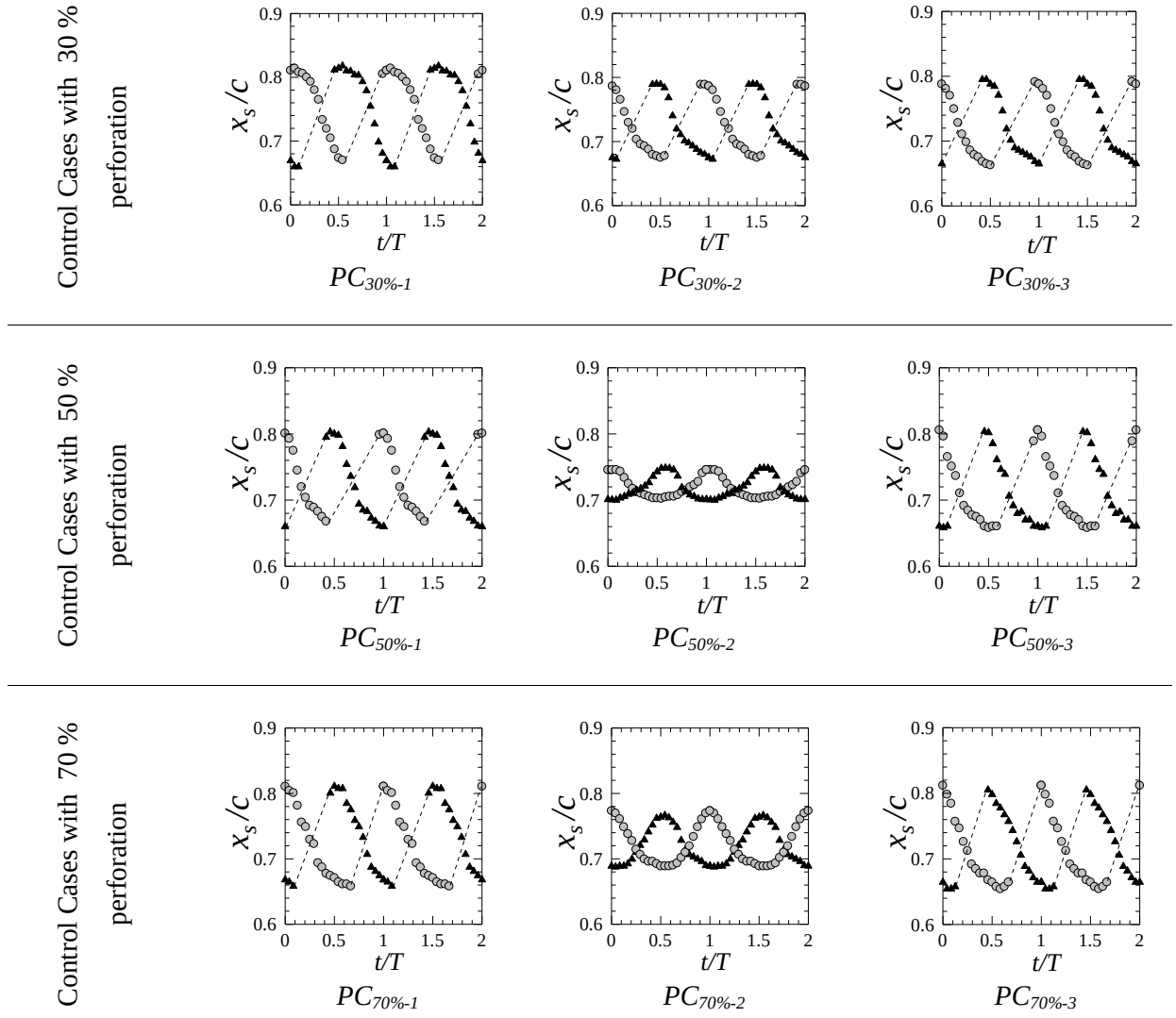

Fig 5.1.10: Shock wave location. Line with circle and line with triangle represent shock location on line y/c = 0.1 and y/c = - 0.1 respectively

5.1.2.2 Pressure rise across shock wave

Figure 5.1.11 shows the variation of $\Delta p/p_1$ with time for all control cases with perforated cavity. From figures 5.1.10 and 5.1.11 it is observed that the shock on both upper and lower surfaces turns into compression wave when $\Delta p/p_1$ falls below 1/3 for all nine cases. So our consideration of 1/3 as the threshold for transformation from shock wave to compression wave seems to have more logical consistency.

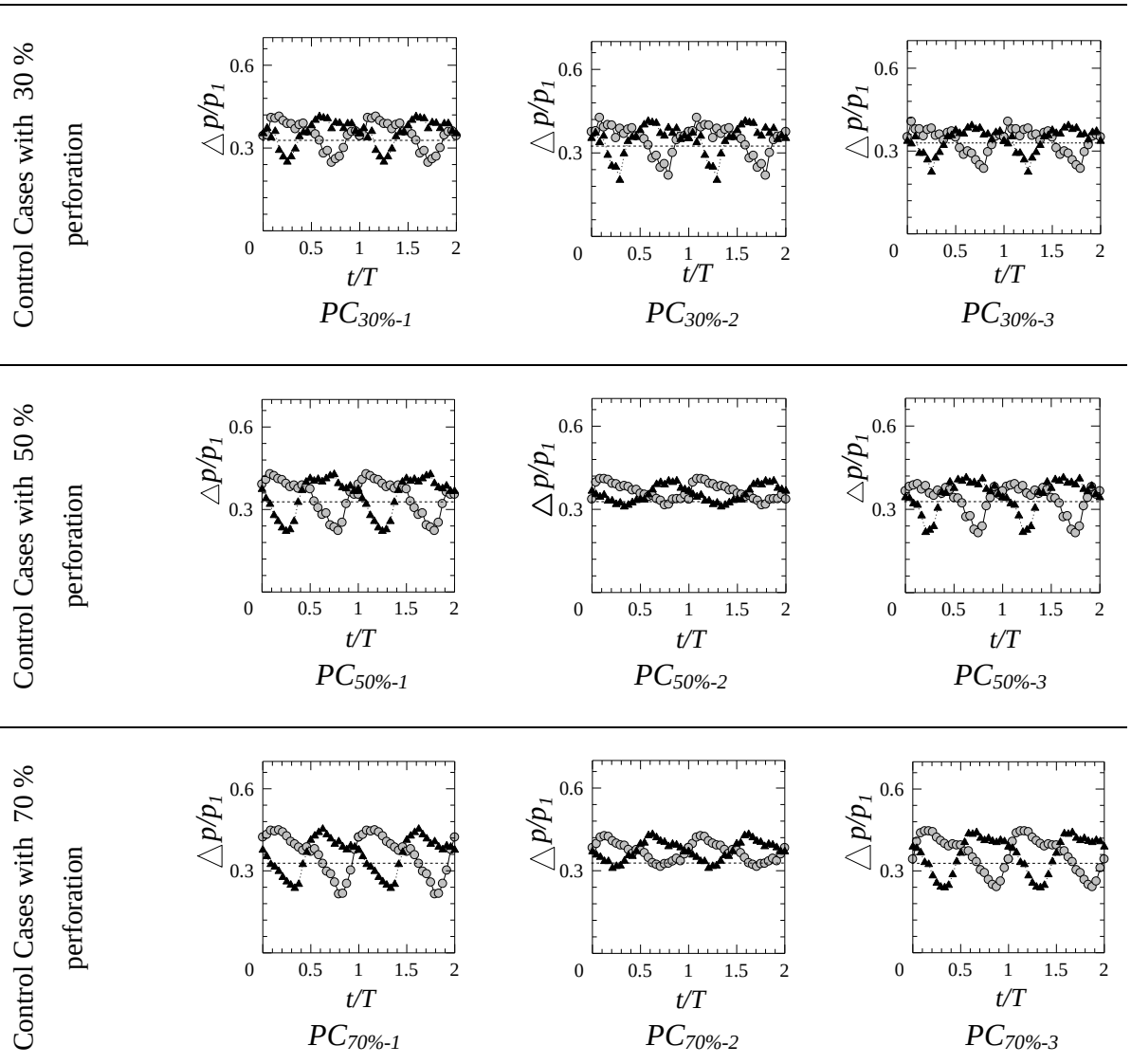

Fig 5.1.11: Pressure rise across shock wave. Line with circle and line with triangle represent pressure rise across along line y/c = 0.1 and y/c = - 0.1 respectively.

The Time averaged value of $\Delta p/p_1$ for all control cases with perforated cavity is shown in the table 5.1.2. From the table it is clear that all the control cases of perforated cavity lower the shock strength near airfoil region (will be discussed later). Again for all the configurations the shock strength near

the airfoil region increases slightly with increase of percentage perforation. The fluctuation in shock strength for all perforated cavity cases are also given in table 5.1.2. from the data in the table can be found that case $PC_{50\%-2}$ is the most effective in order to minimize the strength fluctuation. The same conclusion can be drawn from the table of shock excursion zone (table 5.1.1).

For base case time averaged $\Delta p/p_1$ is 0.403 and fluctuation of $\Delta p/p_1$ is 0.364

Percentage of perforation of control cases	Configuration 1		Configuration 2		Configuration 3	
	Time averaged $\Delta p/p_1$	Maximum fluctuation of $\Delta p/p_1$	*Time averaged* $\Delta p/p_1$	Maximum fluctuation of $\Delta p/p_1$	*Time averaged* $\Delta p/p_1$	Maximum fluctuation of $\Delta p/p_1$
30%	0.348	0.167	0.349	0.200	0.336	0.163
50%	0.349	0.210	0.362	0.099	0.338	0.175
70%	0.363	0.231	0.369	0.109	0.361	0.204

Table 5.1.2: Value of time averaged $\Delta p/p_1$ and its maximum fluctuation for different perforated control cases

From the plot of $\Delta p/p_1$(fig 5.1.11) and flow field visualizations it is found that for control cases the maximum shock strength is much lower that of base case. This decrease in shock strength at the beginning of oscillation cycle is due to the incorporation of the perforated cavity. Again installation of perforated cavity increases the strength of the rearward moving compression wave. This could be possible by either of the following way:

i. The propagation of either pressure wave or upstream wave or may be both (further analysis is required) is interrupted so it supplies less energy during strength gaining period of the shock compared to the base case. This mechanism suggests that the shock is interacting weakly with upstream wave or the pressure wave is interacting weakly with the disturbances. Due to this weaker interaction the dissipation of energy is reduced during the time period when the shock turns into compression wave. Of course, for perforated cavity this interaction is stronger than open cavity cases.

ii. The propagation of either pressure wave or upstream wave or may be both (further analysis is required) is shifted with a time delay/advance in such a manner that the upstream wave provide energy to the shock when is already has turned into a compression wave. So the pressure wave do not provide any energy to the shock during its strongest period rather it provides energy during its weak period.

iii. The above mentioned mechanism could happen simultaneously.

5.1.2.3 Shock Mach number

Figure 5.1.11 shows the variation of $\Delta p/p_1$ with time for all control cases with perforated cavity. The fluctuations of shock mach number are shown in table 5.1.3. The table illustrates that the fluctuation of shock Mach number is also lowest for case $PC_{50\%-2}$. That means shock excursion zone, fluctuation of shock strength and shock mach number are greatly affected by incorporation of perforated cavity and their variation patterns depends on the configuration of the cavity.

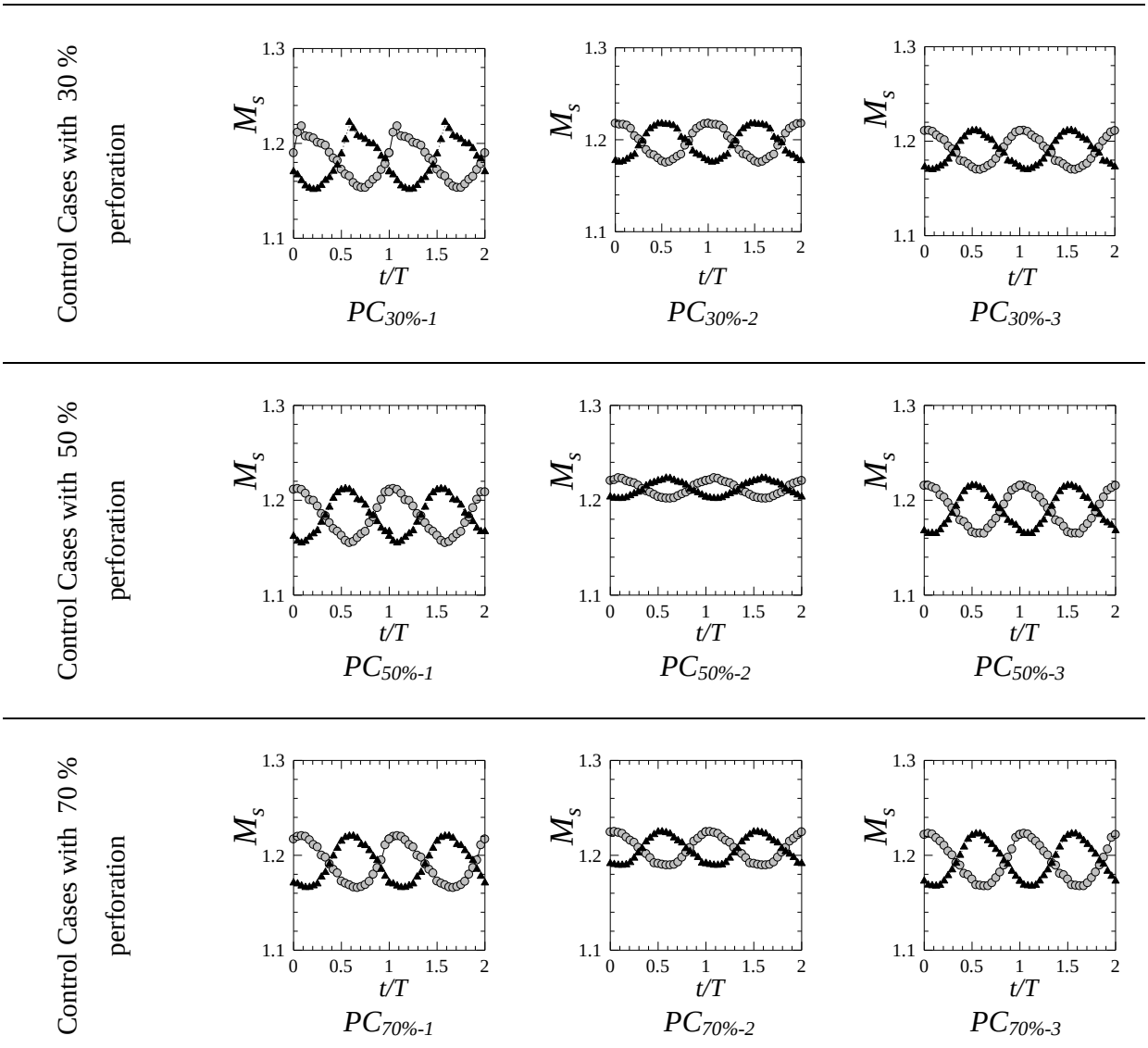

Fig 5.1.12: Variation of Shock Mach number with time. Line with circle and line with triangle represent shock Mach number on line $y/c = 0.1$ and $y/c = -0.1$ respectively

For base case maximum fluctuation of M_s is 0.115

Percentage of perforation of control cases	Configuration 1	Configuration 2	Configuration 3
30%	0.066	0.042	0.044
50%	0.060	0.025	0.051
70%	0.058	0.035	0.057

Table 5.1.3: fluctuations of shock mach number for different control cases with perforated cavity.

The phase difference in shock Mach at the beginning of oscillation cycle for open cavity installation supports the third mechanism most. So a possible and acceptable illustration of the mechanism for shock oscillation control with perforated cavity might be as follows:

The propagation of either pressure wave or upstream wave or may be both (further analysis is required) is obviously interrupted and shifted with a time delay/advance in such a manner that the upstream wave provide energy to the shock when the shock already has turned into a compression wave. So the pressure wave provide less energy to the shock during its strength gaining period so the shock strength is reduced. Rather it provides energy during its weakest period and increases the strength of the compression wave.

5.1.3 PRESSURE RISE ACROSS SHOCK WAVE ALONG SHOCK LENGTH

To analyze the effect of perforated cavity on the shock strength the time averaged $\Delta p/p_1$ is calculated at eleven different points along the shock [figure 4.3.5(a)] length and is shown in figure 5.1.13. From the figure the overall view of shock control can be understood.

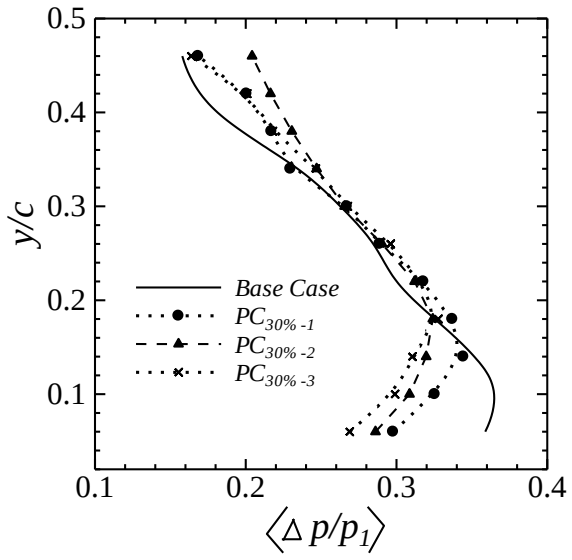

(a) 30% perforated cases

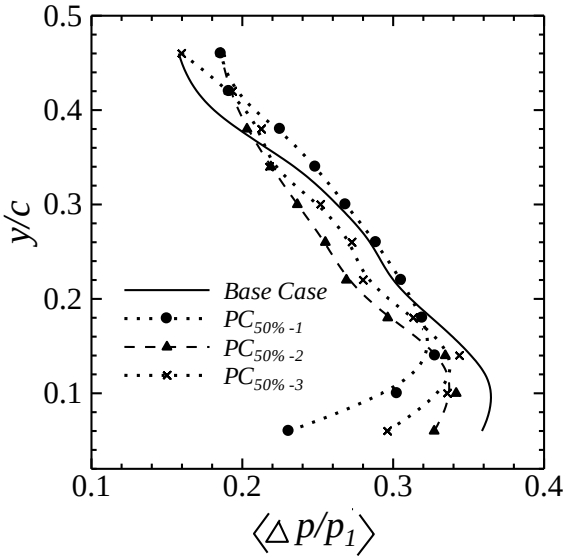

(b) 50% perforated cases

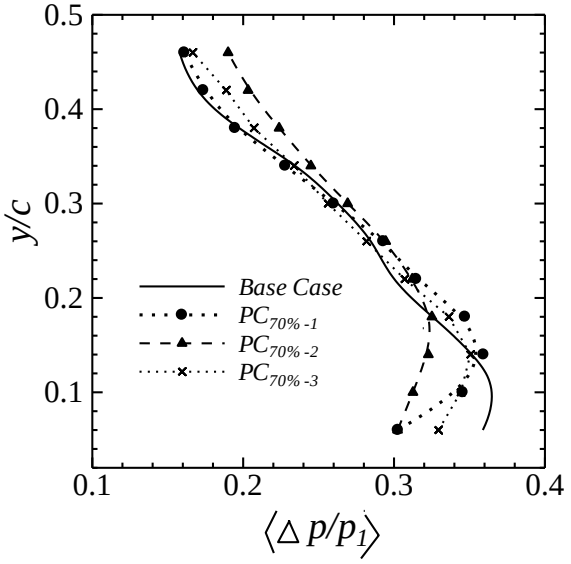

(c) 70% perforated cases

Fig 5.1.13: Time averaged pressure rise across shock wave along shock length

The perforated cavities with 30% perforation installed decrease the shock strength near the airfoil region but increases the shock strength slightly at far region. The values of maximum time averaged $\Delta p/p_1$ are found to be 0.272, 0.273 and 0.265 for cases $PC_{30\% - 1}$, $PC_{30\% - 2}$ and $PC_{30\% - 3}$ respectively. And the locations of maximum time averaged $\Delta p/p_1$ for cases $PC_{30\% - 1}$, $PC_{30\% - 2}$ and $PC_{30\% - 3}$ are found as y/c = 0.147, 0.170 and 0.185. These reductions in shock strength near the airfoil region lower the pressure fluctuation on the airfoil surface (will be discussed in section 5.3).

Again the perforated cavities with 50% perforation installed decrease the shock strength throughout the entire shock length except case $PC_{50\% - 1}$ where an increases of the shock strength at far region (about $y/c \geq 0.2$) is observed. The perforated cavities of 70% perforation show the same trend as of 30% perforated cavities. They also decrease the shock strength at near region while increase shock strength at far region.

Base case	
Value of maximum time averaged $\Delta p/p_1$	0.365
Location (y/c) of maximum time averaged $\Delta p/p_1$	0.1

Open cavity cases	OC_1	OC_2	OC_3
Value of maximum time averaged $\Delta p/p_1$	0.386	0.380	0.361
Location (y/c) of maximum time averaged $\Delta p/p_1$	0.260	0.213	0.222

30% perforated cases	$PC_{30\% - 1}$	$PC_{30\% - 2}$	$PC_{30\% - 3}$
Value of maximum time averaged $\Delta p/p_1$	0.343	0.346	0.324
Location (y/c) of maximum time averaged $\Delta p/p_1$	0.147	0.170	0.185

50% perforated cases	$PC_{50\% - 1}$	$PC_{50\% - 2}$	$PC_{50\% - 3}$
Value of maximum time averaged $\Delta p/p_1$	0.324	0.339	0.340
Location (y/c) of maximum time averaged $\Delta p/p_1$	0.146	0.107	0.134

70% perforated cases	$PC_{70\% - 1}$	$PC_{70\% - 2}$	$PC_{70\% - 3}$
Value of maximum time averaged $\Delta p/p_1$	0.356	0.329	0.349
Location (y/c) of maximum time averaged $\Delta p/p_1$	0.140	0.178	0.140

Table 5.1.4: Comparison of open and perforated cavities.

Meanwhile it has been already discussed that the increase in shock strength at far region can be a problem for real life applications especially where fluid flow through several airfoils situated side by side (compressor and turbines). Due to this problem the open cavities are not considered as suitable for use in an internal flow. As the cavity configuration is modified and perforated cavity has been introduced to overcome this problem, it is mandatory to compare the value of maximum time averaged $\Delta p/p_1$ and its location along the shock length (y/c). This comparison is provided in table 5.1.4.

From figure 5.1.13 and table 5.1.4 it is abundant that the perforated cavity can reduce the shock strength at the near region of the airfoil and the increases in shock strength at the far region is not significant like open cavity cases. So unlike open cavities perforated cavities can be for internal flow cases where flow occurs through a series of airfoils.

5.2 EFFECT OF PERCENTAGE OF PERFORATION

From figure 5.1.10 and table 5.1.1 it can be noticed that for a fixed configuration the shock excursion zone is changed with change in percentage perforation. For configuration 1 and 2 the shock excursion zone is minimum for 50% perforation and for configuration 3 the excursion zone increases with increase in percentage perforation. For a fixed percentage of perforation excursion zone is minimum for configuration 2.

Table 5.1.2 and table 5.1.3 show the fluctuation of pressure rise across shock wave and fluctuation of shock mach number. For different configuration different trend of reduction of these fluctuations are observed. For configuration 1 the fluctuation of pressure rise across shock increases with increase in percentage of perforation. The exact opposite trend is observed for configuration 3. For configuration 2 the pressure rise across shock first decreases and then increases with increase in perforation. For 50% perforation the shock oscillation turns into type A from B. This transformation of shock oscillation type could be the reason for this.

The change in shock oscillation type is found only for configuration 2. For different configuration different trend of reduction in shock Mach fluctuations are also observed. For configuration 1 the fluctuation of shock Mach decreases with increase in percentage of perforation and the exact opposite trend is observed for configuration 3. For configuration 2 the shock Mach fluctuation decrease and then increases with increase in perforation. As like shock strength this could be due to the change in shock oscillation type at 50% perforation of configuration 2.

5.3 CONTROL MECHANISM

5.3.1 BOUNDARY LAYER THICKNESS

Figure 5.3.1, 5.3.2 and 5.3.3 show the velocity profile at trailing edge of the airfoil for eight different time steps for 30%, 50% and 70% perforated cavity respectively. To compare all the cases time averaged velocity is calculated from these unsteady data at 24 different time steps and shown in figure 5.3.4.

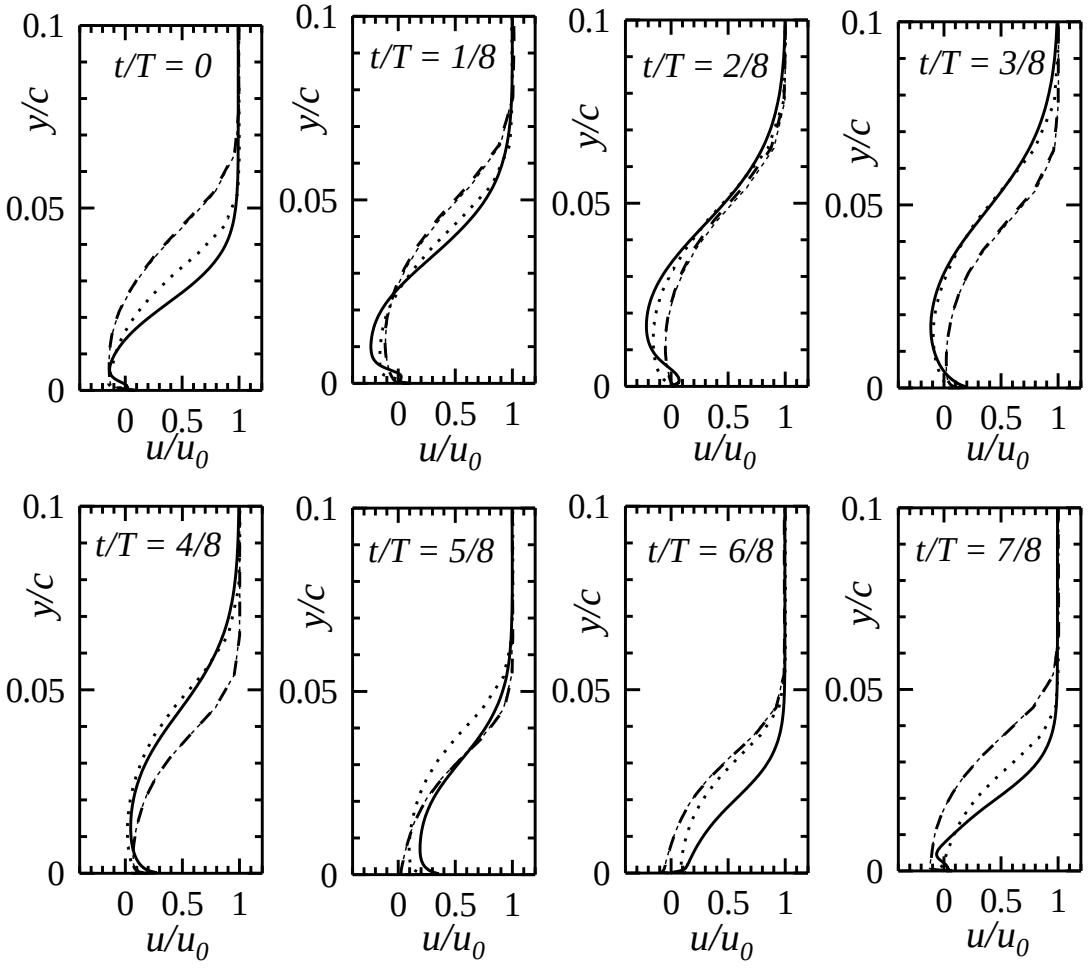

Fig 5.3.1: Velocity profile at trailing edge for 30 % perforated cavity cases. Solid line, dotted line, short dashed and dashed line represent base case, $PC_{30\%-1}$, $PC_{30\%-2}$ and $PC_{30\%-3}$

From the closer look of time averaged velocity profile it is abundant that the thickness of the boundary layer at the trailing edge is reduced significantly after using the perforated cavities. The time averaged boundary layer thickness is found are represented in table 5.3.1.

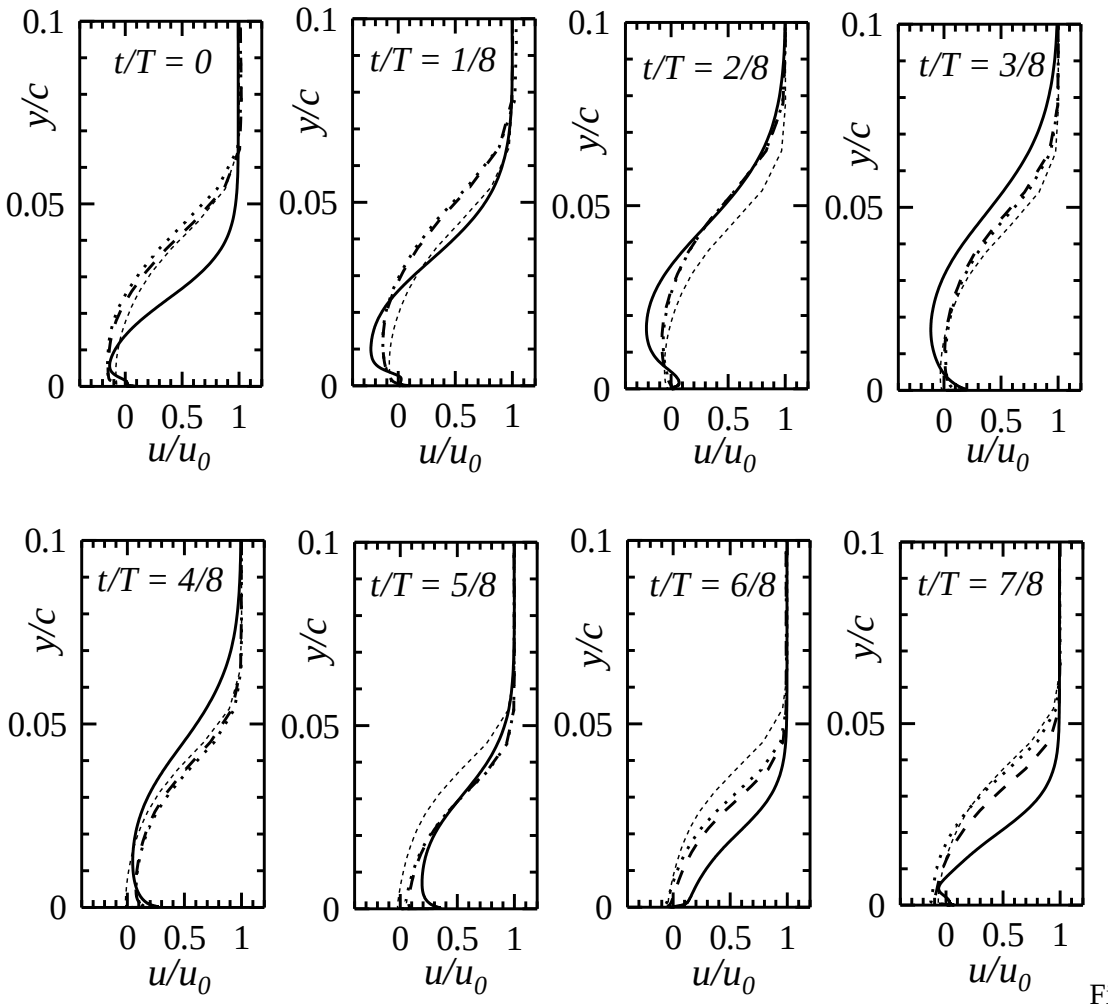

Fig:

Fig 5.3.2:Velocity profile at trailing edge for 50 % perforated cavity cases. Solid line, dotted line, short dashed and dashed line represent base case, $PC_{50\%-1}$, $PC_{50\%-2}$ and $PC_{50\%-3}$

From table 5.3.1 it is observed that the boundary layer thickness at the trailing edge is reduced significantly with incorporation of perforated cavities. For configuration 1 and 3 there is a reduction and then stall for boundary layer thickness with increasing percentage perforation. But for configuration 2 the boundary layer thickness first increases and then decreases with increasing percentage perforation. This could mean there is also a percentage of perforation for configuration 1 and 3 for which the boundary layer thickness will be minimum. This also indicates that the control with perforated cavity having configuration 2 is different from configuration 1 and 3. This is possibly for the smaller plates located at the two ends of the cavity for configuration 2, which allows shock to move more smoothly over the perforated cavity.

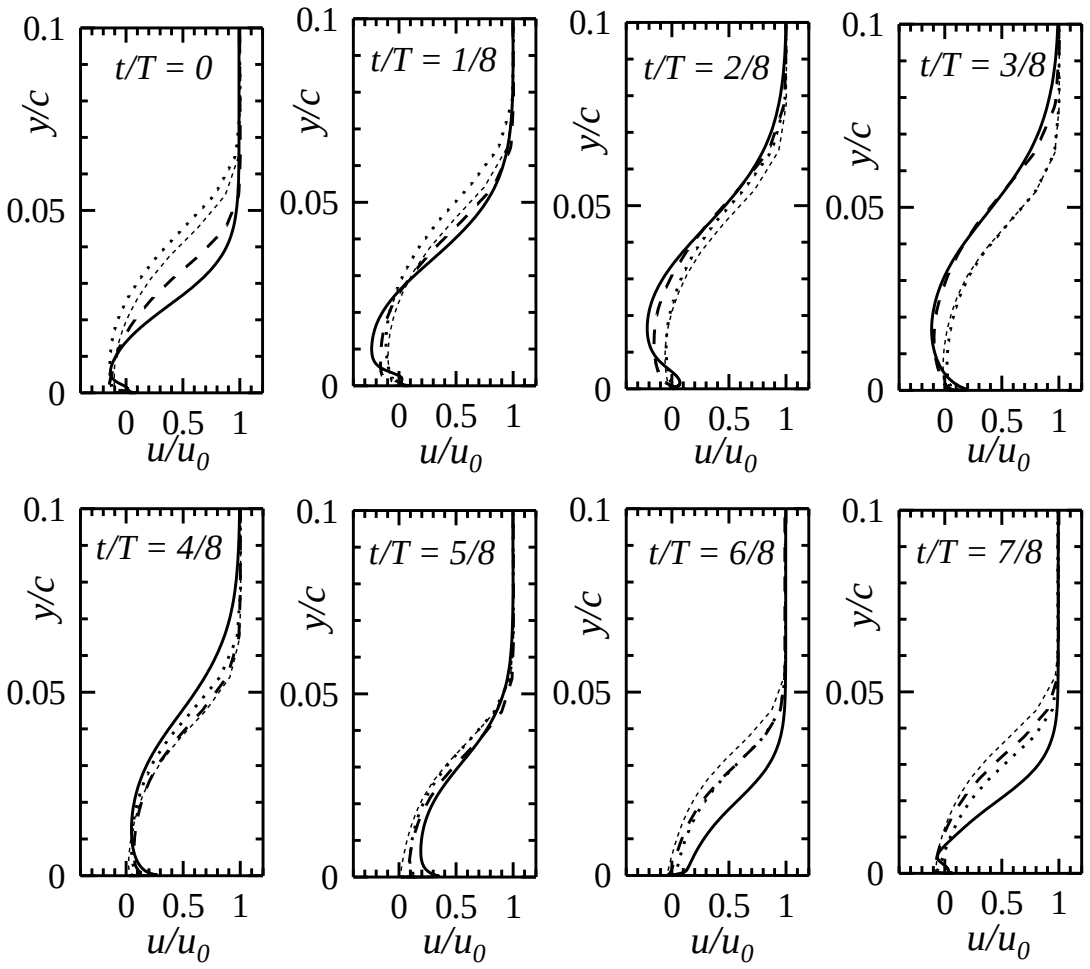

Fig 5.3.3: Velocity profile at trailing edge for 70 % perforated cavity cases. Solid line, dotted line, short dashed and dashed line represent base case, $PC_{70\%-1}$, $PC_{70\%-2}$ and $PC_{70\%-3}$

For base case time averaged Boundary layer thickness (δ)= 0.092

Percentage of perforation of control cases	Configuration 1		Configuration 2		Configuration 3	
	Time averaged δ	% decrease	*Time averaged* δ	% decrease	*Time averaged* δ	% decrease
30%	0.085	8%	0.077	16%	0.080	13%
50%	0.076	17%	0.073	21%	0.076	17%
70%	0.076	17%	0.074	17%	0.076	17%

Table 5.3.1: Time averaged boundary layer thickness for all perforated cavity cases.

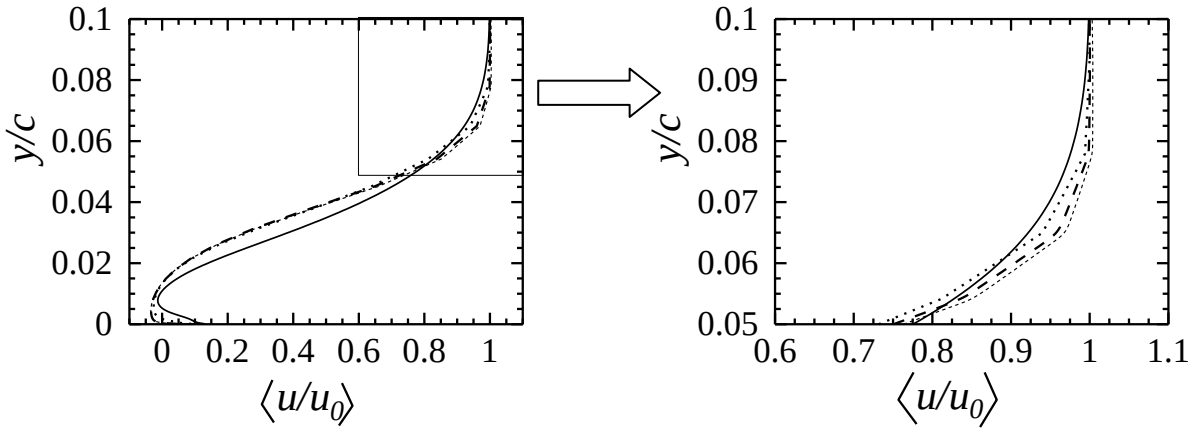

(a) Solid line, dotted line, short dashed and dashed line represent base case, $PC_{30\%-1}$, $PC_{30\%-2}$ and $PC_{30\%-3}$.

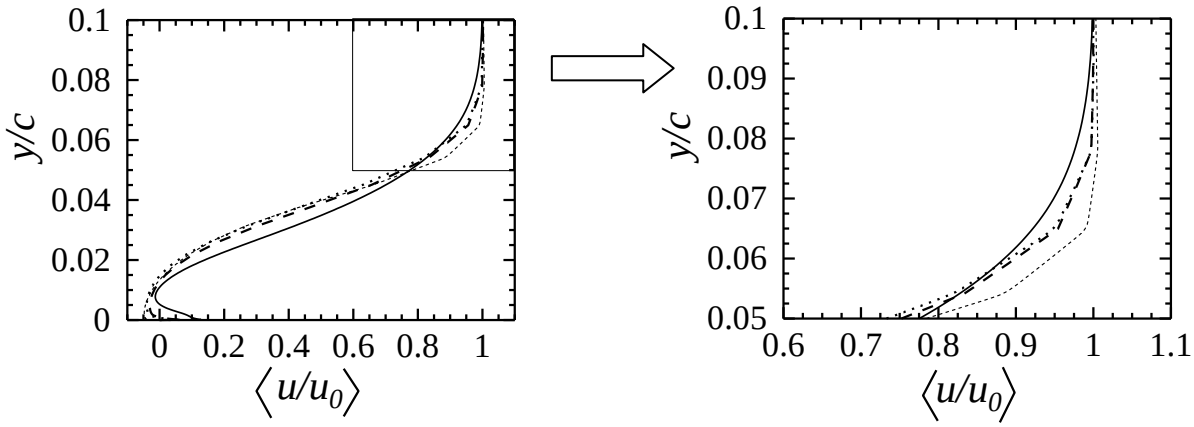

(b) Solid line, dotted line, short dashed and dashed line represent base case, $PC_{50\%-1}$, $PC_{50\%-2}$ and $PC_{50\%-3}$

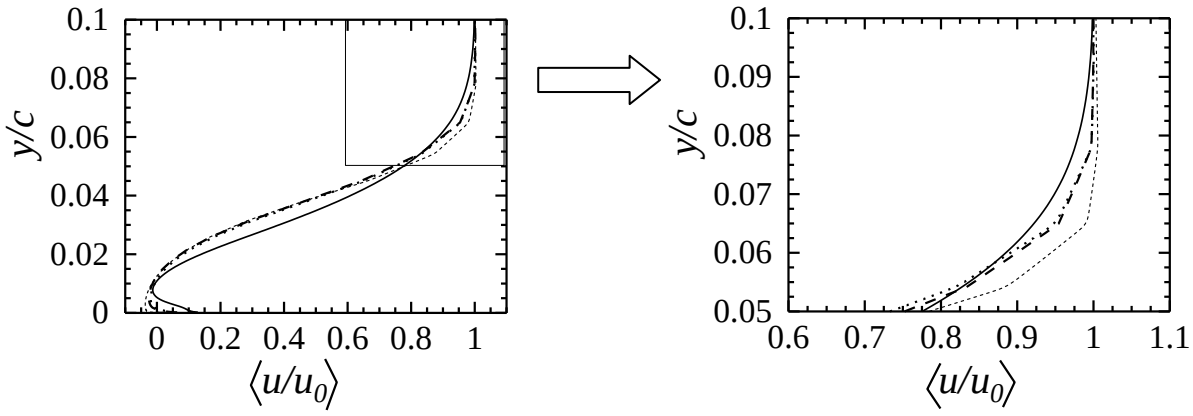

(c) Solid line, dotted line, short dashed and dashed line represent base case, $PC_{70\%-1}$, $PC_{70\%-2}$ and $PC_{70\%-3}$

Fig 5.3.4: Time Averaged velocity profile at trailing edge for (a) 30% (b) 50% and (c) 70% perforated cavity cases.

5.3.2 SHOCK BOUNDARY LAYER INTERACTION

Figure 5.3.5 shows the time variation of shock boundary layer interaction zone with time for all perforated cavity control cases. The interaction zone was calculated as the chord wise distance between points of maximum Mach number and the point where Mach number is unity as shown in figure 4.4.3(a). The time averaged value of $[x]_s/c$ is calculated from instantaneous data and are shown in table 5.3.2.

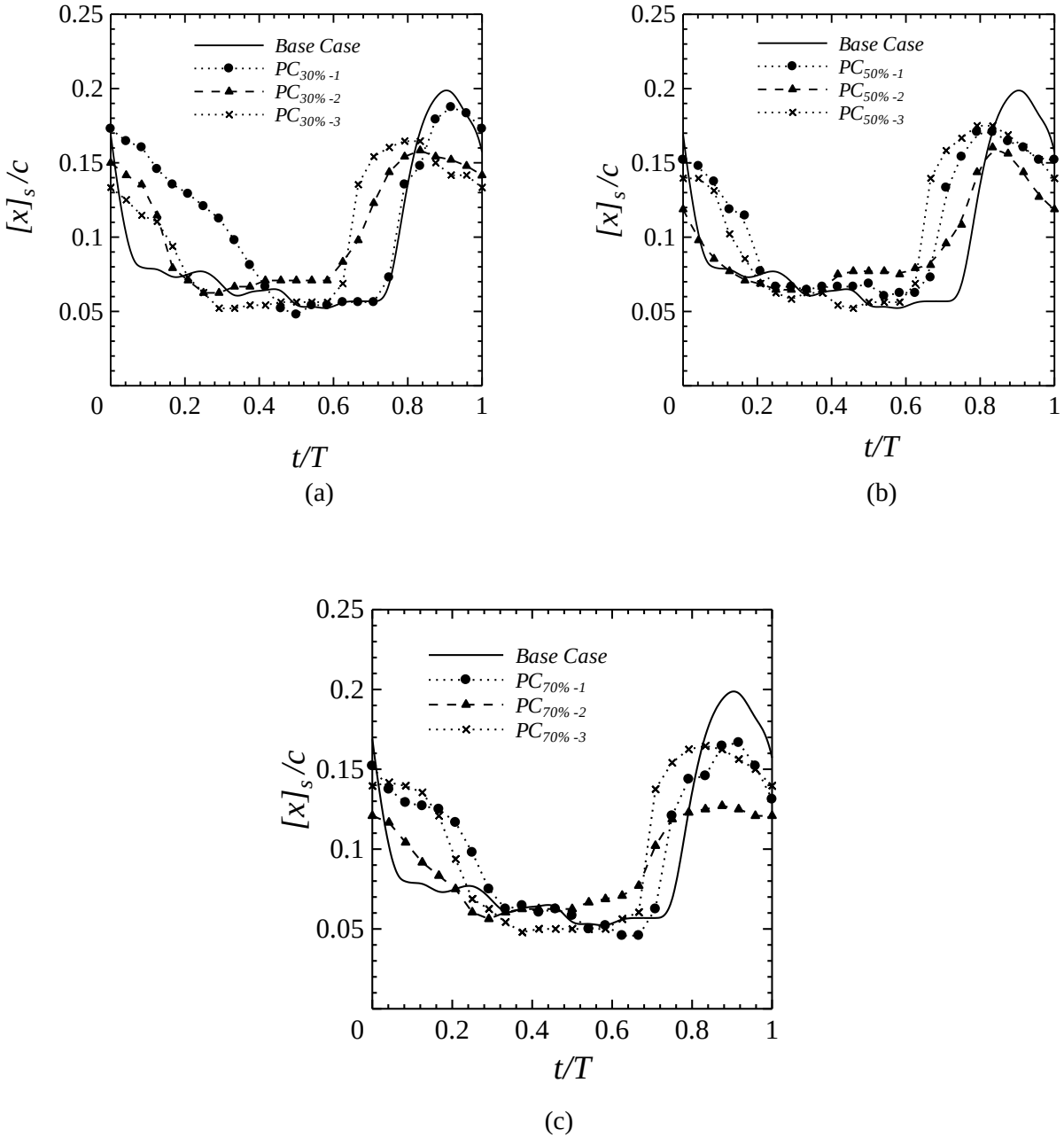

Fig 5.3.5: Shock-boundary layer interaction zone for (a) 30% (b) 50% (c) 70% perforated case.

For base case time averaged $[x]_s/c = 0.086$

Percentage of perforation of control cases	Configuration 1	Configuration 2	Configuration 3
	Time averaged $[x]_s/c$	*Time averaged* $[x]_s/c$	*Time averaged* $[x]_s/c$
30%	0.114	0.106	0.103
50%	0.109	0.095	0.108
70%	0.102	0.091	0.104

Table 5.3.2: Time averaged shock boundary layer interaction zone for all perforated cavity cases.

Table 5.3.2 reveals that the shock boundary layer interaction zone ($[x]_s/c$) for control cases is higher than the base case. This mean that the gradient of fluid properties is reduced at the shock foot for all control cases. This increase of $[x]_s/c$ for control cases enhances the communication between the upstream and downstream of the shock. This communication allows the reduction of pressure fluctuation on the airfoil surface.

5.4 PRESSURE FLUCTUATION ON AIRFOIL SURFACE

The unsteady pressure fluctuations over upper airfoil surface at different chord wise location for different control cases with perforated cavity are shown in figure 5.4.1, 5.4.2 and 5.4.3. From these figures the oscillation frequency of the shock oscillation is calculated as 760 Hz for all control cases. For all the cases frequency of shock oscillation is measured at point where pressure fluctuation is maximum.

The RMS of static pressure fluctuation is calculated from these unsteady pressure data. The RMS of static pressure fluctuation on upper airfoil surface is given in figure 5.4.4. The RMS of pressure fluctuation is calculated by the equation described in section 4.5. The values of RMS pressure fluctuation for all control case of perforated cavity are shown in table 5.4.1.

For base case maximum $p_{rms}/q_0 = 0.377$

Percentage of perforation of control cases	Configuration 1		Configuration 2		Configuration 3	
	Maximum p_{rms}/q_0	Percent reduction of p_{rms}/q_0	Maximum p_{rms}/q_0	Percent reduction of p_{rms}/q_0	Maximum p_{rms}/q_0	Percent reduction of p_{rms}/q_0
30%	0.275	27	0.188	50	0.187	50
50%	0.238	37	0.105	72	0.214	43
70%	0.225	40	0.159	58	0.225	40

Table 5.4.1: Maximum value of RMS of static pressure fluctuation on airfoil surface.

From figure 5.4.4 and table 5.4.1 it is clear that perforated cavity can reduce pressure fluctuation on the airfoil surfaces. The perforated cavity reduced the pressure fluctuation by about 25% to 70% while open cavity cases reduced the pressure fluctuation by about 70% to 80%.

So in terms of reducing surface static pressure fluctuation open cavities are better choice than perforated cavities. But for internal flows perforated cavity can be used with much closer adjacent airfoils where open cavities causes performance deterioration due to interaction of two stronger shock waves in between two airfoils.

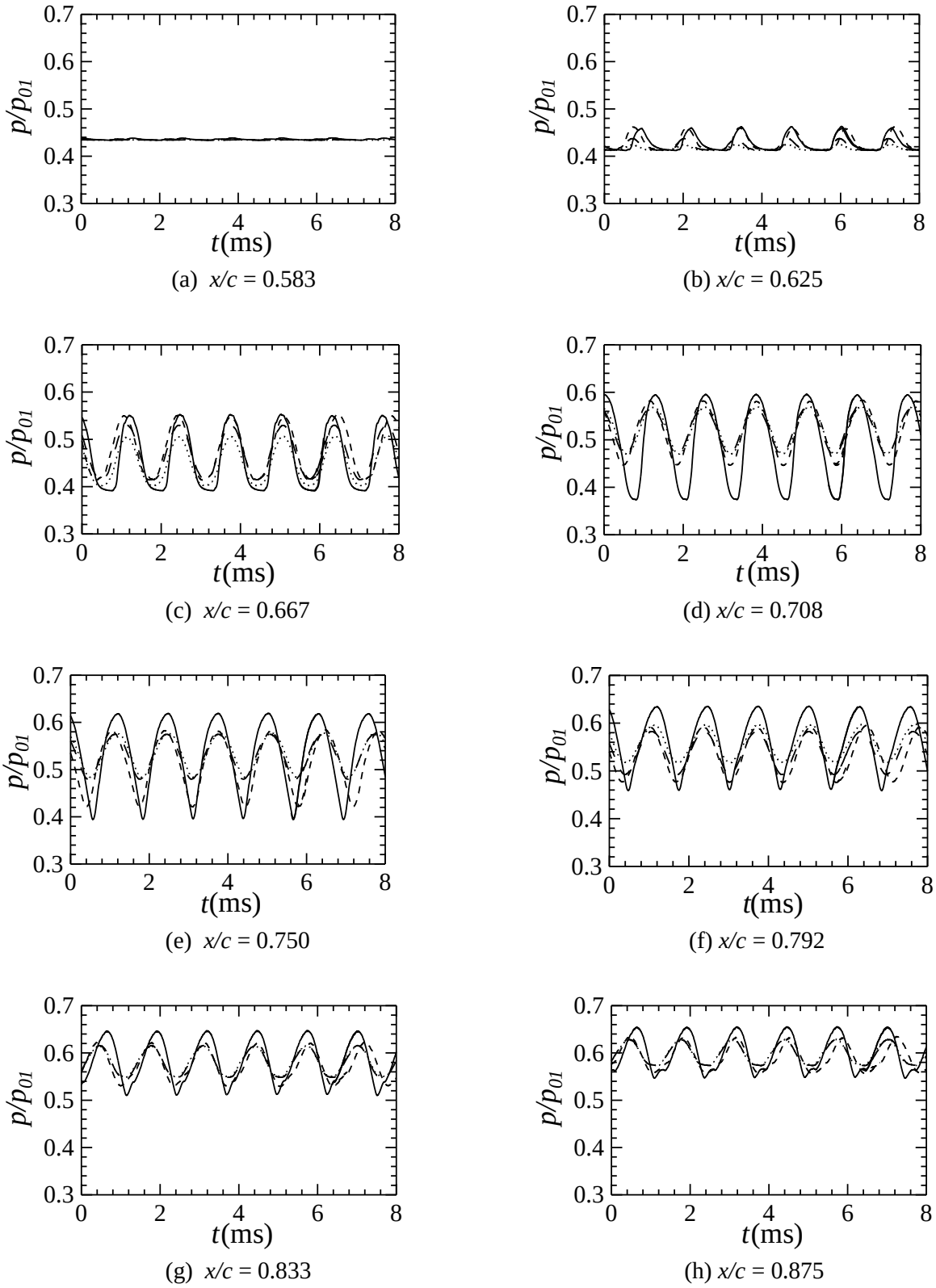

(a) x/c = 0.583 (b) x/c = 0.625

(c) x/c = 0.667 (d) x/c = 0.708

(e) x/c = 0.750 (f) x/c = 0.792

(g) x/c = 0.833 (h) x/c = 0.875

Fig 5.4.1: Pressure variation history with time at different location on upper airfoil surface for 30% perforated cavity. Solid, dashed, dotted and long dashed line represents Base Case, $PC_{30\%-1}$, $PC_{30\%-2}$ and $PC_{30\%-3}$.

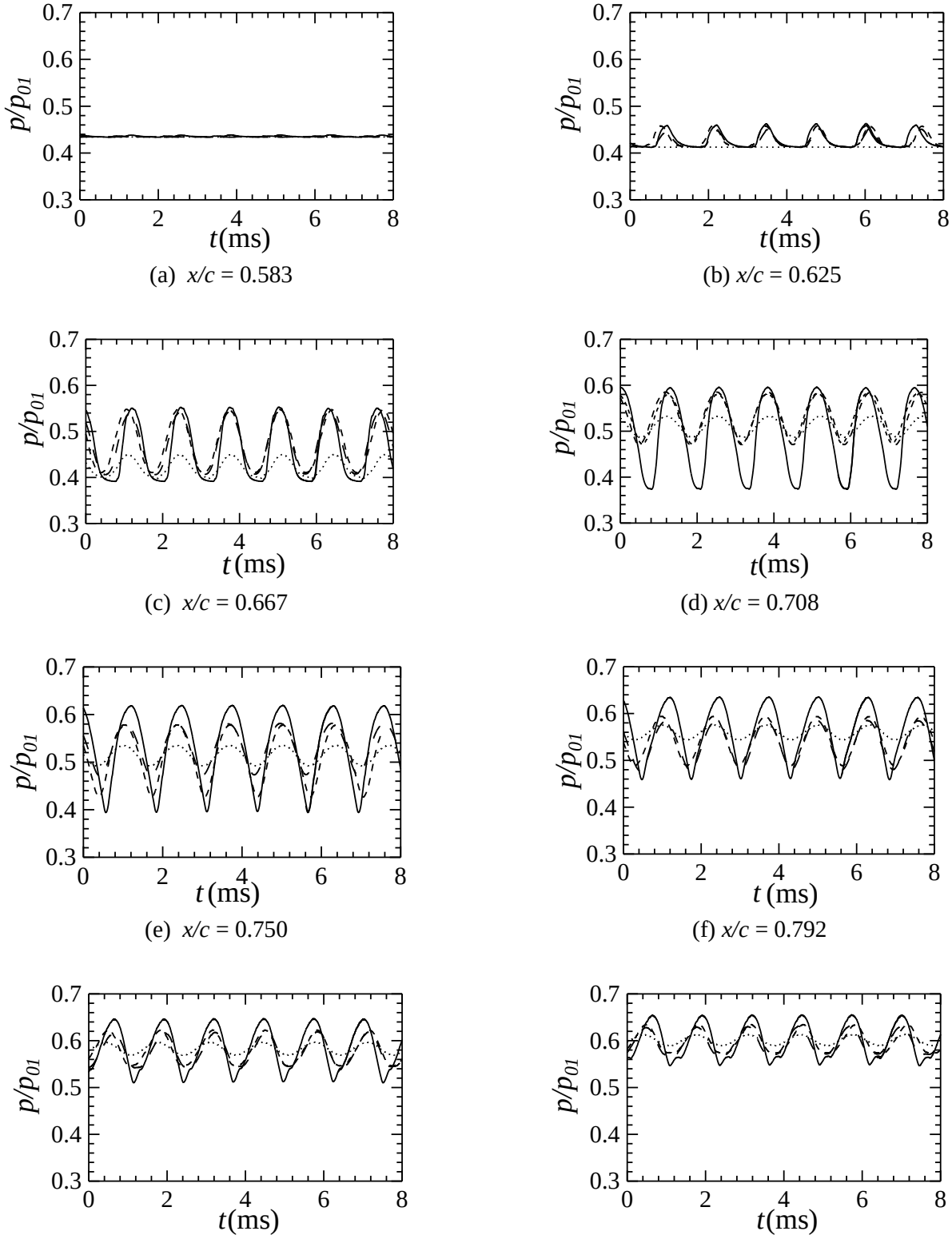

(a) x/c = 0.583 (b) x/c = 0.625

(c) x/c = 0.667 (d) x/c = 0.708

(e) x/c = 0.750 (f) x/c = 0.792

(g) x/c = 0.833 (h) x/c = 0.875

Fig 5.4.2: Pressure variation history with time at different location on upper airfoil surface for 30% perforated cavity. Solid, dashed, dotted and long dashed line represents Base case, $PC_{50\%-1}$ $PC_{50\%-2}$ and $PC_{50\%-3}$.

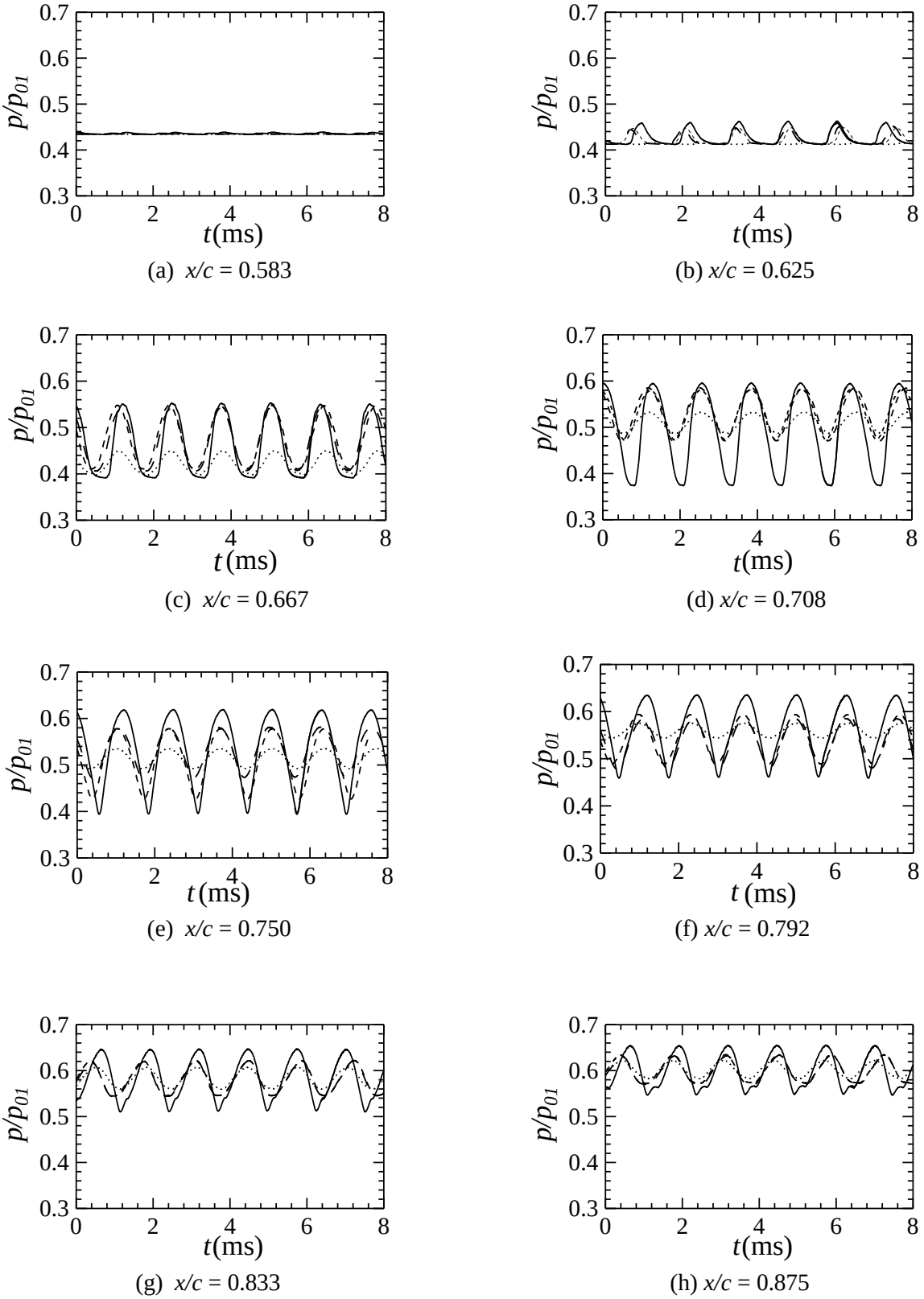

(a) x/c = 0.583 (b) x/c = 0.625

(c) x/c = 0.667 (d) x/c = 0.708

(e) x/c = 0.750 (f) x/c = 0.792

(g) x/c = 0.833 (h) x/c = 0.875

Fig 5.4.3: Pressure variation history with time at different location on upper airfoil surface for 30% perforated cavity. Solid, dashed, dotted and long dashed line represents Base case, $PC_{70\%-1}$, $PC_{70\%-2}$ and $PC_{70\%-3}$.

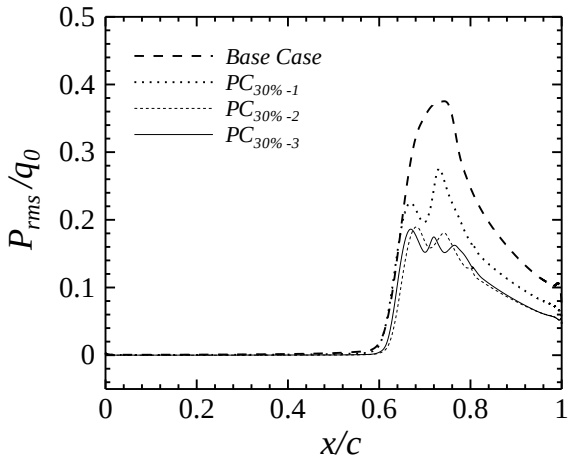

(a) 30% perforated cases

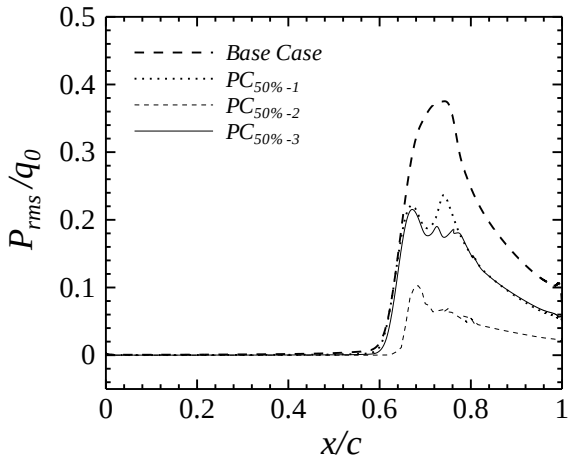

(b) 50% perforated cases

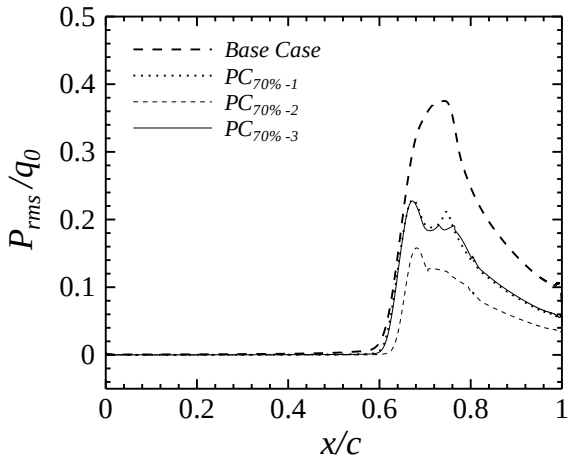

(c) 70% perforated cases

Fig 5.4.4: RMS pressure fluctuation over upper airfoil surface for control cases with perforated cavity.

5.5 TOTAL PRESSURE LOSS

As the perforated cavities can reduce the shock strength over the airfoil surface but increase the shock strength at the far region, the economic feasibility of perforated cavities is also a question. Like open cavity cases the total pressure loss is considered and studied at the airfoil trailing edge to assess the economic feasibility. The time averaged total pressure loss is calculated as a percentage of upstream total pressure (p_{01}).

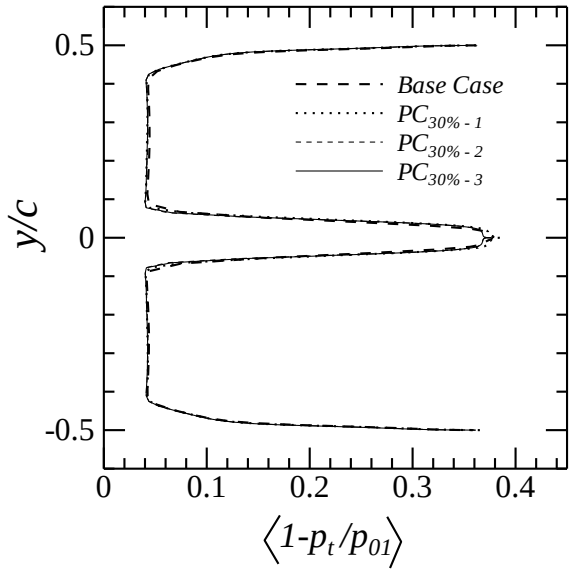

(a) 30% perforated cases

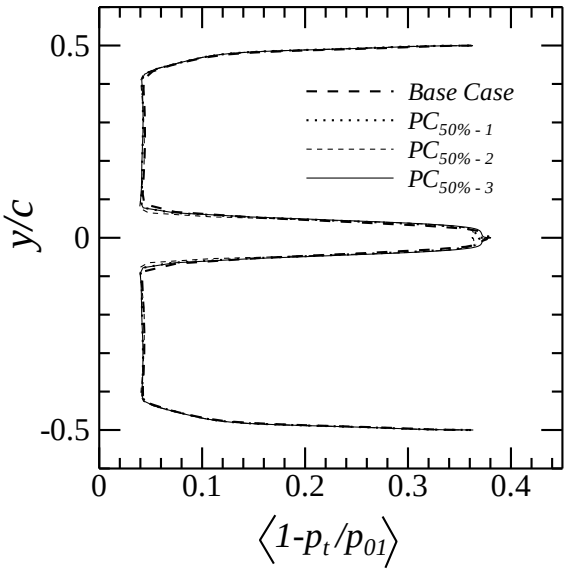

(b) 50% perforated cases

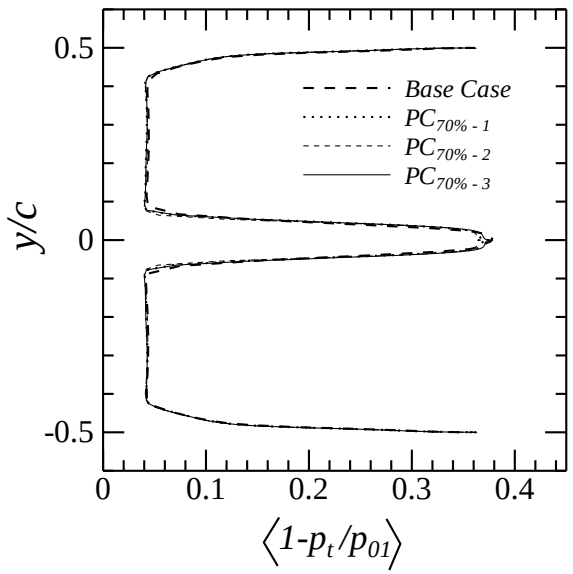

(c) 70% perforated cases

Fig 5.5.1: Time averaged total pressure loss for 50% perforated cases at trailing edge

Figure 5.5.1 shows the time averaged total pressure loss along the line parallel to *y*-axis passing through $x/c = 1$. The figure shows that the total pressure loss for the control cases with perforated cavity is reduced at the near regional flow field where $|y/c| \leq 0.05$. For open cavity cases thie region was much more wide $|y/c| \leq 0.1$. Like open cavity cases, for $|y/c| > 0.1$ the total pressure loss is almost same as the base airfoil

For further assessment of the open cavities the integrated total pressure loss (*ITPL*) is calculated as a percentage of upstream total pressure (p_{01}) at the trailing edge of the airfoil using the equation from section 4.6. The values of *ITPL* for different perforated cases are shown in table 5.5.1.

For base case ITPL = 8.60%

Percentage of perforation of control cases	Configuration 1	Configuration 2	Configuration 3
	ITPL (%)	*ITPL (%)*	*ITPL (%)*
30%	8.57	8.42	8.41
50%	8.43	8.32	8.50
70%	8.43	8.33	8.48

Table 5.5.1: Integrated total pressure loss (*ITPL*) for perforated cavities.

Table 5.5.1 confirms the economic feasibility of perforated cavities. The *ITPL* for open cavity cases are 8.27%, 8.28% and 8.27% for base case, OC_1, OC_2 and OC_3 respectively. So the open cavities are also more favorable from economic point of view. But due to its limitation perforated cavities could be the better choice for shock oscillation control in internal flows.

CHAPTER 6

SUMMARY AND RECOMMENDATION

6.1 SUMMERY OF THE STYDY

In the present study the effect of incorporating both open and perforated cavity on the airfoil surfaces are demonstrated systematically. Three different cases of open cavity control and nine different cases of perforated cavity control is studied along with the clean (base airfoil) airfoil. Results for base airfoil and airfoil with cavities (open and perforated) are compared to understand the effects of cavity installation. Shock strength, total pressure loss and surface pressure fluctuation are investigated by interpreting various shock characteristics like shock location, shock Mach number, boundary layer thickness and shock boundary layer interaction zone. After analyzing all the data and results the following can be concluded as the summery of this study:

i. Open cavity incorporation can affect the entire flow field. It can change both the shock structure and the type of shock oscillation. In present study (12% biconvex arc airfoil at zero incidence, pressure ratio 0.7, upstream Mach number 0.65) it changes the normal shock into a λ shock wave for a significant fraction of time (1/5 to 2/5 of the cycle period). The shock oscillation type is also changed to type A for all the open cavity configurations (for clean airfoil shock oscillation is type B).

ii. The length and depth of open cavity has impact on both the flow field and shock characteristics. Open cavity is significantly effective in order to reduce shock excursion zone, shock strength near airfoil surface and fluctuation of shock Mach number.

iii. Though open cavity reduces the shock strength near the airfoil region it increases the shock strength at far region. This limits the use of open cavity for internal flows where fluid flows through series of airfoils like compressors and turbines. Further realistic study is required for its application in internal flow cases.

iv. Open cavity reduces the boundary layer thickness at the trailing edge of the airfoil. This decrease of the boundary layer thickness may be due to the vortices created inside of the cavities.

v. Open cavity is significantly effective in minimizing the pressure fluctuation on the airfoil surfaces. 70% to 80% reduction of static pressure fluctuation is obtained for present study. So open cavities could be used as noise, fatigue and vibration reducing technique.

vi. Open cavity slightly reduce the integrated total pressure loss (*ITPL*), confirming its economic feasibility. So open cavity could be used economically and effectively in external flow cases over a single airfoil.

vii. For incorporation of perforated cavity the configuration and percentage of the perforation has impact on the development of the flow field, shock oscillation and shock structure.

viii. For configuration of perforation with openings at the two ends of the cavity (configuration 1 and 3) higher shock foot is achieved with higher percentage of perforation meanwhile for configuration of perforation without openings at the ends of the cavity (configuration 2) the shock foot shows different trend of dependency on percentage perforation.

ix. The configuration and percentage of perforation has a roll on the variation of changing mode (increasing/decreasing /first increasing then decreasing/ increasing then become constant etc) of the shock properties like excursion zone, shock strength, shock Mach number etc.

x. Like open cavities perforated cavities also reduces the pressure fluctuation and shock strength near the airfoil surface while increases the shock strength at the far region. But for perforated cavities increase in shock strength at far region is not much significant compared to the open cavity cases. And the location of maximum time averaged $\Delta p/p_1$ is far less than the open cavity cases. So open cavity could be used for internal high speed flows.

xi. For perforated cavity reduction in surface pressure fluctuation and total pressure loss is less compared to open cavities. So open cavities could be a better choice for external high speed flow but for internal flow application perforated cavities provide better option.

6.2 RECOMMENDATION

The following recommendations can be suggested for future study:

i. Further study can be carried out to identify the effect of cavity incorporation (open and perforated) on the shock oscillation frequency. The study could be based on the calculation of velocities of the downstream moving pressure wave and upstream propagating wave. The time required for the pressure wave to propagate from shock foot to the trailing edge and the time required for the upstream waves to move from the trailing edge to the shock wave can be compared with the time period of the shock oscillation. From the comparison it could be possible to find out if there is any other physical event associated with the shock oscillation mechanism for control cases.

ii. This study is performed based on Lee's feedback mechanism. The same study could be analyzed based on the effective airfoil shape and corresponding change in airfoil camber. The study could involve calculations of displacement thickness, momentum thickness and shape factor.

iii. This study identifies a major limitation of open cavities for high speed internal flow applications like compressors and turbines and suggests use of perforated cavity for such flows. Further study can be carried out to find out the optimum distance between two airfoils to achieve gentler but efficient machinery operation from the combined study of fluid machinery performance analysis and shock oscillation phenomenon. The study could involve study of the interaction of two shock waves and their other properties like pressure fluctuation and total pressure loss due to the superposition of two stronger shockwave.

REFERENCES

[1] McDevitt, J.B., Levy, L. L., and Deiwert, G. S., "Transonic Flow about a Thick Circular-arc Airfoil", *AIAA Journal*, 14(5), 603-613, 1976.

[2] Tijdeman, H., " Investigations of the Transonic Flow Around Oscillating Airfoils", *National Aerospace Laboratory*, 1977.

[3] Levy, L. L., "Experimental and Computational Steady and Unsteady Transonic Flows about a Thick Airfoil", *AIAA Journal*, 16(6), 564-572, 1978

[4] Tijdeman, H., Seebass, R., "Transonic Flow Past Oscillating Airfoils", *Annual Review of Fluid mechanics Journal*, 12(1), 181-222, 1980.

[5] Gronland, T.A., Eliasson. P., Nordstrom, J., "Accuracy of Unsteady Transonic Flow Computations", *International Council of the Aeronautical Sciences*, 21st congress, ICAS-98-.4.2, 1998.

[6] McDevitt, J.B., "Supercritical Flow about a Thick Circular-arc Airfoil", *National Aeronautics and Space Administration Technical Memorandum*, 6-88, January, 1979.

[7] Li, Y.C., Wang, J.J., Hua, J., "Experimental Investigations on the Effects of the Divergent Trailing Edge and Gurney Flaps on a Supercritical Airfoil", *Aerospace Science and Technology* 11, 91-99, 2007.

[8] Alfano, D., Michel, B., Corre, C., Lerat, A., "Numerical Simulation of Shock / Boundary - layer Self-sustained Oscillations for External and Internal Flows", *AIAA Paper, 24th Applied Aerodynamics Conference*, 2006-2840, 2006.

[9] Raghunathan, S., Early, J.M., Tulita, C., Bernard, E., Quest, J., "Periodic Transonic Flow and Control", *The Aeronautical Journal*, January, 2008.

[10] Chen, Li-Wei., Xu, Chang-Yue., Lu, Xi-Yun., "Numerical Investigation of the Compressible Flow Past an Airfoil", *J. Fluid Mech.*, 643, 97-126, 2010.

[11] Catalano, P., Tognaccini, R., "RANS Analysis of the Low-Reynolds Number Flow around the SD7003 Airfoil", *Aerospace Science and Technology*, 15(8), 615-626, December, 2011.

[12] Hasan, A.B.M. Toufique., Matsau, S., Setoguchi, T., and Islam, A.K.M. Sadrul, "Effects of Condensing Moist Air on Shock Induced Oscillation around an Airfoil in Transonic Internal Flows", *International Journal of Mechanical Sciences*, 1-11, 2011.

[13] Xiong, J., Nezhad, S. T., Liu, F., "Computation of Self-excited Unsteady Transonic Flow of an airfoil in a channel using URANS and DES" *AIAA Paper*, 2010-5109, 2010.

[14] Bendiksen, O. O.,"Review of Unsteady Transonic Aerodynamics: Theory and Application", *Progress in Aerospace Sciences*, 47, 135-167, 2011.

[15] Yagiz B., Kandil O., Pehlivanoglu Y. V.," Drag minimization using active and passive flow control techniques", *Aerospace Science and Technology*, 17 (1), 21-31, 2012.

[16] Eleni, D. C., Athanasios, T. I., Dionissios, M. P., “Evaluation of the Turbulence Models for the Simulation of the Flow over a National Advisory Committee for Aeronautics (NACA) 0012 Airfoil”, *Journal of Mechanical Engineering Research*, 4(3), 100-111, March, 2012.

[17] Lee, B. H. K., “Self-sustained shock oscillations on airfoils at transonic speeds”, *Progress in Aerospace Sciences*, 37 (1), 147-196, 2001.

[18] Alshabu, A., Olivier, H.,“Unsteady wave phenomena on a supercritical airfoil”, *AIAA Journal*, 46, 2066-2073, 2008.

[19] Zhao, Z., Ren, X., Gao, C., Xiong, J., Liu, F., Luo, S., "Experimental Study of Shock Wave Oscillation on SC(2)-0714 Airfoil", *in 51st AIAA Aerospace Sciences Meeting*, Texas, AIAA 2013-0537, 2013.

[20] Sartor, F., Mettor, C., Sipp, D.,“Stability, Receptivity, and Sensitivity Analyses of Buffeting Transonic Flow over a Profile”, *AIAA Journal*, 53, 1980-1993, 2015.

[21] Qin N., Zhu Y.,Shaw S.T.,"Numerical study of active shock control for transonic aerodynamics", *International Journal of Numerical Methods for Heat and Fluid Flow* , 14(4), 444-466, 2004.

[22] Stanewsky, E., "Adaptive Wing and Flow control Technology", *Progress in Aerospace Sciences*, 37(7), 583-667, 2001.

[23] Li, J., Lee, C. H., Jia, L., Li, X., "Numerical Study on Flow Control by Micro-Blowing", *47th AIAA Aerospace Sciences Meeting*, Orlando, Florida, AIAA 2009-779, 2009.

[24] Hasan, A. B. M. T., Matsuo, S. , Setoguchi, T. , Kim, H.-D.Yu, S., "Control of transonic flow with non-equilibrium condensation around a circular arc blade using bump", *International Journal of Turbo and Jet Engines*, 26(1), 3-49, 2009.

[25] Raghunathan S., Early J. M.,Tulita C., Benard E. Quest J., "Periodic transonic flow and control" , *Aeronautical Journal*, 112, 1-16, 2008.

[26] Ashill P.R., Fulker J.L. , Shires A.,"A novel technique for controlling shock strength of laminar-flow aerofoil sections", *First European Forum on Laminar Flow Technology*, Hamburg, Germany, 1992.

[27] Patzold M., Lutz Th. ,Kramer E. ,Wagner S."Numerical optimization of finite shock control bumps", *44th Aerospace Science Meeting and Exhibit*, Reno, Nevada, AIAA Paper-1054, 2006.

[28] Tian Y., Liu P. , Feng P., "Shock control bump parametric research on supercritical airfoil", *Science China Technological Sciences*, 54(11), 2935-2944, 2011.

[29] Mazaheri K., Kiani K.C., Nejati A., Zeinalpour M., Taheri R., "Optimization and analysis of shock wave/boundary layer interaction for drag reduction by Shock Control Bump", *Aerospace Science and Technology*, 42, 196-208, 2015.

[30] Hasan A.B.M.T, Alam M., "A numerical study on the control of self-excited shock induced oscillation in transonic flow around a supercritical airfoil", *International Journal of Fluid Mechanics Research*, 41(5), 440-459, 2014.

[31] McComick D.C., "Shock/Boundary-Layer Interaction control with Vortex Generators and Passive Cavity", *AIAA Journal*, 31(1), 91-96, 1993.

[32] Smith A.N., Babinsky H., Dhanasekaran P.C., Savill Mark, Dawes Bill, "Computational Investigation of Groove Controlled Shock Wave / Boundary Layer Interaction", *41st Aerospace Sciences Meeting and Exhibit*, Reno, Nevada, 0446, 2003.

[33] Rowley D. C., Williams, "Dynamics and control of high-Reynolds-number flow over open Cavities", *Annual Review of Fluid Mechanics*, 38, 251-276, 2006.

[34] Olsman W. F. J., Colonius T.,"Numerical simulation of flow over an airfoil with a cavity", *AIAA Journal*, vol. 49(1), 143-149, 2011.

[35] Rahman M.M., Hasan A.B.M.T, Islam A.K.M.S., Matsuo S., Setoguchi T., "Computation of transonic internal flow around a biconvex airfoil with cavity", *Journal of Mechanical Science and Technology*, 29(6), 2415-2421, 2015.

[36] Yu, T., Wang, J.J., Zhang, P.F., "Numerical Simulation of Garney Flap on RAE-2822 Supercritical Airfoil", *Journal of Aircraft*, 48(5), 1565-1575, 2011.

[37] Hartmann, A., Klass, M., Schroder, W., "On the interaction of shock waves and sound waves in transonic buffet flow", *Physics of Fluids*, 25, 026101, 2013.

[38] Bahi, L., Ross, J. M., and Nagamatsu, H. T.," Passive shock wave/boundary layer control for transonic airfoil drag reduction", *AIAA Paper, 83-0137,* 1983.

[39] Nagamatsu, H. T., Orozco, R. D., and Ling, D. C., "Porosity effect on supercritical airfoil drag reduction by shock wave/boundary layer contro"l, *AIAA Paper, 84-1682,* 1984.

[40] Raghunathan, S., "Passive control of shock-boundary layer interaction", *Progress in Aerospace Sciences*, 25, 271–296, 1989.

[41] Doerffer, P., and Szulc, O.," Passive control of shock wave applied to helicopter rotor high-speed impulsive noise reduction". *Polish Academy of Sciences, Fiszera* 14, 80-952, 2010.

[42] Yamamoto K., Tanida Y., "Self excited oscillation of transonic flow around an airfoil in two-dimensional channels", *ASME Journal of Turbomachinery*, 112, 723-731, 1990.

[43] Xiong, J., Nezhad, S. T., Liu, F., "Computation of Self-excited Unsteady Transonic Flow of an airfoil in a channel using URANS and DES" *AIAA Paper,* 2010-5109, 2010.

[44] Hamid, M. A., Hasan, A. B. M. T., Alimuzzaman, S. M., Matsuo, S., Setoguchi, T., "Compressible flow characteristics around a biconvex arc airfoil in a channel", *Propulsion and Power Research,* 3(1), 29-40, 2014.